Studies on the Manipulation of Intrinsic Localized Modes in Coupled Cantilever Arrays

Masayuki Kimura

December 2008

Abstract

In late 1980s, intrinsic localized mode (ILM) was theoretically discovered in a nonlinear coupled oscillator. This discovery triggered wide-spread investigations on energy localization phenomena in spatially discrete systems. Recently, the ILM was experimentally observed in micro-mechanical cantilever arrays fabricated by micro-electromechanical system (MEMS) technology. This observation directly suggests that if the spatial controllability is confirmed, ILM has potential applications in MEMS devices. However, the dynamical behavior of ILM is still an open problem. The dynamics of traveling ILM should be clarified to establish control schemes. Therefore, this thesis aims to study the possibility of control of ILM in coupled cantilever arrays.

In this thesis, at first, a nondimensionalized equation of motion is described by modeling micro-cantilever arrays in which ILMs were observed. The resulting equation consists of on-site and inter-site potentials. Each potential is represented by quadratic and quartic terms. For the equation, the coexistence and the stability of ILM are numerically discussed. Observed ILMs are classified into Sievers-Takeno (ST) mode and Page (P) mode. According to the stability analysis, ST-modes are stable when P-modes are unstable, and *vice versa*. The stability of coexisting ILMs is flipped by varying the nonlinear inter-site coefficient.

The global phase structure is investigated by calculating invariant manifolds of unstable ILMs. The drastic change of the global phase structure is caused when the stability of coexisting ILMs is flipped. Furthermore, the influence of impurities is also discussed. An impurity locally changes the global phase structure.

The dynamical feature of traveling ILM is discussed with the structure of invariant manifolds of unstable ILMs. Through the discussion, it is shown that the relationship between the structure of invariant manifold and behavior of ILMs is clearly understood. It is suggested that the motion of traveling ILM in the coupled cantilever array is governed by the extension of unstable manifolds and its recurrence.

A new manipulation concept is proposed based on the fact that the global phase

structure governs traveling ILMs and is changed by varying the nonlinear inter-site coefficient. The new manipulation is called "capture and release." An ILM can be shifted to any site in the cantilever array. In addition to that, a traveling ILM wandering in the whole of array can also be produced. Furthermore, manipulations using impurity is discussed. The mechanism of the attractive/repulsive manipulation is revealed.

To confirm the numerically obtained results, a macro-mechanical cantilever array is proposed. The cantilever array is designed to have individually tunable on-site potentials. The attractive manipulation of ILM in the cantilever array is experimentally demonstrated and numerically confirmed. The numerical investigation suggests that the global phase structure plays an important role for the manipulation.

Contents

Chapter 1

Introduction

1.1 Localized Solutions in Nonlinear Coupled Systems

Energy localization phenomenon is known as soliton for continuum media and intrinsic localized mode (ILM) for discrete media. ILM, also called discrete breather (DB), appears as a spatially localized and temporally periodic solution in coupled differential equations with nonlinearity. In 1988, A. J. Sievers and S. Takeno analytically discovered an odd-symmetric ILM in a Fermi-Pasta-Ulam (FPU) lattice [1,2], which has both harmonic and anharmonic inter-site potentials[1]. An even-symmetric ILM was derived by J. B. Page in 1990 [4]. After this discovery, ILM in nonlinear discrete systems has attracted many researchers. In the first decade since the discoveries, the existence [5–11], the stability [12–15], the movability [16–20], and the other properties of ILM have been investigated both theoretically and numerically for variety of physical systems [21]. These analyses clarify the fundamental properties of ILM in both FPU lattices and nonlinear Klein-Gordon (KG) lattices. Whereas the FPU lattices contain linear and nonlinear inter-site potentials, the nonlinear KG lattices consist of linear inter-site potential and nonlinear on-site potential including the harmonic term. It seems that the analyses of ILM for both lattices provide the impetus for further investigations on localized phenomena in realistic systems.

In this decade, experimental studies have appeared [22]. ILM is experimentally generated or observed in various systems, for instance, Josephson-junction arrays [23–25], optic wave guides [26,27], photonic crystals [28], micro-mechanical cantilever array [29], mixed-valence transition metal complexes [30, 31], antiferromag-

---

[1]The FPU lattice has been proposed as a discrete model of material by Fermi, Pasta, and Ulam for investigating the equipartition of energy among the degrees of freedom [3].
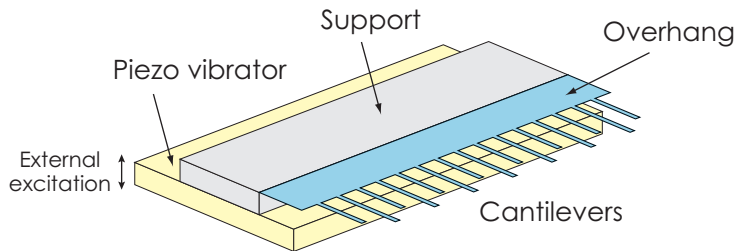
Figure 1.1: Schematic configuration of a micro-cantilever array fabricated by M. Sato *et al.* [29]. Short and long cantilevers are coupled by the overhang region which is a flexible thin film. To excite the cantilevers, the piezo vibrator is attached to the support.

nets [32], and electronic circuits [33]. These experiments suggest the phenomenological universality of ILM and the possible application phase. Studies have indeed appeared toward potential applications in both fundamental science and practical engineering [22].

1.2 Experimental Studies in Micro-cantilever Arrays

Sato *et al.* have shown the existence of intrinsic localized modes in micro-cantilever arrays [29,34]. They fabricated a di-element cantilever array by microelectromechanical system (MEMS) technology. Short and long cantilevers are alternately arranged in one dimension and they are coupled by the overhang region as shown in Fig. 1.1. To reduce energy dissipations, the cantilever array was in high vacuum, so that the quality factor of resonating cantilever was about 10^4. A piezo vibrator, which is attached to the substrate, excites the array to keep oscillations of cantilevers.At first, the frequency of the piezo vibrator was set at the upper zone boundary of the band formed by the coupled cantilevers. Then the zone boundary mode was excited. To generate ILMs, the modulational instability of the zone boundary mode is caused by frequency chirping. The initially excited mode lost its stability when the frequency of vibrator was increased. After the chirping was stopped, several localized oscillations remained. That is, ILMs were produced. When the external vibration was turned off, the ILMs began to decay, and finally disappeared. On the other hand, localized oscillations wandering in the array were also observed during frequency chirping. These localized oscillations are called *traveling* ILM. It was shown by the above experiment that standing ILMs exist even at a micrometer scale in mechanical structure. It was also suggested by the observation of traveling ILMs that we can

manipulate standing ILMs without destroying them.

Manipulation of ILM in micro-cantilever arrays has also been realized by M. Sato [35,36]. They used a localized impurity to manipulate ILMs. The impurity was induced by IR laser that could locally heat the array. Several cantilevers in the heated region have different resonant frequency to the others. Thus, the heated region can be thought of as a localized impurity. A standing ILM was attractively or repulsively manipulated by the impurity. The ILM maintained its energy concentration during the manipulation. Therefore, ILM was possibly shifted from a site to another without loss of its energy concentration. These experimental results allow us to expect applications of ILM in practical engineering, especially micro- and nano-engineering.

In terms of micro- and nano-engineering, a cantilever structure is widely used for both sensing and actuating [37]. A resonating cantilever has capabilities to measure various physical and chemical quantities with high accuracy. Mass sensing is an example of sensor applications. The resonant frequencies of cantilever are determined by the stiffness, the size, and the mass of cantilever. Therefore, the resonant frequency is changed when the mass is varied. By using the frequency shift, attogram (10^{-18} g) level detections are realized [38]. On the other hand, a more sensitive mass sensor has been proposed by M. Spletzer *et al.* [39]. They utilized a coupled cantilever, which consists of two identical cantilevers. The coupled cantilever array is modeled as a linear coupled system in which two linear oscillators are coupled by a linear spring. The linear coupled system has two eigenmodes, namely, symmetric and antisymmetric mode. M. Spletzer *et al.* showed that the mode symmetries were sensitively broken when a tiny particle was attached on a cantilever. The resonant frequencies of the eigenmodes were also changed but the amount of the frequency shift was small. It was suggested that the sensitivity of mass sensors using eigenmodes is three or four orders of magnitude greater than by using the resonant frequency [39]. That is, coupled cantilevers can be utilized to ultra sensitive mass sensors. ILM is a solution of a nonlinear coupled oscillator as well as a linear eigenmode of a linear coupled oscillator. Thus, ILM is a considerable phenomenon for detecting the change of mass through dynamical transition. On the other hand, an ILM can perform as a local exciter of micro-cantilever arrays. A desired cantilever can be excited when an ILM is manipulated. If the spatial controllability is confirmed, ILM has potential applications in MEMS devices. Therefore, dynamical analyses on ILM in micro-cantilever arrays are necessary to realize such applications.

1.3   Global Dynamics of Propagating Waves

Standing ILMs are solutions that do not propagate in nonlinear coupled systems. It allows us to expect that there is an analogy between the standing ILMs and stationary waves. In a nonlinear coupled system, the global dynamics of traveling waves related to stationary waves has been investigated in terms of the nonlinear dynamical system theory [40–42]. A magneto-elastic beam system has been proposed as an experimental model of nonlinear coupled system. Cantilevered elastic beams are placed with an equal interval in one dimension. In the model, two permanent magnets are placed to face the free end of each beam so that nonlinearity is induced in the restoring force. The coupling force between adjacent beams is caused by a long elastic beam. Nonlinearity in the coupling force is also considered in the model. It should be noted that the experimental model is described by a similar equation of motion to that of the micro-cantilever array in which ILMs are observed. In the model, an external vibrator is attached at a boundary of array while another boundary is kept free. For a specific amplitude and a single frequency, many stationary waves were observed both experimentally and numerically. That is, the stationary waves coexist in the magneto-elastic beam system. The dynamics of traveling wave was investigated by calculating basin structures around the coexisting stationary waves. Resulting basin structures imply that there are heteroclinic connections between the stable and the unstable invariant manifolds of unstable stationary waves around the unstable waves [41]. Consequently, it was suggested that the transition of traveling wave is governed by the phase structure in the vicinity of coexisting stationary waves. Based on the results in the magneto-elastic beam system, standing ILMs in the micro-cantilever array are assumed to have similar dynamics as the stationary waves. That is, it is conjectured that the traveling dynamics of ILM is governed by the phase structure around standing ILMs.

1.4   Purpose and Organization of Thesis

The main purpose of this study is to propose a new method to manipulate ILM in coupled cantilever arrays. In order to achieve this goal, the global phase structure regarding the dynamics of traveling ILM should be revealed, and can be changed as desired.

To propose new manipulation methods, the fundamental characteristics of ILM have to be clarified. Stability and local bifurcations are investigated in Chapter 3. The global phase structure and the dynamics of traveling ILM are discussed in Chapter 4. Chapter 2 is preliminary for the Chapters 3 and 4. A nondimensionalized equation of motion is first introduced by modeling a micro-cantilever array,

where ILMs were observed. The cantilever array is described by a coupled ordinary differential equation. Parameter settings and boundary conditions are also given. In addition, some general things needed to discuss ILM are briefly introduced. The mechanism of localization is shown by theoretical analysis in the linearized equation of motion. The classification of localized modes is also given in this chapter.

Chapter 3 discusses the local characteristics of ILM in coupled cantilever arrays. Firstly, based on the results in coupled magneto-elastic beam system, it is investigated whether ILMs coexist in the coupled cantilever array. Then the stability analysis is applied to the coexisting ILMs. The coexistence and the stability are the basis for investigations in the proceeding chapters. In this chapter, local bifurcations of ILM are also investigated for parameters in the coupled cantilever array. It is shown how ILMs exchange the stability. The influence of an impurity in the coupled cantilever array is also discussed.

Chapter 4 clarifies the global phase structure by calculating invariant manifolds of unstable ILMs. In particular, the change of the structure due to the change in stability change is discussed. Furthermore, the local changes of the structure are shown by adding an impurity. The dynamical behavior of traveling ILM is also discussed with the global phase structure. The discussion is based on the suggestion that the global phase structure governs the dynamics of a solution wandering in phase space [41, 43].

In Chapter 5, a new concept to manipulate ILM is proposed on the basis of the results in Chapter 3 and 4. First, the capture and release manipulation is numerically demonstrated. Next, the mechanism of the manipulation is explained based on the global phase structure. In addition to that, the attractive/repulsive manipulations, which are realized by M. Sato [35, 36], are also shown. The mechanism for the attractive/repulsive manipulations can be understood by the global phase structure.

In Chapter 6, a macro-mechanical cantilever array is proposed to confirm the results in Chapter 3 to 5. First, equation of motion describing the oscillations of cantilevers is described. Then, the validity of the modeling is experimentally confirmed by a frequency response of a cantilever. Several localized oscillations were observed experimentally and numerically. In addition, an attractive manipulation is demonstrated experimentally by adding an impurity. Finally, the mechanism of the manipulation in the experimental model is discussed numerically.

In Chapter 7, the conclusions of this study are summarized. Some proposals for the future works are also presented.

Chapter 2

Cantilever Array and Localized Solutions

Intrinsic localized mode is a spatially localized and temporally periodic solution in a nonlinear coupled oscillators array. A micro-cantilever array is one of the nonlinear coupled oscillators arrays which allow intrinsic localized modes to exist. In this chapter, the micro-cantilever array is modeled as a coupled ordinary differential equation. Experimental observations give parameter settings. In addition, fundamental topics related to spatially localized solutions are introduced for both linear and nonlinear cases. The analysis for the linear case gives the relationship between the frequency and the spatial decay rate of spatially localized solutions. A criterion is also presented for discussing the dynamical stability of intrinsic localized modes.

2.1 Micro-mechanical Cantilever Array

2.1.1 Schematic Configurations

Various types of nonlinear coupled ordinary differential equation (ODE) can exhibit intrinsic localized mode (ILM) [44]. Since ILMs were experimentally observed in a micro-cantilever array, mechanically coupled cantilever arrays have been a well known example of nonlinear coupled ODE exhibiting ILM. Here, we introduce a nonlinear coupled ODE describing motion of the tip of individual cantilevers.

The micro-cantilever is designed to observe ILMs and is fabricated by using photolithography technology [29]. A thin SiN_x film on a silicon substrate forms cantilevers and overhang [29]. In experiments, a di-element cantilever array, which has short and long cantilevers, was fabricated to make experiments easy. For sim-

7

(a) Eight cantilevers array with fixed ends.

(b) Schematic image of deformation of cantilevers and overhang.
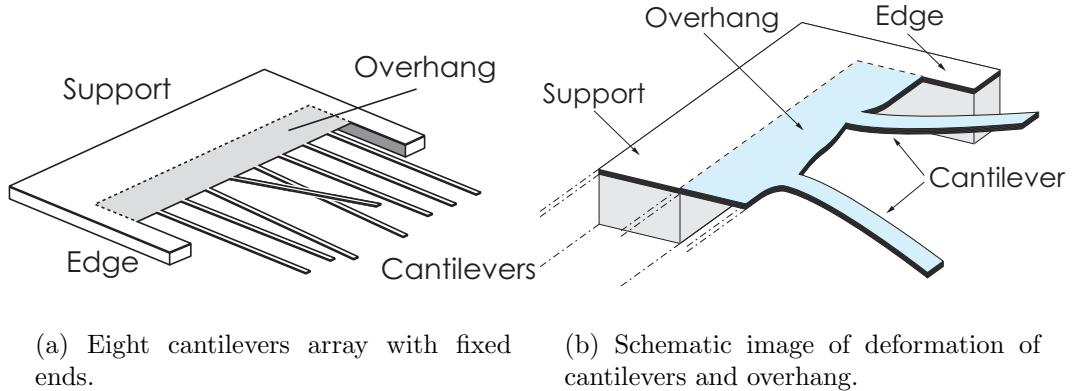
Figure 2.1: Schematic configuration of coupled cantilever array. The array has eight cantilevers arranged in one dimension. Both ends of the array are fixed by support.

Table 2.1: Size of cantilever array [34]

Each cantilever			
Length(ℓ)	55 μm	Width(w)	10 μm
Thickness(h)	300 nm	Pitch(p)	40 μm

Overhang			
Length(L)	60.0 μm	Thickness(h)	300 nm

SiN			
Density(ρ)	3.3×10^3 kg/m^3	Young's modulus(E)	300 GPa

plicity we can assume a mono-element cantilever array without loss of generality. A schematic configuration of the cantilever array is shown in Fig. 2.1(a). All homogeneous cantilevers are arranged with equal intervals in one dimension. The number of cantilevers is chosen as $N = 8$ because spatially localized solutions are mainly discussed. Adjacent cantilevers are coupled by the elastic deformation of overhang as shown in Fig. 2.1(b). The size of the array in Table 2.1 is determined as followed in Ref. [34].

8

2.1.2 Modeling of Cantilever Array

The vibration of cantilever is described by a partial differential equation. Since the cantilever is thin, Euler-Bernoulli beam theory can be applied to obtain the resonant frequencies and shape functions of the cantilever. The lowest resonant frequency corresponds to the first mode oscillation of cantilever. Because the micro-cantilever array is excited near the lowest frequency [34], we only focus on the first mode oscillation. The shape function of the first mode shows the maximum amplitude at the free end of cantilever. Here we describe the motion of the tip of cantilever by a simple spring-mass model which has the same resonant frequency as the original cantilever.

The nonlinearity of cantilever is arisen by more precise analysis. On the basis of the theoretical analyses [45–47], the cantilever tends to be hard as the deformation increases. This hardening nonlinearity is arisen from geometric nonlinearity. The hardening nonlinearity, which appears as a cubic term in the restoring force, has already been confirmed by experimental analyses [36, 47]. Therefore the cantilever is depicted by a spring-mass system with cubic nonlinearity in the spring. The coupling force caused by the overhang is modeled by the same way [36]. The difference in displacements of neighboring cantilevers causes the deformation of the overhang region. The restoring force also has a cubic nonlinearity [36]. Consequently, the motion of the micro-cantilever array is depicted by

$$
\begin{aligned}
m\ddot{Y}_n = &- k_{\mathrm{O2}}Y_n - k_{\mathrm{I2}}\left\{(Y_n - Y_{n-1}) + (Y_n - Y_{n+1})\right\} \\
&- k_{\mathrm{O4}}Y_n^3 - k_{\mathrm{I4}}\left\{(Y_n - Y_{n-1})^3 + (Y_n - Y_{n+1})^3\right\},
\end{aligned}
\tag{2.1}
$$

where Y_n denotes the displacement of the tip of the nth cantilever. The first and third terms represent the restoring force caused by bending each cantilever. The coupling force is depicted by the second and fourth terms. The mass denoted by m is assumed to correspond to the cantilever's mass given by $m = \rho wh\ell$. Table 2.2 shows the values of parameters in Eq. (2.1). By fundamental experiments reported by M. Sato, the linear on-site, inter-site, and the nonlinear on-site coefficients well coincide with the values obtained by the theoretical analyses [29, 34–36]. However, the experimentally estimated inter-site nonlinearity is quite smaller than the theoretical value. The assumptions applied to derive the inter-site nonlinearity may be a main reason for the large difference [48]. Thus, it is assumed that the ratio of linear coefficient between on-site and inter-site is equal to the nonlinearity ratio, namely, $k_{\mathrm{I2}}/k_{\mathrm{O2}} = k_{\mathrm{I4}}/k_{\mathrm{O4}}$.

Equation (2.1) does not include an energy dissipation term and an external excitation term. Although these terms should be considered when we discuss ILMs for real devices, we first investigate fundamental characteristics of ILM in the ideal system, namely, the conservative system. Because results in the conservative system

9

Table 2.2: Parameters of micro-cantilever array [34].

Symbol	Value	Symbol	Value
k_{O2}	0.303 kg/s^2	k_{I2}	0.0241 kg/s^2
k_{O4}	5×10^8 kg/s^{2}m^2	k_{I4}	$k_{O4}k_{I2}/k_{O2}$
m	5.46×10^{-13} kg		

can be fundamentals for studies of ILM in realistic systems. In addition, experimental studies is very often done in a situation of low energy dissipation. In fact, the micro-cantilever array was in high vacuum environment to reduce the air friction[1]. Then the energy dissipation and the external force are omitted. So, we consider the conservative system from Chapter 2 to Chapter 5. In Chapter 6, the energy dissipation is considered.

2.1.3 Nondimensionalization

To generalize the equation of cantilever array, Eq (2.2) is nondimensionalized by scaling $t \to \mathcal{T}\tau$, $Y \to \mathcal{X}u$, where $\mathcal{T}$ and $\mathcal{X}$ are unit values. The nondimensional equation of motion is induced as follows:

$$
\begin{aligned}
\ddot{u}_n = &- \alpha_1 u_n - \alpha_2 \left\{ (u_n - u_{n-1}) + (u_n - u_{n+1}) \right\} \\
&- \beta_1 u_n^3 - \beta_2 \left\{ (u_n - u_{n-1})^3 + (u_n - u_{n+1})^3 \right\},
\end{aligned}
\tag{2.2}
$$

where $\ddot{u}_n$ denotes the second order time derivative, $\dfrac{\mathrm{d}^2 u_n}{\mathrm{d}\tau^2}$. The unit for time is determined as $\mathcal{T} = \sqrt{m/k_{O2}}$, so that the resonant angular frequency is to be unity. Then α_1 is always equal to 1. The linear coupling coefficient is given by $\alpha_2 = k_{I2}/k_{O2} \simeq 0.1$. The nonlinear coefficients β_1 and β_2 are decided by scaling in length. Here the unit of length is set as $\mathcal{X} = \sqrt{m/k_{I4}}/(10\mathcal{T})$, so that $\beta_1 = 0.01$. As a result, the coefficient of nonlinear coupling term is defined as $\beta_2 = 0.01 k_{I4}/k_{O4} \simeq 0.001$. Values of unit time and length are in Table 2.3.

---

[1]The quality factor of a cantilever in high vacuum is evaluated about 10^4 [34].

Table 2.3: Nondimensionalized parameters.

Symbol	Value	Symbol	Value
α_1	1	$\alpha_2 = \alpha_1 k_{I2}/k_{O2}$	0.1
β_1	0.01	$\beta_2 = \beta_1 k_{I4}/k_{O4}$	0.001
$\mathcal{T}$	1.34 μs	$\mathcal{X}$	2.46 μm

2.1.4 Boundary Conditions and Total Energy

To discuss a spatially extended system, boundary conditions should be specified. For the coupled cantilever array, we mainly use the fixed boundary condition:

$$\begin{cases} u_0 = v_0 = 0, \\ u_{N+1} = v_{N+1} = 0, \end{cases} \tag{2.3}$$

where v_n corresponds to $\dfrac{\mathrm{d}u_n}{\mathrm{d}\tau}$, namely, the velocity of the nth cantilever. The coupled cantilever array with the fixed boundaries has the mirror symmetry with respect to the center of array. On the other hand, the periodic boundary condition

$$\begin{cases} u_0 = u_N, \\ v_0 = v_N, \end{cases} \tag{2.4}$$

is applied to both theoretical and numerical studies because the translational symmetry is maintained. The coupled cantilever array having the periodic boundary condition is called ringed array in this paper. The ringed array is focused when we discuss the influence of the fixed boundary condition.

One important thing is that Eq. (2.2) is a Hamiltonian system. The Hamiltonian is defined as follows:

$$\mathcal{H} = \sum_{n=0}^{N} \left\{ \frac{1}{2}v_n^2 + \frac{\alpha_1}{2}u_n^2 + \frac{\alpha_2}{2}(u_n - u_{n-1})^2 + \frac{\beta_1}{4}u_n^4 + \frac{\beta_2}{4}(u_n - u_{n-1})^4 \right\}. \tag{2.5}$$

The Hamiltonian corresponds to the total energy of the coupled cantilever array. Then $\mathcal{H}$ must be conserved during numerical simulations. The conservation is estimated to confirm the accuracy of numerical simulations. All numerical results in this paper include numerical errors under $\epsilon\mathcal{H}$, where $\epsilon = 10^{-12}$.

2.2 Localized Mode

2.2.1 Linear Wave Solution

Equation (2.2) has an obvious equilibrium point at $(u_n,\ v_n) = (0,\ 0)$ without relation to the position of site. The linearization around the equilibrium point leads the linearized equation of motion:

$$\ddot{u}_n = -\alpha_1 u_n - \alpha_2 \left\{ (u_n - u_{n-1}) - (u_n - u_{n+1}) \right\}, \tag{2.6}$$

where the number of oscillator is assumed to be infinite ($n \in \mathbb{Z}$), so that the boundary condition can be neglected. The general solution of Eq. (2.6) is easily obtained as

$$u_n(t) = A_1 e^{i(\kappa n - \omega t)} + A_2 e^{i(\kappa n + \omega t)}, \tag{2.7}$$

where A_1 and A_2 are arbitrary constants, κ corresponds to wave number, and ω denotes frequency [49]. Substituting Eq. (2.7) into Eq. (2.6) the relationship between the wave number and the frequency is obtained as follows:

$$\omega = \sqrt{\alpha_1 + 2\alpha_2(1 - \cos \kappa)}. \tag{2.8}$$

The relationship (2.8) is called dispersion relation. As shown in Fig. 2.2 the dispersion relation has both upper and lower bound with respect to frequency. It implies that the frequency of Eq. (2.7) is restricted to $\omega_0 \leq \omega \leq \omega_\pi$, where ω_0 and ω_π denote the angular frequency of the lower and the upper zone boundary, respectively (see Fig. 2.2).

2.2.2 Linear Localized Mode

Here we assume that the oscillator at $n = 0$ is vibrated with a frequency outside the band, namely, $\omega < \omega_0$ or $\omega > \omega_\pi$. Substituting $u_n = B_n e^{i\omega t}$ into Eq. (2.6) we obtain a difference equation [50]

$$B_{n+1} - 2\left(\frac{\alpha_1 - \omega^2}{2\alpha_2} + 1 \right) B_n + B_{n-1} = 0 \qquad \text{for} \quad n > 0, \tag{2.9}$$

where B_n denotes the amplitude of nth oscillator. Eq. (2.9) can be solved by putting $B_n = B_0 R^n$. Then we have the following quadratic equation

$$R^2 - 2\left\{ \frac{\alpha_1 - \omega^2}{2\alpha_2} + 1 \right\} R + 1 = 0, \tag{2.10}$$
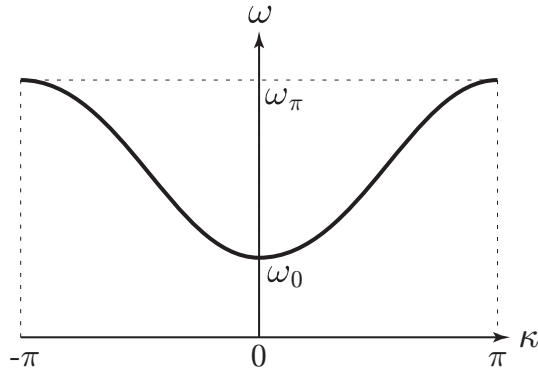
Figure 2.2: Dispersion relation for Eq. (2.6). $\omega_0 = \sqrt{\alpha_1}$ and $\omega_\pi = \sqrt{\alpha_1 + 4\alpha_2}$ represent the lower and the upper bound of frequency, respectively.

and the solutions

$$R = \frac{\alpha_1 - \omega^2}{2\alpha_2} + 1 \pm \sqrt{\left\{\frac{\alpha_1 - \omega^2}{2\alpha_2} + 1\right\}^2 - 1}. \tag{2.11}$$

If the frequency ω is inside the band ($\omega_0 \leq \omega \leq \omega_\pi$), R becomes a complex number. That is, a linear wave solution is obtained. For the case that the frequency is outside the band, R becomes a real number. To avoid divergence, $|R|$ has to be less than 1. Therefore, we have

$$R = \begin{cases} R_{\mathrm{A}} = \dfrac{\alpha_1 - \omega^2}{2\alpha_2} + 1 - \sqrt{\left\{\dfrac{\alpha_1 - \omega^2}{2\alpha_2} + 1\right\}^2 - 1} & \text{for} \quad \omega < \omega_0, \\[4mm] R_{\mathrm{O}} = \dfrac{\alpha_1 - \omega^2}{2\alpha_2} + 1 + \sqrt{\left\{\dfrac{\alpha_1 - \omega^2}{2\alpha_2} + 1\right\}^2 - 1} & \text{for} \quad \omega > \omega_\pi. \end{cases} \tag{2.12}$$

The amplitudes of oscillators thus exponentially decay as n is increased. The same equations as Eq. (2.12) is obtained for the case of $n < 0$ [50]. Therefore, the amplitude distribution has a peak at $n = 0$ with a tail decaying exponentially. Fig. 2.3 shows the shape of localized solutions. All oscillators vibrate in-phase for the case of $R = R_{\mathrm{A}}$ because R_{A} is positive (see Fig. 2.3(a)). On the other hand, neighboring oscillators vibrate in anti-phase for $R = R_{\mathrm{O}}$ as shown in Fig. 2.3(b). The sign of R_{A} and R_{O} is independent with respect to ω. Therefore, the shape of localized solution depends on the frequency. In addition, $|R|$ becomes large as $\omega - \omega_\pi$ or $\omega_0 - \omega$ increase. That is, the shape of localized solution tends to be sharp.

For one dimensional oscillators array, an impurity can cause the vibration that frequency is outside the band [50]. If α_1 at $n = 0$ is larger than the others, the
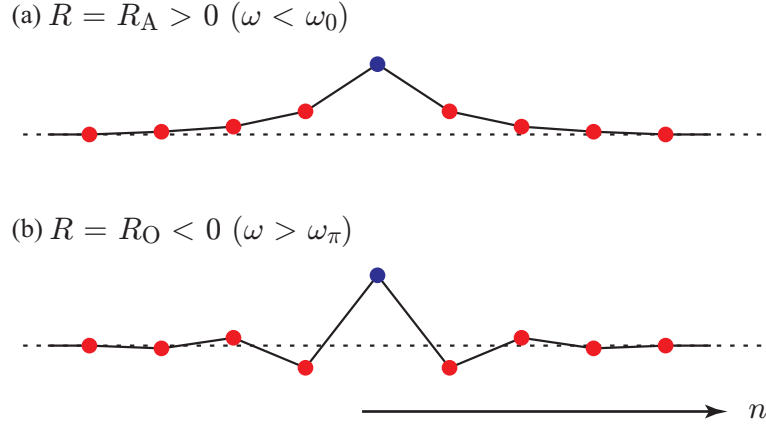
13

(a) $R = R_{\mathrm{A}} > 0$ $(\omega < \omega_0)$

(b) $R = R_{\mathrm{O}} < 0$ $(\omega > \omega_\pi)$

n

Figure 2.3: Localized mode for (a) below the lower zone boundary $(\omega < \omega_0)$ and (b) above the upper zone boundary $(\omega > \omega_\pi)$.

oscillator at $n = 0$ tends to vibrate with a higher frequency than the upper bound of band. For this case, a localized solution appears as in Fig. 2.3(b). The impurity oriented localized solution is called *linear localized mode*.

2.2.3   Intrinsic Localized Mode

For the linear coupled oscillator, a localized mode exists if and only if there is an impurity. However, a localized mode can appear without any impurity in nonlinear coupled oscillators arrays. Here we consider a simple nonlinear oscillator described by $\ddot{u} = -\alpha_1 u - \beta_1 u^3$. It is well known that the frequency of the solution of the nonlinear oscillator depends on its amplitude as shown in Fig. 2.4. If β_1 is positive, the frequency increases with amplitude, and *vise versa*. In other words, an oscillator with large amplitude vibration can be thought as an impurity for the linear case. Therefore, the vibration does not propagate if the oscillator in the nonlinear coupled oscillators array is excited with large amplitude. The localized oscillation is called *intrinsic localized mode* or *discrete breather*. The shape of ILM is determined by the sign of β_1 for this case. If β_1 is negative, the frequency tends to decrease as the amplitude increases. In the linear case, the frequency decrement occurs if α_1 is smaller than the others. Then ILMs for $\beta_1 < 0$ have a similar shape to Fig. 2.3(a). Such ILMs are called *acoustic* ILM. ILMs like Fig. 2.3(b) are called *optic* ILM. That is, for the positive/negative on-site nonlinearity, an optic/acoustic ILM can appear.
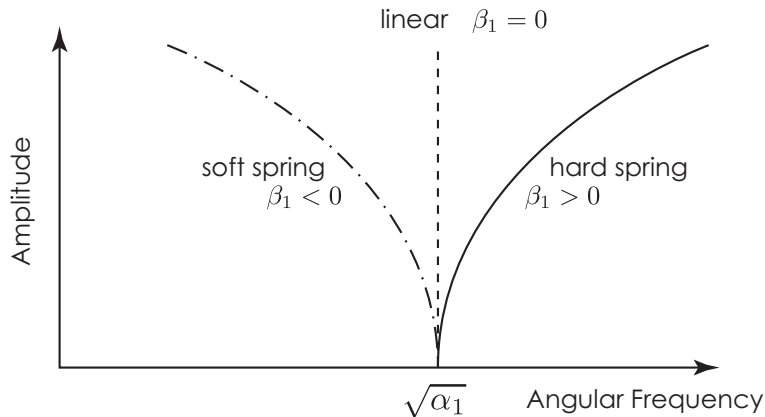
14

Figure 2.4: Relationship between amplitude and angular frequency of time-periodic solutions for $\ddot{u} = -\alpha_1 u - \beta_1 u^3$.

2.2.4 Spatial Symmetry of ILM

Intrinsic localized modes are roughly classified with its spatial symmetry into two kinds, "Sievers-Takeno mode (ST-mode)" and "Page mode (P-mode)" [51]. The ST-mode is odd-symmetric in amplitude distribution and centered on a site. This mode is found analytically by Sievers and Takeno [1]. On the other hand, the P-mode derived by Page [4] is even-symmetric in amplitude distribution. Two oscillators nearby the center of P-mode show the same amplitude. Fig. 2.5 illustrates these modes for both optic and acoustic ILMs.

2.2.5 Anticontinuous Limit for Existence Proof

Existence of ILM is rigorously discussed by using anticontinuous limit [52]. This technique is applicable to prove the existence of ILM in nonlinear Klein-Gordon lattices, which consist of linearly coupled nonlinear oscillators. The coupled cantilever array is one of nonlinear KG lattices when the nonlinear coupling coefficient is taken as zero, namely, $\beta_2 = 0$. In the anticontinuous limit, it is first assumed that nonlinear oscillators are arranged without any coupling. If an oscillator is excited while the others are kept at zero amplitude, a localized solution is obviously obtained because of no-couping. The existence of ILM is proven if the localized solution survives after introducing a weak coupling. For Klein-Gordon lattice the existence was proven by R. S. MacKay and S. Aubry [6]. Thus, the existence of ILM is guaranteed for Eq. (2.2) at a situation that $\beta_2 = 0$ and sufficiently small α_2.
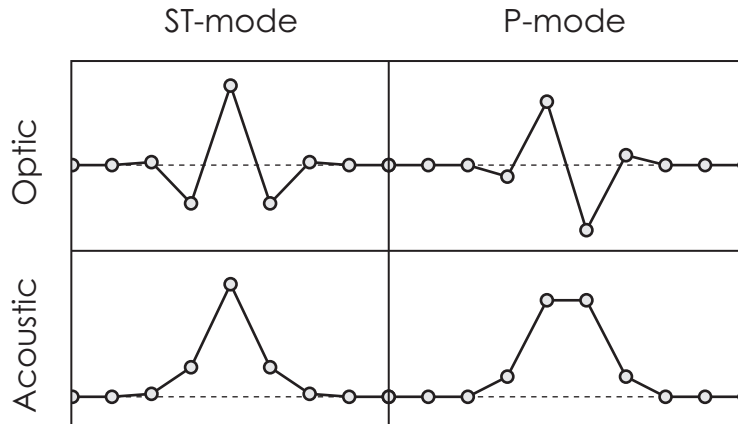
Figure 2.5: Sievers-Takeno (ST) mode and Page (P) mode for both optic and acoustic ILMs [44].

2.2.6 Obtaining Intrinsic Localized Mode

The anticontinuous limit can also be applied to a numerical method to find ILMs. The shooting method using Newton-Raphson method is a good numerical technique to obtain ILM [53, 54]. However, an initial guess should be carefully chosen to converge the Newton-Raphson method. That is, a good initial guess is necessary in order to obtain a desired solution. The anticontinuous limit helps to estimate initial guess for obtaining ILM [52]. At first, a spatially localized solution is obtained in the lattice without coupling. As a result, an amplitude and the corresponding frequency are obtained. Then the inter-site coefficient is slightly increased. Since the existence of ILM at a weekly coupled oscillators is guaranteed, the shooting method will converge to an ILM. The obtained ILM is used a new initial guess for more larger coupling coefficient. By iterating the above process, an ILM is obtained for the coupled cantilever array at desired parameters.

2.3   Stability of Periodic Solution

The stability of time-periodic solutions in Eq. (2.2) can be discussed in terms of the Floquet multipliers [55]. Let Γ be a periodic orbit for Eq. (2.2) as shown in Fig. 2.6. Here we introduce a hyperplane

$$\Sigma_p = \left\{ (\mathbf{u}, \dot{\mathbf{u}}) \in \mathbb{R}^{16} \mid u_p > 0, \dot{u}_p = 0 \right\}, \tag{2.13}$$

where p is the index of cantilever. The point where Γ intersects Σ_p is denoted by $\mathbf{x}^*$ in Fig. 2.6. This point can be a fixed point for the Poincaré map, defined as
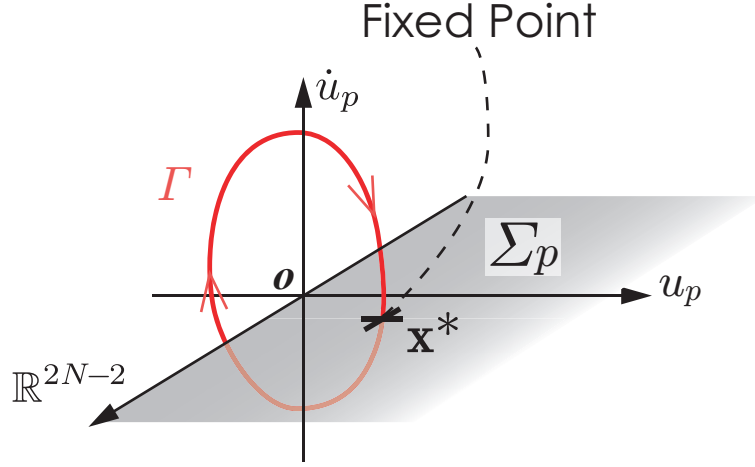
16

Figure 2.6: Time-periodic solution in $\mathbb{R}^{2N}$ and the corresponding fixed point, $\mathbf{x}^* \in \mathbb{R}^{2N-1}$, in a hyper surface Σ_p.

$\mathcal{P} : U \rightarrow \Sigma_p$, where $U \subseteq \Sigma_p$ is a neighborhood of $\mathbf{x}^*$. The stability of $\mathbf{x}^*$ for $\mathcal{P}$ reflects the stability of Γ for Eq. (2.2) [55].

The linearization of the map $\mathcal{P}$ leads to the linear map at the fixed point $\mathbf{x}^*$:

$$\xi_{k+1} = \mathcal{DP}(\mathbf{x}^*)\xi_k, \tag{2.14}$$

where ξ depicts a variation. The matrix $\mathcal{DP}(\mathbf{x}^*)$ has $2N - 1$ different eigenvalues. Then the stability of $\mathbf{x}^*$ is determined by whether the eigenvalues are located inside or outside unit circle in complex plane. The stability of ILM coincides with the corresponding fixed point because the eigenvalues of the matrix $\mathcal{DP}(\mathrm{x}^*)$ correspond to Floquet multiplies [55].

As mentioned above, Eq. (2.2) is a Hamiltonian system. If λ is an eigenvalue then $\bar{\lambda}$, $\frac{1}{\lambda}$, and $\frac{1}{\bar{\lambda}}$ are also eigenvalue of the matrix, where $\bar{\lambda}$ is the complex conjugate of λ. Therefore, a fixed point, $\mathbf{x}^*$, is not determined to be unstable if and only if all of eigenvalues are on unit circle as shown in Fig. 2.7(a). Otherwise, the fixed point is determined to be unstable (see Fig. 2.7(b)). The stability of ILM is not determined to be stable.

However Floquet multipliers are widely applied to discuss the stability of ILM [53]. The reason is that numerical simulations have shown that ILMs have maintained its energy concentration for a very long period if all eigenvalues are on unit circle. In addition, all Floquet multipliers of the ILMs enter into unit circle if the system has a damping term. For this reason, the ILMs is determined to be "marginally stable [53]". In this paper, we simply call "stable" for the stability of

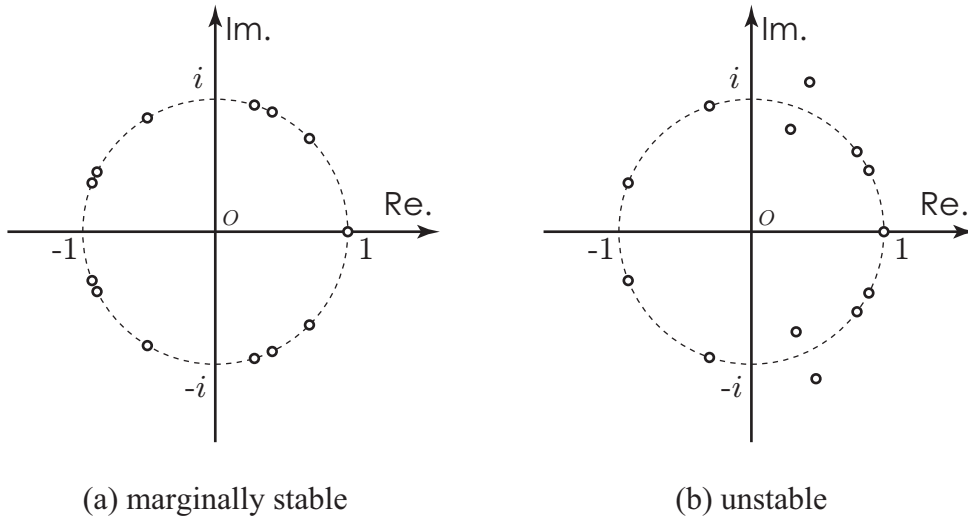(a) marginally stable   (b) unstable

Figure 2.7: Floquet multipliers for (a) marginally stable and (b) unstable ILMs [53].

the ILMs.

2.4 Remarks

The coupled differential equation obtained by modeling a micro-cantilever array has nonlinearities in both on-site restoring and coupling forces. This equation can represent both the Fermi-Pasta-Ulam (FPU) lattice and the nonlinear Klein-Gordon (KG) lattice, which frequently appear in researches discussing ILM/DB. In the FPU lattice, any on-site restoring force does not exist. The coupled cantilever array approaches to the FPU lattice when $\alpha_2 \to \infty$ and $\beta_2 \to \infty$. In the case of $\beta_2 = 0$, the coupled cantilever array coincides with a nonlinear KG lattice. Dynamical properties of ILM, such as the stability, are usually different between the FPU and the nonlinear KG lattices [21]. Then the fundamental characteristics of ILM will be strongly affected by the magnitude of β_2. Therefore the nonlinear inter-site coefficient is a key parameter. For this reason, coexistence and stability are investigated with respect to the coefficient, β_2, in the next chapter.

Numerically obtained localized solutions are confirmed to be ILMs by the theoretical analysis for the tail. It was shown that the tail is exponentially decay in space. So, the theoretical result can be applied even in the nonlinear lattice. The amplitude of ILM must be small except its locus. Then the shape of ILM asymptotically approaches to the linear localized mode which has the same frequency as the ILM. Therefore, a numerically obtained solution is identified as ILM if the

decay rate of tail coincides with the theoretically obtained value.

Chapter 3

Coexistence and Stability

This chapter presents intrinsic localized modes in coupled cantilever arrays. It is shown that several ILMs are obtained by using anticontinuous limit with different initial guesses. That is, ILMs coexists in a coupled cantilever array. The stability of coexisting ILMs is presented for two different coupled cantilever arrays. One is similar to a nonlinear Klein-Gordon lattice and the other is similar to a Fermi-Pasta-Ulam lattice. Here, a numerical method is applied to obtain ILMs for both arrays. As results, obtained ILMs are classified into two kinds by the spatial symmetry of amplitude distribution. The dependency on energy of coexisting ILMs is also discussed with bifurcation diagrams. At the low energy regime, ILMs will not exist because the effect of nonlinearity becomes smaller. Thus, the number of coexisting ILMs depends on the total energy of the system. On the other hand, the stability is determined by the spatial symmetry and flipped by the nonlinear inter-site coefficient. Bifurcation diagrams clearly show how the coexisting ILMs exchange the stability. In addition, the ringed array, where influences of the fixed boundaries are eliminated, is assumed for the analysis regarding to the stability change. In the ringed array, influences of an impurity are discussed with bifurcation diagrams. It is concluded that the impurity effectively affects coexisting ILMs where the stability change occurs.

3.1 Intrinsic Localized Modes in Coupled Cantilever Arrays

3.1.1 Coexisting ILMs

By using anticontinuous limit, several ILMs are obtained in coupled cantilever arrays with the fixed boundary condition that parameters are set to $N = 8$, $\alpha_2 = 0.1$, $\beta_2 = 0.001$, and $\mathcal{H} = 250$. The shape of amplitude distribution is shown in Fig. 3.1. ILMs shown in Figs. 3.1(a)–(e) correspond to ST-modes. They are obtained by initial guesses that only one cantilever is excited. P-modes are shown in Figs. 3.1(f)–(i). The initial guesses for P-modes are that two neighboring cantilevers are excited in anti-phase.

Coexisting ILMs in the cantilever array can be distinguished by the index number of cantilever oscillating with the largest amplitude. In this paper, the ST-mode standing at m-th site is called STm. For example, ST4 corresponds to the ST-mode centered on the 4th cantilever as shown in Fig. 3.1(d). The P-mode is depicted Pm-m' with $m' = m + 1$, because the P-mode has even symmetry in amplitude distribution. The locus of the P-mode is found at $m + 1/2$.

In the cantilever array, ST-modes and P-modes are alternately observed as shown in Fig. 3.1. In this parameter setting, all possible ILMs, ST1, ... ST8, P1-2, ..., P7-8, are found. The ST-modes are obtained by anticontinuous limit with the initial guesses that one cantilever is excited. Therefore, eight ST-modes are found because the number of cantilever is set at $N = 8$. On the other hand, two neighboring cantilevers are excited in anti-phase for the initial guesses of the P-modes. Since the both ends of array are fixed, P0-1 and P8-9 are not obtained. The initial guesses for P0-1 and P8-9 cannot be chosen because u_0 and u_9 are always fixed at zero. Therefore, seven P-modes are found at the cantilever array with the fixed boundaries.

The coexistence of ILM is also investigated for larger inter-site nonlinearity. The nonlinear inter-site coefficient β_2 is increased from 0.001 to 0.01. For this array, ST2, ..., ST7, P1-2, ..., P7-8 are found. However, ST1 and ST8 cannot be obtained by using anticontinuous limit. It implies that bifurcations occur between $\beta_2 = 0.001$ and 0.01. The bifurcations are investigated in Sec. 3.3.

3.1.2 Wave Forms

The time-development of displacement of each cantilever is shown in Fig. 3.2. Each cantilever shows a sinusoidal oscillation. A cantilever vibrates in anti-phase against
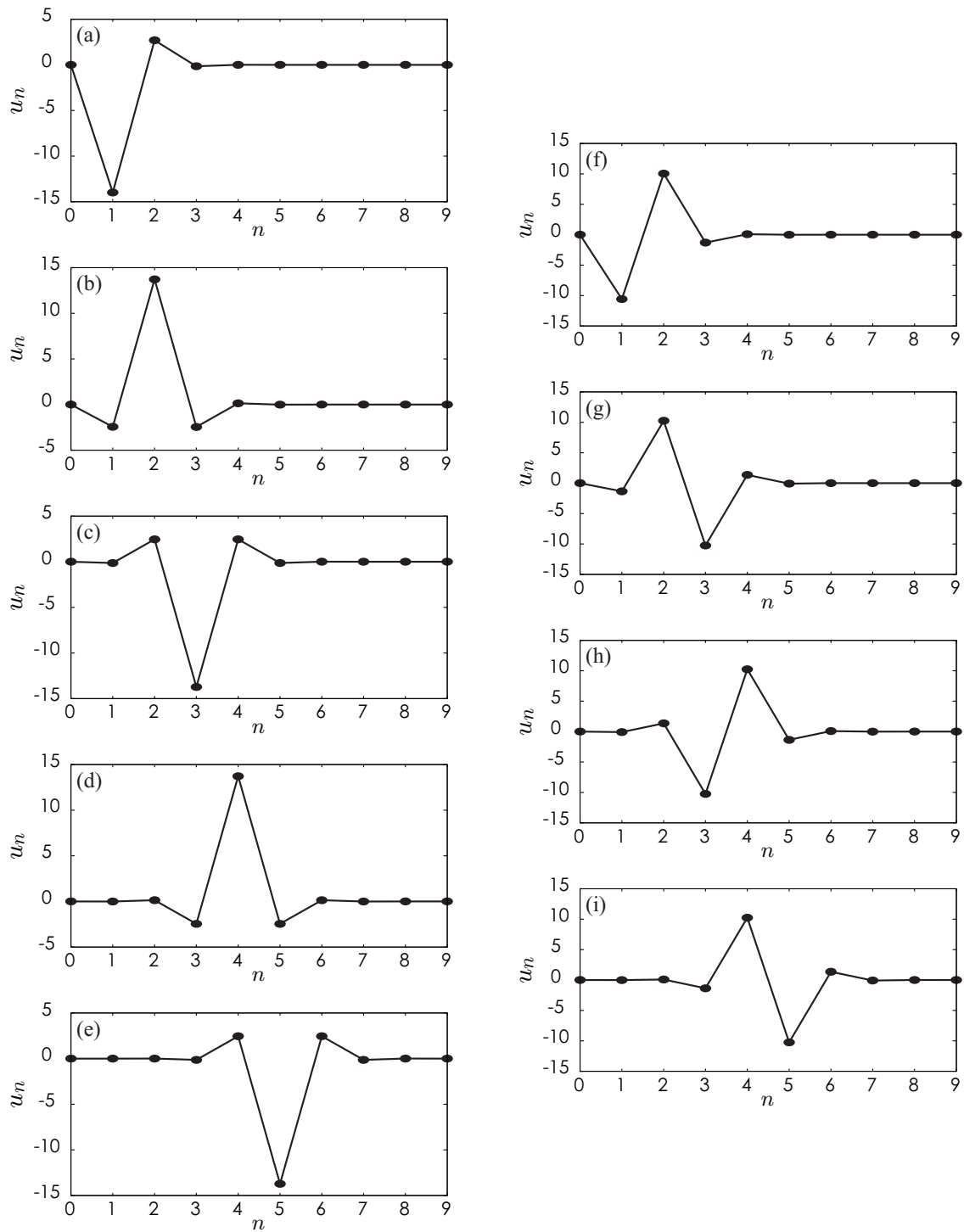
Figure 3.1: Coexisting ILMs at $\alpha_1 = 1$, $\alpha_2 = 0.1$, $\beta_1 = 0.01$, and $\beta_2 = 0.001$.
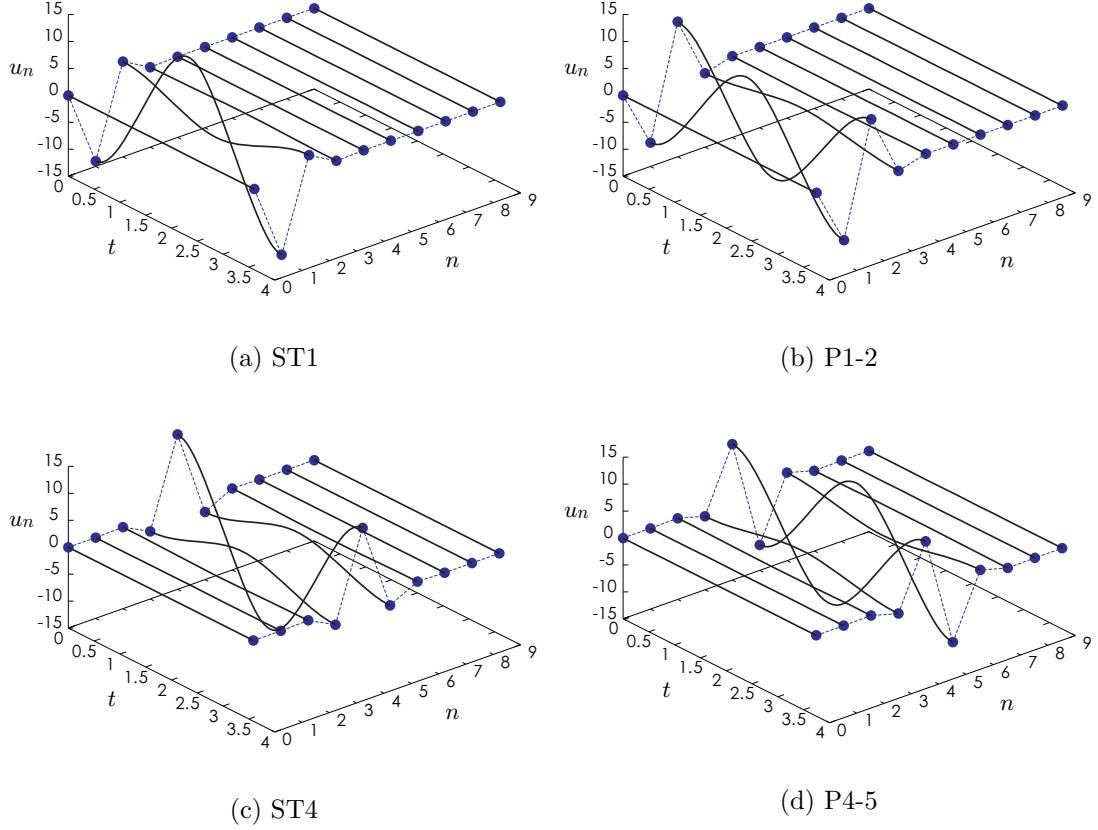
(a) ST1

(b) P1-2

(c) ST4

(d) P4-5

Figure 3.2: Wave form of each oscillator.

neighboring cantilevers because the coexisting ILMs are classified into optic ILM. In the conservative coupled cantilever array, the first derivative of u_n, namely, the velocity becomes zero at $t = kT/2, (k \in \mathbb{N})$ for all cantilevers. Then each value of u_n in Σ_4 corresponds to the amplitude of cantilever. That is, Fig. 3.1 shows the amplitude distribution.

3.1.3 Exponential Decay

The tail of ILM should be decayed exponentially. The linear analysis can be applied to the region where the amplitude of oscillator is small because coexisting ILMs shown in Fig. 3.1 are strongly localized. Fig. 3.3 shows the logarithmic plot of amplitude distributions for ST1, ST4, P1-2, and P4-5. The dotted lines are obtained by Eq. (2.12). The gradient of decaying amplitude of each ILM coincides with the corresponding theoretical line where the small amplitude region. Around the locus of

24

ILM, the gradient becomes small. In Eq. (2.12), an increment of the linear coupling coefficient reduces the decay rate. The coupling force is enhanced by the nonlinearity around the locus. Thus the differences between numerical and theoretical results are mainly caused by the inter-site nonlinearity. The gradient always becomes small around the locus of ILM as long as the inter-site nonlinear coefficient is positive.

The exponential decay of the tail of ILM shows that the localization mechanism of ILM is the same as the linear localized mode. In addition, the number of cantilever is enough to discuss the coexisting ILMs. As shown in Fig. 3.1, it seems that the coexisting ILMs are not affected by the fixed boundaries. That is, the coexisting ILMs are sufficiently localized at $\mathcal{H} = 250$. However, at the low energy regime, the coexisting ILMs will be affected by the boundary conditions. Because the decay rate tends to small as the total energy decreases. The effect of boundaries is discussed at the low energy regime in Sec. 3.2.

3.1.4 Stability of Coexisting ILMs

The stability of ILM depends on the symmetry of amplitude distribution in space [21]. As mentioned in Sec. 3.1.1, coexisting ILMs in the coupled cantilever array are classified into two kinds. Generally, one is stable if the other is unstable and *vise versa*. Floquet multipliers of ST4 and P4-5 at $\beta_2 = 0.001$ are shown in Figs. 3.4(c) and (d), respectively. All of the multipliers for ST4 are on unit circle. Thus ST4 is stable. As shown in Fig. 3.4(d), one of the multipliers is outside unit circle. That is, P4-5 is unstable. At $\beta_2 = 0.001$, all coexisting P-modes are unstable and ST-modes are stable. In addition, all unstable P-modes have only one multiplier outside unit circle. The stability of coexisting ILMs is the same as in nonlinear Klein-Gordon lattices [21]. In terms of the stability of ILM, the coupled cantilever array at $\beta_2 = 0.001$ is similar to the nonlinear KG lattices.

On the other hand, ST4 becomes unstable when β_2 is increased from 0.001 to 0.01. Fig. 3.5(c) shows the Floquet multipliers of ST4. One of the multipliers is clearly located outside unit circle. All coexisting ST-modes are unstable. The stability of P-modes is also flipped. The multipliers of P4-5 are shown in Fig. 3.5(d). All multipliers are on unit circle. Stable P-modes are also observed in Fermi-Pasta-Ulam (FPU) lattices [12]. ST-modes are unstable in the lattices. Thus, the cantilever array at $\beta_2 = 0.01$ is similar to the FPU lattices in terms of the stability of ILM.

The coupled cantilever array has both on-site and inter-site nonlinearity. Thus the ratio of nonlinearity β_2/β_1 determines whether the array is similar to a nonlinear KG or a FPU lattice. The stability of ST- and P-modes should be exchanged between $\beta_2 = 0.001$ and 0.01 because the stability of ILM is different between nonlinear KG and FPU lattices. Therefore, in the coupled cantilever array, bifurcations appear by
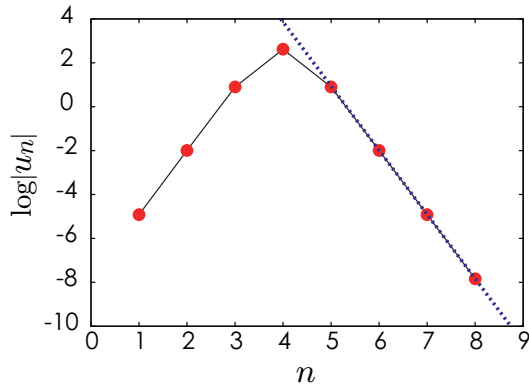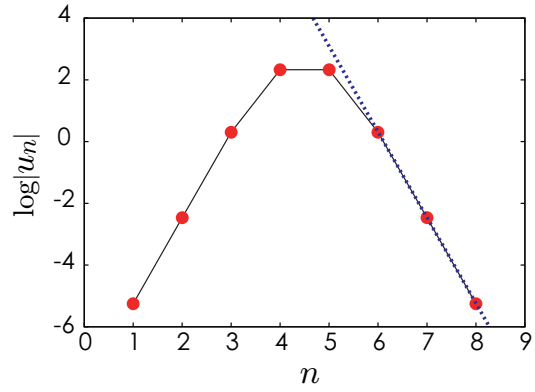
25
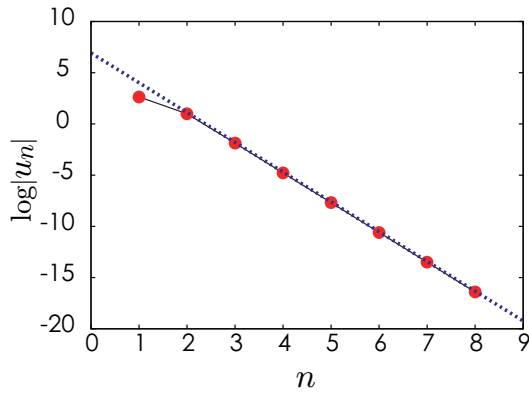
(a) ST1($T = 3.60728$)
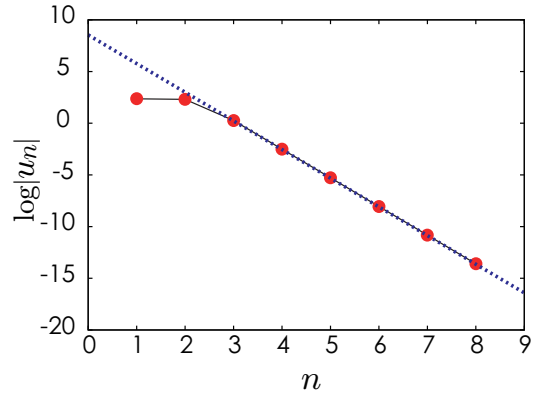
(b) P1-2($T = 3.75139$)

(c) ST4($T = 3.58959$)

(d) P4-5($T = 3.74723$)

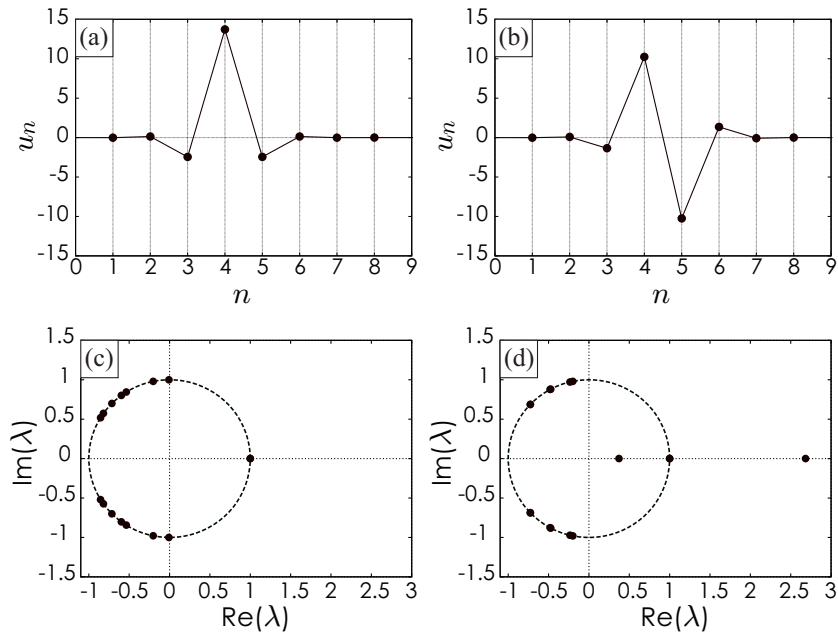Figure 3.3: Exponential decay of amplitude of coexisting ILMs. Dotted lines are drawn by Eq. (2.12).

Figure 3.4: Floquet multipliers of ST4 (b) and P4-5 (d) at $\beta_2 = 0.001$. Circle drawn by dashed curve indicates unit circle in complex plane.

varying the nonlinear inter-site coefficient[1] β_2, so that drastic change of the global phase structure is caused. The bifurcations will discussed in Sec. 3.3 in details.

3.2 Tangent Bifurcations

Coexisting ILMs show that the amplitude distributions are strongly localized, so that many ILMs are obtained. The shape of amplitude distribution is derived by Eq. (2.12) except the locus of ILM. That is, the gradient of the shape is determined by the frequency ω of ILM. The gradient tends to be large as the frequency increases. On the other hand, the gradient becomes small when the frequency decreases and approaches to the upper zone boundary. Since the number of cantilever is limited to be $N = 8$, coexistence of ILM will be changed with respect to the frequency. For the coupled cantilever array, the frequency increases with increasing the total energy of the system because all coefficients of Eq. (2.2) are positive. Then the total energy $\mathcal{H}$ is chosen as a parameter for investigating the coexistence of ILM.

---

[1]The value of β_1 is determined by the scaling for the homogeneous cantilever array. Then β_1 is kept 0.01 for all analysis in homogeneous cantilever arrays.
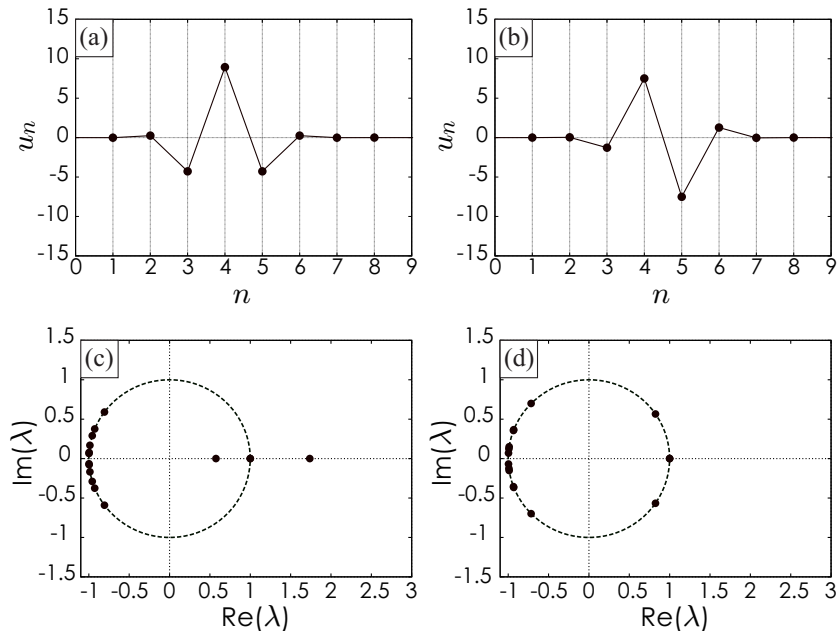
Figure 3.5: Floquet multipliers of ST4 (b) and P4-5 (d) at $\beta_2 = 0.01$. The total energy is set to $\mathcal{H} = 250$ as well as the case of Fig. 3.4.

To draw all coexisting ILMs in one bifurcation diagram, the collective variable is introduced as follows:

$$X_{\text{ILM}} = \frac{\sum_{n=1}^{8} n \times |u_n|}{\sum_{n=1}^{8} |u_n|}, \tag{3.1}$$

where $|u_n|$ is the absolute value of nth cantilever's displacement on the hyper surface Σ_4. The locus of ILM coincides with X_{ILM}. Then X_{ILM} takes integers for ST-modes and half-integers for P-modes. For example, $X_{\text{ILM}} \simeq 4$ for ST4 and $X_{\text{ILM}} \simeq 4.5$ for P4-5.

The bifurcation diagram of coexisting ILMs is shown at $\beta_2 = 0.001$ in Fig. 3.6. The total energy is swept from zero to 250. The amplitude distributions of coexisting ILMs at $\mathcal{H} = 250$ are shown in Fig. 3.1. The number of coexisting ILMs is not change while $\mathcal{H} > 50$. However, P1-2 and ST1 disappear for $\mathcal{H} < \mathcal{H}_3$, where $\mathcal{H}_3$ is the critical value when the bifurcation occurs. As the total energy decreases, coexisting ILMs disappear. Finally, ST4, P4-5, and ST5 degenerate to a stable solution, which is continuously connected to P4-5 in Fig. 3.6. The solution ultimately correspond to the upper zone boundary mode when the total energy is reduced to be zero, namely, $\mathcal{H} \to 0$. In other words, the upper zone boundary mode loses the stability and then ILMs appear. This bifurcation is called *tangent bifurcation* [21].

28
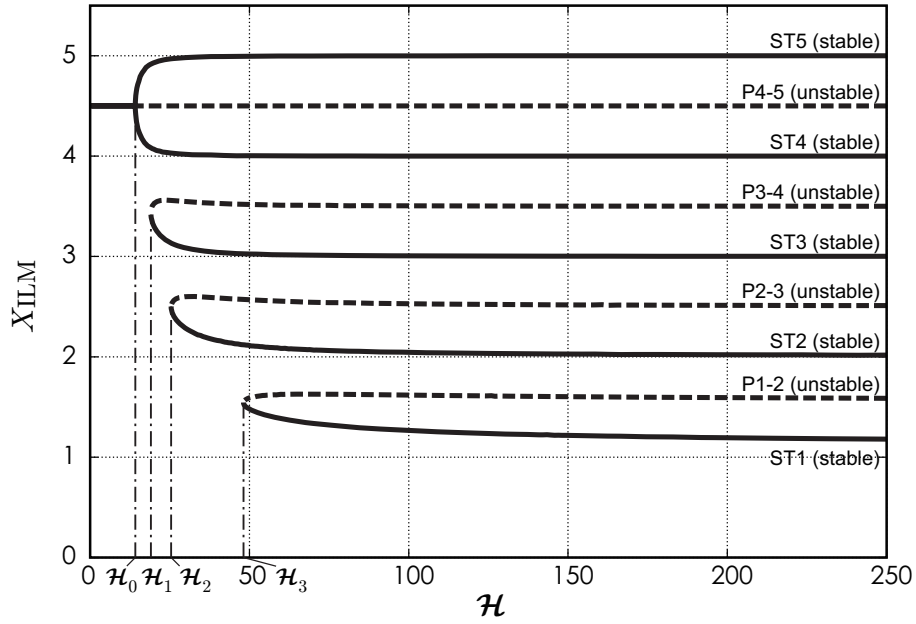
Figure 3.6: Bifurcation diagram for coexisting ILMs at $\beta_2 = 0.001$. Solid and dashed curves represent stable and unstable ILMs, respectively. The threshold energies are evaluated as follows: $\mathcal{H}_0 \simeq 14.2$, $\mathcal{H}_1 \simeq 19.0$, $\mathcal{H}_2 \simeq 25.4$, $\mathcal{H}_3 \simeq 48.1$.

Figure 3.7: Bifurcation diagram for coexisting ILMs at $\beta_2 = 0.01$. $\mathcal{H}_0 \simeq 5.06$, $\mathcal{H}_1 \simeq 9.09$, $\mathcal{H}_2 \simeq 88.8$.

Figure 3.7 shows the bifurcation diagram at $\beta_2 = 0.01$. The number of coexisting ILMs is also changed with $\mathcal{H}$. In this case, P1-2 coincides with ST2 instead of ST1 and disappears at $\mathcal{H} = \mathcal{H}_2$. P2-3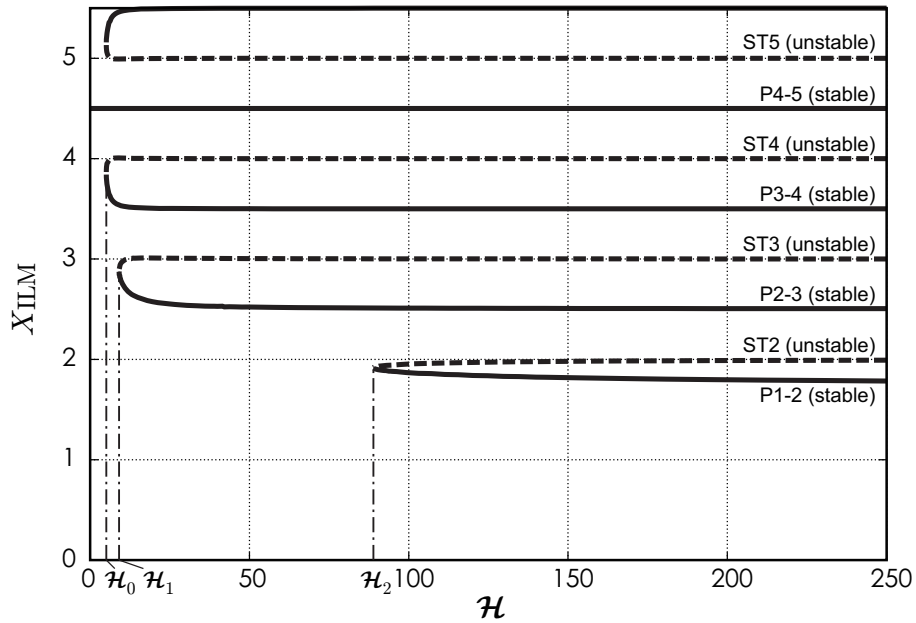 and P3-4 also disappeared with unstable ST-modes. However, P4-5 does not show any bifurcation to the other ILMs. The stability of P4-5 is always stable.

Bifurcation diagrams show that an ILM requires an energy to exist. The threshold energies depend on parameters of Eq. (2.2). The boundary conditions also affect the threshold energies. Figs. 3.6 and 3.7 clearly show that the threshold energies are increased as X_{ILM} approaches to the boundary. This implies that the influence of the boundaries becomes weak at high energy regime because the energy distribution of ILM is concentrated in narrow region.

3.3   Stability Change

The stability of coexisting ILMs is different between the array at $\beta_2 = 0.001$ and 0.01. ST-modes are stable at $\beta_2 = 0.001$ and unstable at $\beta_2 = 0.01$. Thus the stability should be flipped in the parameter region, $0.001 < \beta_2 < 0.01$. The locus and the stability of coexisting ILMs are shown with respect to β_2 in Fig. 3.8, where the total energy $\mathcal{H}$ is kept at 250. The figure clearly shows how the stability of coexisting ILMs is flipped with the change of the nonlinear inter-site coefficient. ILMs standing around the center of array, $2.5 < X_{\mathrm{ILM}} < 6.5$, almost simultaneously gain or lose stability at $\beta_2 \simeq 0.00545$. On the other hand, ST1 coincides with P1-2 at $\beta_2 \simeq 0.00238$ and disappears with increment of β_2. ST1 could not found for $\beta_2 > 0.00238$. The disappeared P1-2 appears again with ST2 at $\beta_2 \simeq 0.00716$. That is, the P1-2 makes a pair with ST2 for $\beta_2 > 0.00716$. As a result, ST1 is isolated from pairs of coexisting ILMs and then it is prohibited to exit. Therefore, the number of coexisting ILM is also changed with respect to β_2.

The enlargement of the bifurcations is shown in Fig. 3.9(a). Bifurcation points differ from each other even if ILMs are located around the center of array. The difference between bifurcation points results in the situation that unstable P-modes and ST-modes coexist. The unstable ST4 exists with the unstable P4-5 as shown in Fig. 3.9(a). The region, where the unstable P-modes and ST-modes coexist, is investigated in Sec. 3.4.

As shown in Fig. 3.9(a), the locus of stable ST3 is shifted from 3.0 toward 3.5 with β_2. The stable ST3 finally coincides with unstable P3-4 and disappears. The ST3 appears again as an unstable ILM with stable P2-3. Then the locus of stable P2-3 asymptotically reaches to 2.5 as β_2 increases. The region where ST3 does not exist is arisen between these bifurcation points. That is, ST3 has a parameter gap
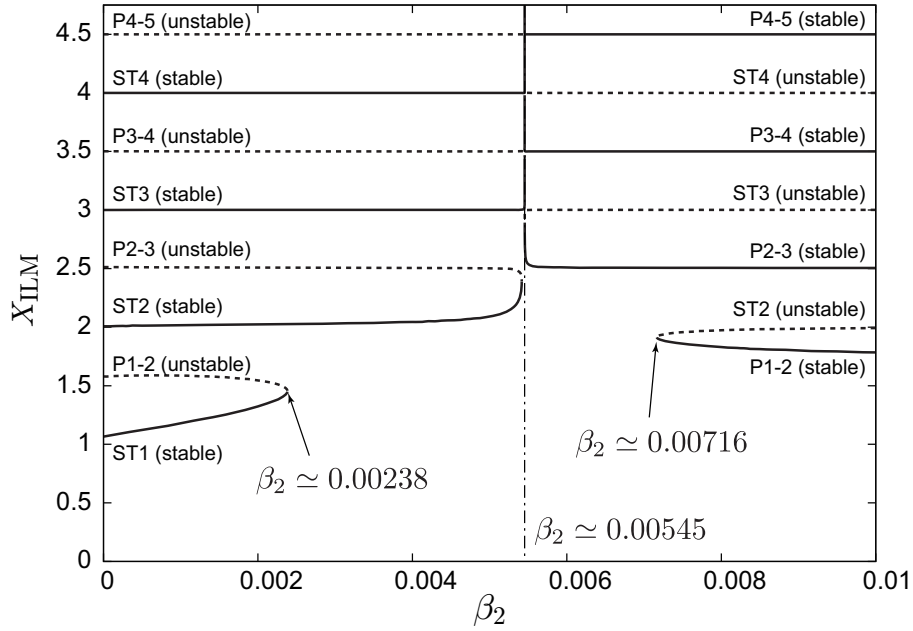
Figure 3.8: Locus and stability of coexisting ILMs. Solid curve corresponds to stable ILMs. Unstable ILMs are represented by dashed curve.

between stable and unstable modes. The parameter gaps also exist for P3-4 and ST4.

However, P4-5 does not have any parameter gap because of the reflectional symmetry about the center of array. That is, only P4-5 changes its stability without any discontinuity. Unstable and stable P4-5 continuously join at B_P. Two stable ST-modes join with P4-5 and disappear at the same condition. P4-5 changes only its stability at B_P.

The absolute value and argument of the Floquet multipliers for P4-5 are shown in Figs. 3.8(b) and (c). Two Floquet multipliers are on real axis for $\beta_2 < \beta_P$. One of them exists outside unit circle. The other stays inside unit circle. As β_2 increases, two Floquet multipliers approach toward $+1$ along real axis. At $\beta_2 = \beta_P$, these multipliers are conjoined at $+1$. After the bifurcation, their multipliers are on unit circle. Consequently, the bifurcation of ILMs on β_2 is classified to *saddle-node bifurcation* [56].
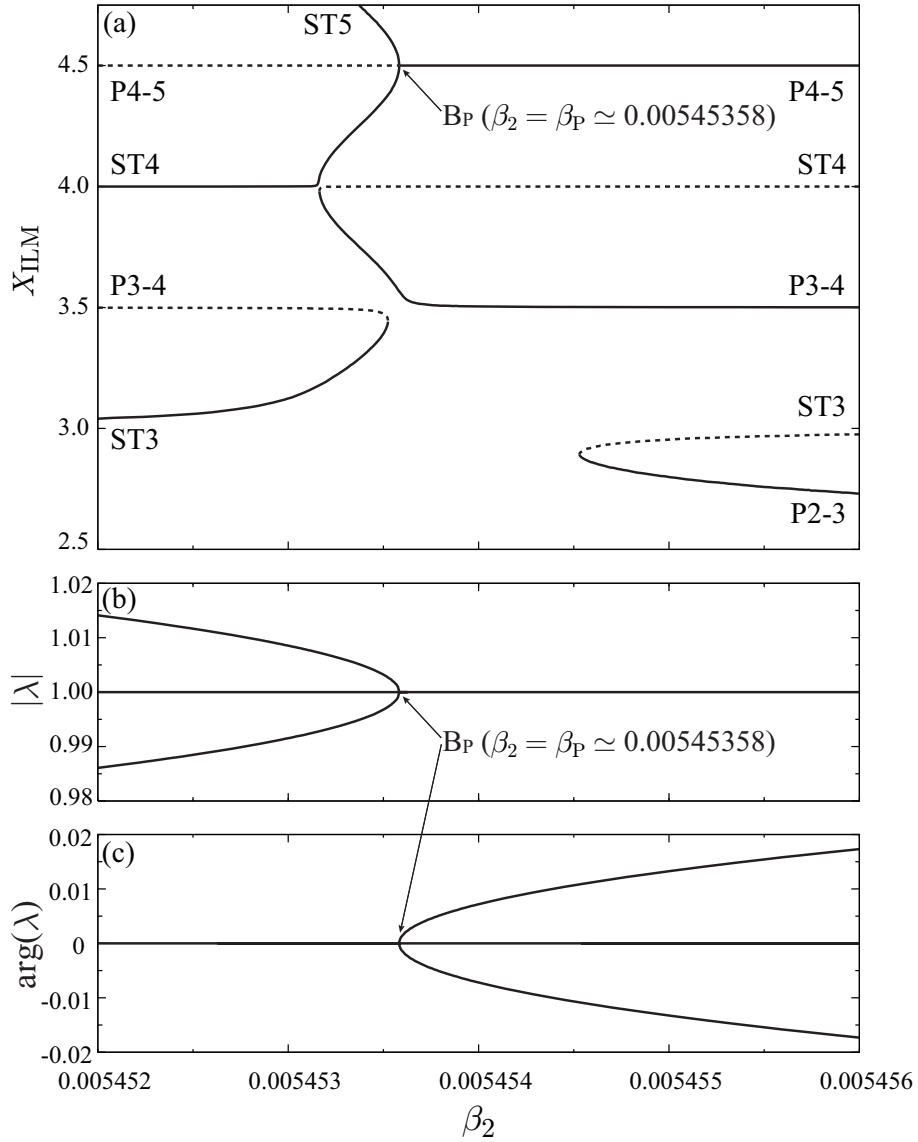
31

Figure 3.9: Stability change of ILMs to β_2 with $\alpha = 0.1$. (a) Position and stability of ILM. Solid curve is a set of stable ILM. Dashed curves correspond to the unstable ILMs. Absolute value (b) and argument (c) of Floquet multipliers of P4-5. The saddle-node bifurcation occurs at $\beta_2 \simeq 0.00545358$.

3.4 Analysis on Ringed Array

3.4.1 High Energy Limit

The bifurcation diagram shown in Fig. 3.8 includes the influence of the boundaries and has the dependency on energy. It suggests the influence of the boundaries that a bifurcation point tends to depart from $\beta_2 \simeq 0.00545$ as the locus of ILM approaches to the end of array. Then this parameter gap seems to be affected by the fixed ends. The influence of the boundaries can be reduced by substituting the boundary conditions from Eq. (2.3) to Eq. (2.4). On the other hand, according to the dependency on energy, the critical value at which P4-5 gains the stability, namely β_P, increases with $\mathcal{H}$. To eliminate the dependency, the linear coefficients are set to be zero. As a result, the equation which only consists of nonlinear terms is obtained as follows:

$$\ddot{u}_n = -\beta_1 u_n^3 - \beta_2 \left\{ (u_n - u_{n-1})^3 + (u_n - u_{n+1})^3 \right\}, \tag{3.2}$$

where the boundary condition is $u_0 = u_N$. The Hamiltonian is derived as follows:

$$\mathcal{H} = \sum_{n=1}^{N} \left\{ \frac{1}{2} v_n^2 + \frac{\beta_1}{4} u_n^4 + \frac{\beta_2}{4} (u_n - u_{n-1})^4 \right\}. \tag{3.3}$$

Equation (3.2) describes the dynamics of cantilevers at high energy regime. The contribution of the linear terms can be neglected in Eq. (2.2) because the nonlinear terms become dominant as the total energy increases. Thus, Eq. (3.2) is obtained by taking a limit $\mathcal{H} \to +\infty$. This limit is called *high energy limit*.

3.4.2 Stability Change

Since Eq. (3.2) is invariant against the total energy, the tangent bifurcations shown in Figs. 3.6 and 3.7 do not occur. However, the nonlinear inter-site coefficient β_2 is still included as a parameter in the equation. Therefore, we can investigate only the bifurcations related to the stability. The bifurcation diagram for Eq. (3.2) is shown in Fig. 3.10(a). The bifurcation point β_P is slightly increased. In addition, the parameter gaps are completely vanished. All ST-modes and P-modes are smoothly connected to corresponding modes. In the ringed array, the bifurcations related to the stability are simultaneously caused for each mode. The stability of all P-modes is simultaneously flipped at β_P as shown in Fig. 3.10(a). For coexisting ST-modes, the stability is flipped at $\beta_2 = \beta_{ST}$.

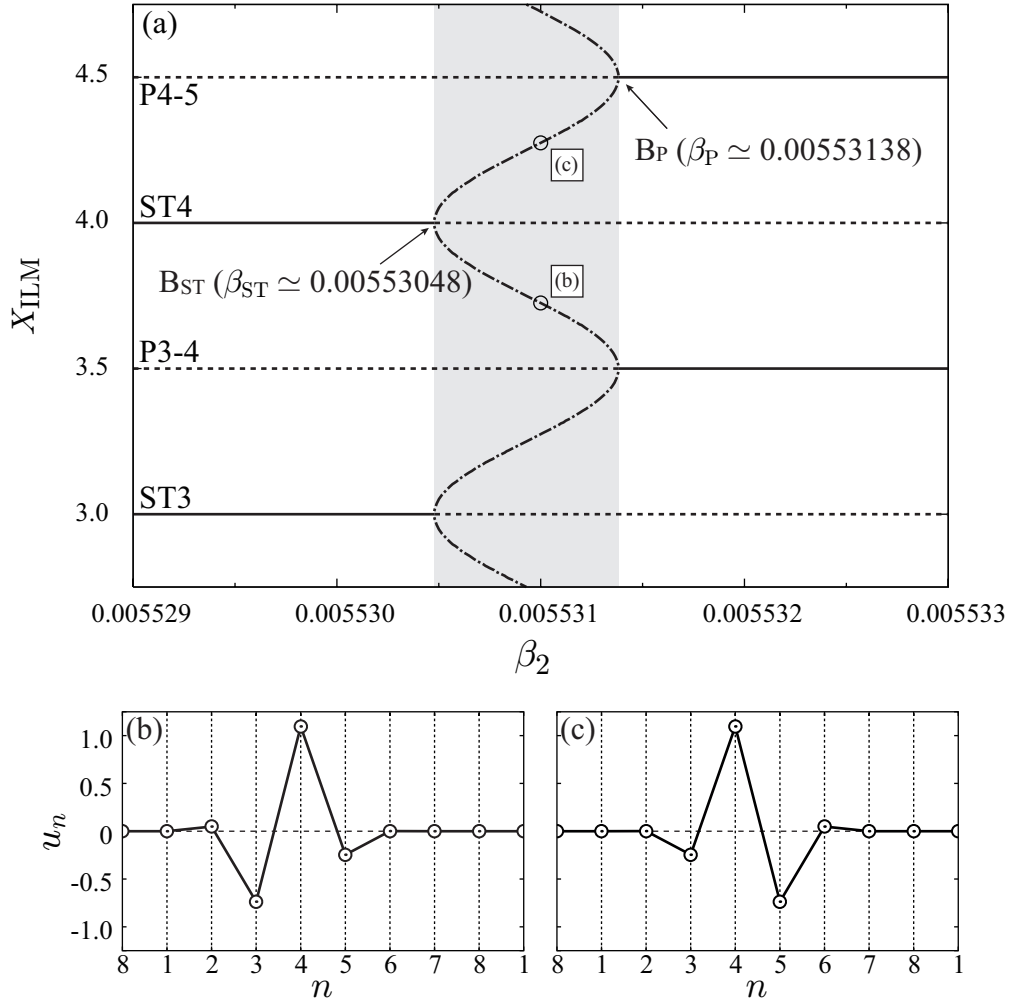Figure 3.10: (a) Stability change of ILMs with respect to β_2 in a ringed cantilever array without harmonic potentials. Solid line and dashed line represent stable and unstable ILM, respectively. Dash-dotted curves correspond to stable asymmetric ILMs. The asymmetric ILMs exist in the darkly hatched area, where ST-modes and P-modes are unstable. (b) and (c) Amplitude distribution of asymmetric ILMs.

3.4.3 Asymmetric ILM

As can be seen in Fig. 3.10(a), the critical values β_{P} and β_{ST} are different. This case corresponds to $\beta_{\mathrm{P}} > \beta_{\mathrm{ST}}$. Thus there exists the region in which all of the coexisting P- and ST-modes are unstable. The region is darkly hatched in Fig. 3.10(a). In the region, asymmetric ILMs, which are represented by dash-dotted curve, also coexist with P- and ST-modes. The amplitude distribution is shown in Figs. 3.10(b) and (c). These asymmetric ILMs are stable and stand between P- and ST-modes. Then they cannot be classified into P- or ST-mode.

3.4.4 Influence of Impurity

The parameter gaps shown in Fig. 3.8 are caused by the fixed boundaries. In this section, bifurcation diagrams for Eq. (2.2) with an impurity are shown. The impurity is added to the linear on-site coefficient α_1 at $n = 4$. Thus, the equation of motion is modified as follows:

$$
\begin{aligned}
\ddot{u}_n = & - \alpha_{1,n} u_n - \alpha_2 \left\{ (u_n - u_{n-1}) + (u_n - u_{n+1}) \right\} \\
& - \beta_1 u_n^3 - \beta_2 \left\{ (u_n - u_{n-1})^3 + (u_n - u_{n+1})^3 \right\},
\end{aligned}
\tag{3.4}
$$

where

$$
\alpha_{1,n} = \begin{cases} \alpha_1 & \text{for} \quad n \neq 4, \\ \alpha_1 + \alpha_{\mathrm{d}} & \text{for} \quad n = 4. \end{cases}
\tag{3.5}
$$

To reduce the influence of boundaries, the periodic boundary condition is assumed. The magnitude of impurity is assumed to be 0.1% of α_1, namely, $\alpha_{\mathrm{d}} = \pm 0.001$. The resulting diagrams are shown in Figs. 3.11(a) and (b). In both cases, the added impurity causes parameter gaps between stable and unstable ILMs except ST4. Stable ST4 is connected to unstable ST4 without any gap. However, the bifurcation point of ST4 is shifted by the impurity. The stability change of ST4 is caused at lower value of β_2 by adding the negative impurity as shown in Fig. 3.11(a). It seems that the direction of the shift depends on the sign of α_{d}.

Coexisting ILMs located around the impurity disappear when β_2 is close to the critical value of the stability change in the original system. That is, ILMs are strongly affected by disorders of cantilever array if the nonlinear inter-site coefficient is close to the critical value. In other words, the influence of impurity is enhanced. It implies that manipulations of ILM by adding impurity become possible by adjusting parameters of system. The manipulations using impurity are discussed in Chapter 6.
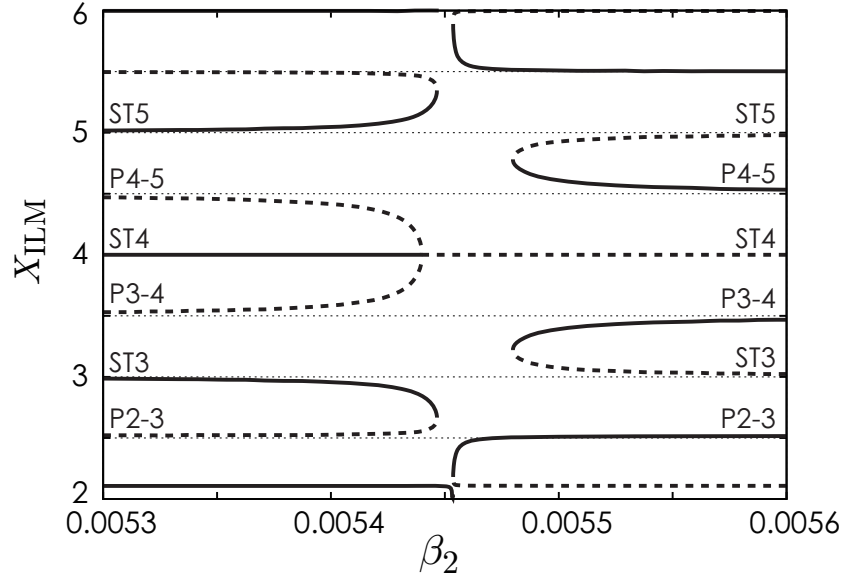
(a) $\alpha_d = -0.001$
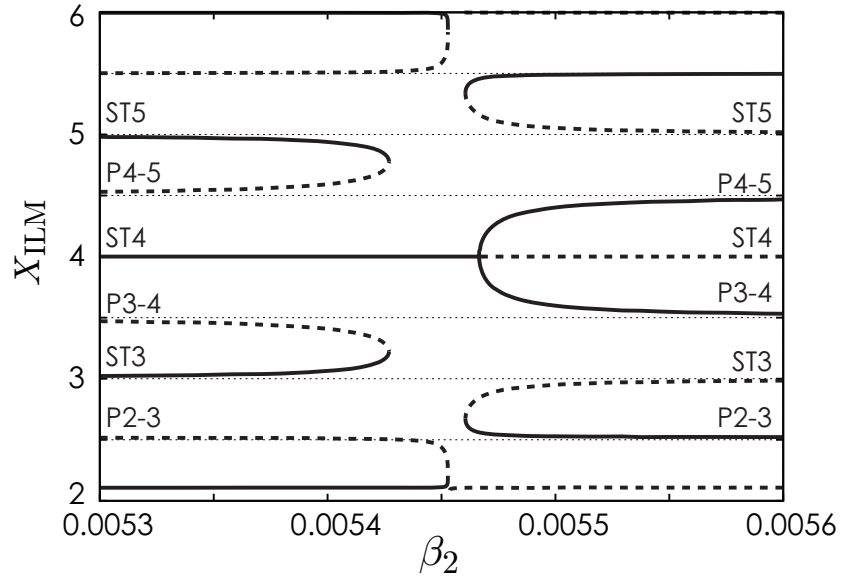
(b) $\alpha_d = 0.001$

Figure 3.11: Stability change of ILMs with respect to β_2 in a ringed cantilever array with an impurity. The impurity is added at $n = 4$. Parameters are set to $\alpha_1 = 1$, $\alpha_2 = 0.1$, $\beta_1 = 0.001$, $\mathcal{H} = 250$.

3.5   Remarks

In this chapter, we have numerically discussed the local characteristics of ILM. The coexistence and the stability were first shown for two types of coupled cantilever array. For the relatively small value of the nonlinear inter-site coefficient, ST-modes are stable and P-modes are unstable. The stability of coexisting ILMs is flipped at the other coupled cantilever array which has the large nonlinear inter-site coefficient. According to bifurcation analysis, it has been shown that the stability change is caused with saddle-node bifurcations by varying the nonlinear inter-site coefficient. In addition, the dependency on energy was also discussed. The total energy should be greater than the lowest threshold energy so that ILMs exist. This fact is one of differences between ILMs and linear localized modes.

Stability analysis in the ringed array where the linear terms are eliminated has revealed that the nonlinear inter-site coefficient governs the stability of ILMs. It suggests that the stability of ILM is determined by the balance of nonlinear terms. If the on-site nonlinearity is dominant, ST-modes is stable. On the other hand, P-modes are stable in the system where the inter-site nonlinearity is dominant. This allows to predict which modes appear in a realistic system. In addition, asymmetric ILMs were obtained in the region where all coexisting P- and ST-modes are unstable. Their amplitude distribution has no symmetry. These ILMs are not classified into ST- or P-modes. In the region $\beta_{ST} \leq \beta_2 \leq \beta_P$, twice number of ILMs coexist. The region still exists for a several hundred degree-of-freedom system. It is thus suggested that the asymmetric ILM independently exists with respect to the degree-of-freedom of system. In experiments, if the coupled cantilever array is precisely fabricated, the asymmetric ILM will be observed. However the region is quite narrow. In addition, analysis in the array with fixed boundaries suggests that the region is sensitive against impurities breaking the symmetry of the system. Thus the excitation of asymmetric ILMs seems to be difficult.

The influence of the fixed boundaries have also been discussed with relation to bifurcation diagrams. At low energy regime, ILM can exist only around the center of array because the gradient of the tail becomes small. Even in high energy regime, ILMs near the fixed boundaries disappear when the nonlinear inter-site coefficient is set around 0.005. Since the fixed boundaries are kinds of impurities, the influence of impurities will be enhanced near the critical value of the nonlinearity inter-site coefficient. It has been confirmed by comparing the periodic boundary condition to the fixed boundary condition. In the ringed array, all coexisting ST-modes simultaneously lose their stability at $\beta_2 = \beta_{ST}$ because of the translational symmetry. The fixed boundaries, which are equivalent to quite heavy impurities, break the symmetry of the array. As a result, the symmetry of the bifurcation diagram is broken. The parameter gaps between stable and unstable ILMs are

emerged. Even if an ILM stands near the center of the array, the parameter gap exists. In other words, the influence of impurity against ILM is enhanced near the critical values which change the stability of ILM.

The balance of nonlinearities is determined by the design of the array. Then the stability of ILM depends on the design of the cantilever array. It implies that the spatial symmetry of ILM is selectable in practical devices through the design. In addition, if the balance is adjustable in time, the stability will be controllable. Therefore, the nonlinearity of the system can be substantial parameter for controlling ILM.

To control ILM, the global behavior of ILM and the related phase structure should be investigated. Such global characteristics will be due to the local characteristics shown in this chapter. Based on the discussion in this chapter, the global phase structure and traveling ILMs are mainly focused in the next chapter.

Chapter 4

Global Phase Structure and Traveling ILM

In the previous chapters, it is revealed that intrinsic localized modes coexist in the array and the total energy of the system is a key to grasp the coexistence. Moreover, the stability of the coexisting ILMs depends on the nonlinear coupling coefficient. On the basis of the facts mentioned above, the global phase structure and the behavior of traveling ILMs are investigated in this chapter. The global phase structure is examined by focusing on the invariant manifolds of unstable coexisting ILMs. The structure formed by invariant manifolds is drastically changed when the bifurcation occurs. It is also shown that an impurity can be a seeds of transition of the global phase structure. Finally, the behavior of traveling ILMs is discussed with relation to the global phase structure. It is concluded that a traveling ILM wandering in the array is inherently governed by the phase structure formed by invariant manifolds of unstable ILMs.

4.1   Traveling Waves and Global Phase Structure

Traveling waves, that wander in a spatially extended system, were investigated on their behaviors in coupled magneto-elastic beam systems, which have a similar structure to the coupled cantilever array [40–42]. Several stationary waves instead of ILMs coexist in the system with complicated basin structures. In particular, the basin structure around unstable waves implies that there are heteroclinic connections of invariant manifolds governing unstable waves. That is, there is an orbit connecting unstable stationary waves. If a solution is generated on the invariant manifolds, the solution transits among the unstable stationary waves. Thus a wave travels through the system [41].

Intrinsic localized modes can be recognized as stationary waves because the locus of ILMs is independent of time. So, it is possible to assume that coexisting ILMs can behave in the similar dynamics to the stationary waves in the coupled magneto-elastic systems. That is, it is conjectured that a traveling dynamics of ILM is governed by the phase structure around coexisting ILMs.

4.2 One Dimensional Invariant Manifolds of Unstable ILMs

Let $\mathbf{x}^* \in \Sigma_4$ be a fixed point for the Poincaré map $\mathcal{P}$. Linearization around the fixed point leads a following equation:

$$\xi_{k+1} = \mathcal{DP}(\mathbf{x}^*)\xi_k, \tag{4.1}$$

where k denotes the number of iteration of the linearized map and $\mathcal{DP}(\mathbf{x}^*)$ is a $(N-1) \times (N-1)$ matrix. As mentioned in Chap. 2, the stability of the fixed point is determined by eigenvalues of the matrix $\mathcal{DP}(\mathbf{x}^*)$. Now we consider subspaces spanned by eigenvectors of the matrix. The subspaces is the direct sum of three subspaces [57]:

$$\text{the stable subspace, } E^s = \text{span}\{\mathrm{e}_s^1, \ldots, \mathrm{e}_s^{N_s}\},$$
$$\text{the unstable subspace, } E^u = \text{span}\{\mathrm{e}_u^1, \ldots, \mathrm{e}_u^{N_u}\}, \tag{4.2}$$
$$\text{the center subspace, } E^c = \text{span}\{\mathrm{e}_c^1, \ldots, \mathrm{e}_c^{N_c}\},$$

where $\mathrm{e}_s^1, \ldots, \mathrm{e}_s^{N_s}$ are the N_s eigenvectors whose eigenvalues are inside unit circle, $\mathrm{e}_u^1, \ldots, \mathrm{e}_u^{N_u}$ are the N_u eigenvectors whose eigenvalues are outside unit circle, and $\mathrm{e}_c^1, \ldots, \mathrm{e}_c^{N_c}$ are those whose eigenvalues are on unit circle. The hyper plane Σ_4 is equal to the direct sum of the subspaces, $E^s \oplus E^u \oplus E^c$. That is, $(N-1) = N_s + N_u + N_c$. Each subspace is called eigenspace. If an initial point is chosen in E^s, a sequence of points obtained by the iteration of the map exponentially approaches to the fixed point. Similarly, a sequence of points lying in E^u exponentially grows and those in E^c neither grows nor decay [57].

For the nonlinear map $\mathcal{P}$, the local stable and unstable manifolds of $\mathbf{x}^*$, W_{loc}^s, W_{loc}^u are defined as follows [58]:

$$W_{\text{loc}}^s(\mathbf{x}^*) = \{x \in U \mid \mathcal{P}^k(x) \to \mathbf{x}^* \text{ as } n \to \infty, \text{ and } \mathcal{P}^k(x) \in U, \forall k \geq 0\},$$
$$W_{\text{loc}}^u(\mathbf{x}^*) = \{x \in U \mid \mathcal{P}^k(x) \to \mathbf{x}^* \text{ as } n \to -\infty, \text{ and } \mathcal{P}^{-k}(x) \in U, \forall k \geq 0\}, \tag{4.3}$$

where $U \subset \Sigma_4$ is a neighborhood of the fixed point $\mathbf{x}^*$. According to stable manifold theorem [57], the local stable and unstable manifolds, W_{loc}^s and W_{loc}^u, have the same

dimensions as the eigenspaces E^s and E^u of the linearized system. In addition, the local invariant manifolds are tangent to the eigenspaces at $\mathbf{x}^*$. The local invariant manifolds W^s_{loc}, W^u_{loc} have global analogues W^s, W^u, obtained by

$$
\begin{aligned}
W^s(\mathbf{x}^*) &= \bigcup_{k \leq 0} \mathcal{P}^k(W^s_{\text{loc}}(\mathbf{x}^*)), \\
W^u(\mathbf{x}^*) &= \bigcup_{k \geq 0} \mathcal{P}^k(W^u_{\text{loc}}(\mathbf{x}^*)).
\end{aligned}
\tag{4.4}
$$

In this thesis, W^s and W^u are called *stable manifold* and *unstable manifold*, respectively.

Unstable ILMs have an eigenvalue outside unit circle in complex plane as shown in the previous chapter. Then unstable manifolds of the unstable ILMs are one dimensional in the hyper plane Σ_4. The unstable manifolds are denoted by $W^u(\cdot)$ with the name of ILM. For instance, unstable manifold of ST4 is denoted by $W^u(\text{ST4})$. Stable manifolds are also one dimensional and have the same global phase structure as the unstable manifolds because Eq. (2.2) is time-reversal. So, we only discuss the global structure of unstable manifolds.

4.3   Projection to Draw Global Structures

Invariant manifolds are globally extended in the phase space. Then the phase space and the configuration space are not suitable for discussing the global structure. Hence a projection $\mathcal{G} : \Sigma_p \to \mathbb{C}$ is introduced, where $\mathbb{C}$ depicts a set of all complex numbers. Here we define local potential energies as follows:

$$
\begin{aligned}
U_{\text{O}n}(u_n) &= \frac{\alpha_1}{2} u_n^2 + \frac{\beta_1}{4} u_n^4, \\
U_{\text{I}n}(u_n - u_{n-1}) &= \frac{\alpha_2}{2}(u_n - u_{n-1})^2 + \frac{\beta_2}{4}(u_n - u_{n-1})^4,
\end{aligned}
\tag{4.5}
$$

where $U_{\text{O}n}$ and $U_{\text{I}n}$ represent the on-site and the inter-site potential of nth oscillator, respectively. Then the energy distribution of the array is given by

$$
E(s) = \begin{cases}
\left. U_{\text{O}n}(u_n) + \frac{1}{2} v_n^2 \right|_{n=s} & \text{for} \quad s = n, \\
\left. U_{\text{I}n}(u_n - u_{n-1}) \right|_{n=s+\frac{1}{2}} & \text{for} \quad s = n - \frac{1}{2}, \\
0 & \text{for} \quad 2s \notin \mathbb{N},
\end{cases}
\tag{4.6}
$$

where s denotes a spatial coordinate of array. The projection is thus defined as [19]

$$
\begin{aligned}
h_k =& \mathcal{G}(\mathbf{x}_k), \\
=& \sum_{n=0}^{N+1} \left\{ \frac{1}{2}\dot{u}_n^2 e^{i\frac{2\pi}{N+1}n} + U_{\mathrm{O}n}(u_n)e^{i\frac{2\pi}{N+1}n} + U_{\mathrm{I}n}(u_n - u_{n-1})e^{i\frac{2\pi}{N+1}(n+\frac{1}{2})} \right\}, \\
& \left(= \int_0^{N+1} E(s)e^{i\frac{2\pi}{N+1}s}\mathrm{d}s \right),
\end{aligned} \tag{4.7}
$$

for the coupled cantilever array with fixed boundaries.

The projection $\mathcal{G}$ implies the inner product of the energy distribution of ILM and the sinusoidal wave whose wave number is unity in the array. Therefore, the phase of h_k, namely $\theta_k = \arg h_k$, in complex plane reveals the locus of the energy distribution. For the case of coexisting ILMs, the phase corresponds to the center of ILM. In addition, the velocity of an traveling ILM can be estimate from the differences between θ_k and θ_{k+1}, namely, $\Delta\theta_k = \theta_{k+1} - \theta_k$ [19].

4.4 Cyclic Structures

The structure of unstable manifolds is schematically drawn by Eq. (4.7). Invariant manifolds of unstable ILMs often show a cyclic structure in $(\theta_k, \Delta\theta_k)$ plane. As an example of the cyclic structure, unstable manifolds of P3-4 and P4-5 are shown in Fig. 4.1, where $\beta_2 = 0.001$ and $\mathcal{H} = 250$. In Fig. 4.1, stable and unstable ILMs are represented by open circles and squares respectively. Unstable manifolds are drawn by solid curves. The right branch of unstable manifolds of P3-4 forms the cyclic structure which lies between P3-4 and ST4. The unstable manifold seems to reach ST4. However, it turns around ST4 in the phase space as shown in Fig. 4.2. The other branches also appear unstable manifolds with the cyclic structure.

4.5 Connections between Vicinities of Unstable ILMs

Unstable manifolds can form another structure instead of the cyclic structure. In Fig. 4.3(a), a simple structure is shown. The total energy is slightly larger than $\mathcal{H}_0$ in Fig. 3.6. At the energy level, only three ILMs coexist, P4-5, ST4, and ST5. As shown in the figure, the unstable manifolds extend from P4-5 and return to P4-5 again. The manifolds approach to ST4. However, the enlargement around P4-5 (see Fig. 4.3(b)) shows that there is no-homoclinic structure in numerical estimation.
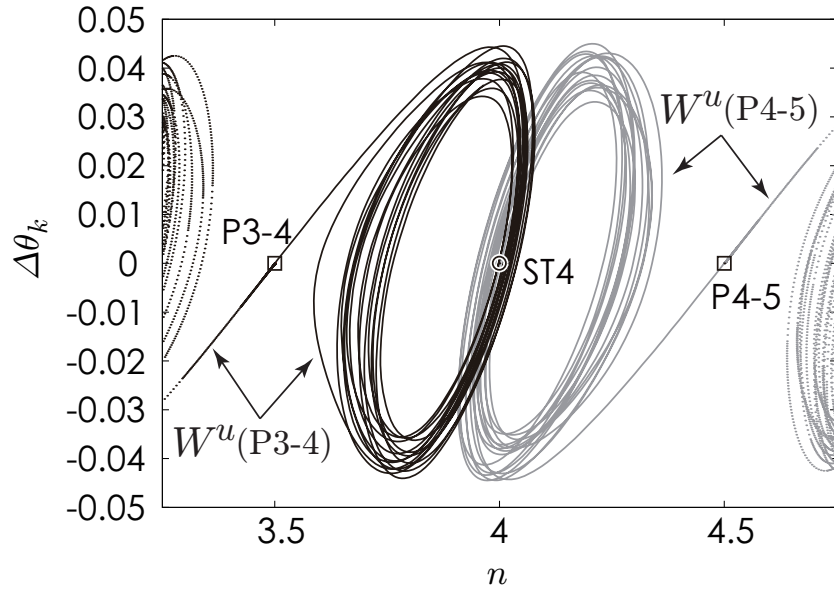
Figure 4.1: Unstable manifolds of P3-4 and P4-5. Coexisting ILMs are represented by circles and squares. The phase θ_k is converted to n by $n = (N+1)\theta_k/2\pi$.
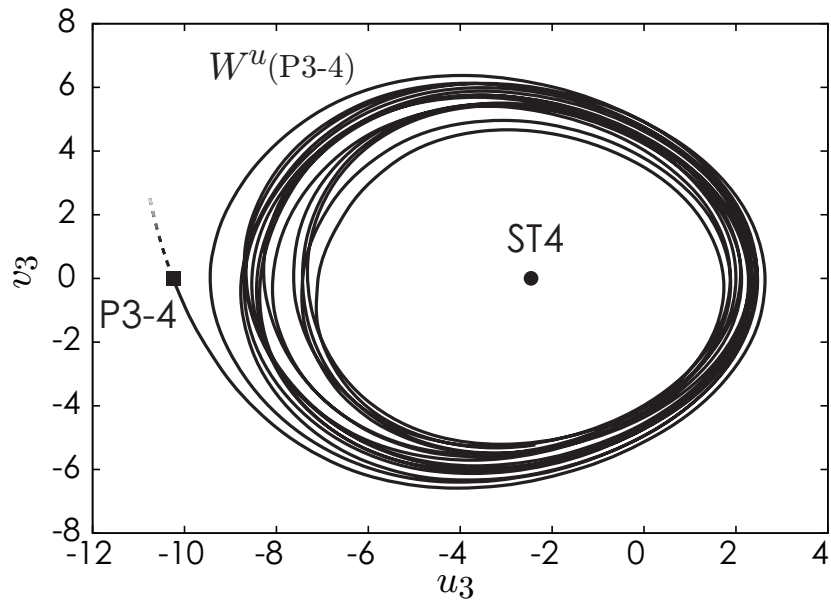

Figure 4.2: The left branch of unstable manifolds of P3-4 drawn in phase space.

43
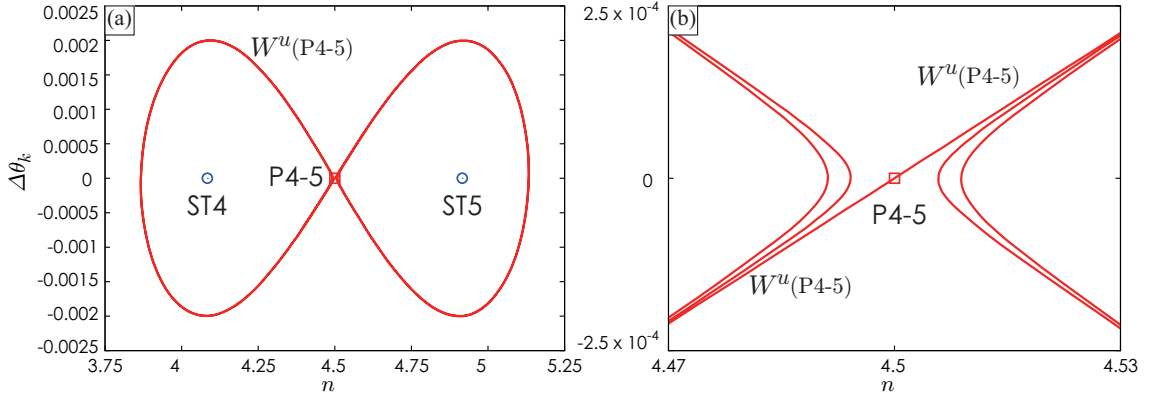
Figure 4.3: Unstable manifolds of P4-5 at $\beta_2 = 0.001$, $\mathcal{H} = 17$.
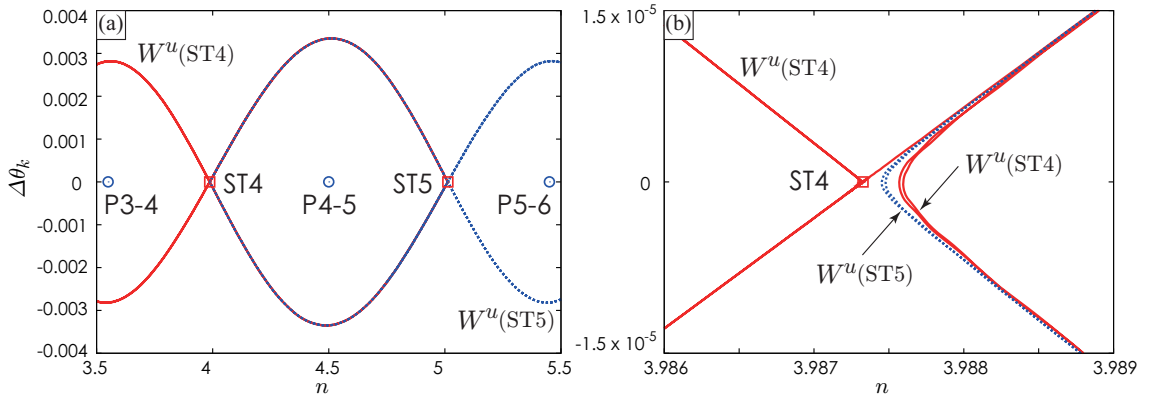

Figure 4.4: Unstable manifolds of ST4 and ST5 at $\beta_2 = 0.01$, $\mathcal{H} = 7$.

On the other hand, another simple structure is shown in Fig. 4.4(a). In this case, the nonlinear inter-site coefficient is set at $\beta_2 = 0.01$. The total energy is decided based on $\mathcal{H}_0$ at $\beta_2 = 0.01$. In Fig. 4.4(a), all coexisting ILMs at the energy level, $\mathcal{H} = 7$, are shown. There are two unstable ST-modes, ST4 and ST5. The solid and dotted curves represent $W^u(\text{ST4})$ and $W^u(\text{ST5})$, respectively. The right branch of $W^u(\text{ST4})$ and the left branch of $W^u(\text{ST5})$ are almost overlapped in Fig. 4.4. Fig. 4.4(b) shows the fact that the unstable manifold of ST5 lies nearby ST4. Although ST4 and ST5 seem to be connected by unstable manifolds, any heteroclinic connections are not identified in Fig. 4.4. However, the vicinities around unstable ILMs are connected each other. On the basis of the results on nonlinear waves in coupled magneto-elastic beam systems [41], the structure connecting the vicinities of unstable ILMs will be the key to the global dynamics of traveling ILMs.

44

4.6 Global Phase Structure Concerning ILMs

4.6.1 Drastic Change with the Stability Change

In the previous chapter, it was revealed that the stability of coexisting ILMs is flipped by the nonlinear inter-site coefficient β_2. Structures of unstable manifolds also depend on β_2 because of the stability change. Figs. 4.5(a)–(d) show structures of unstable manifolds at $\beta_2 = 0.003$, 0.005, 0.006, and 0.01. The stability change occurs between $\beta_2 = 0.005$ and 0.006. The right branch of W^u(P3-4) forms a cyclic structure centered at ST4 as shown in Fig. 4.5(a). The unstable manifold reaches the middle between ST4 and P4-5. The other manifolds in Fig. 4.5(a) show similar structure to the right branch of W^u(P3-4). By increasing β_2 from 0.001, the cyclic structures become wide.

The structure connecting the vicinities of unstable P-modes are observed at $\beta_2 = 0.005$. The right branch of W^u(P3-4) reaches the vicinity of P4-5 as shown in Fig. 4.5(b). The unstable manifold returns to the vicinity of P3-4 again (see inset of Fig. 4.5(b)). Other unstable manifolds show the same structure as the right branch of W^u(P3-4). Thus, the global phase structure becomes quite simple at $\beta_2 = 0.005$.

The global phase structure at $\beta_2 = 0.006$ is also simple as shown in Fig. 4.5(c). However, the structure is drastically changed. The connections between unstable P-modes are vanished. On the other hand, the vicinities of unstable ST-modes are connected each other. The drastic change is caused by the stability change which occurs between $\beta_2 = 0.005$ and 0.006. Unstable manifolds observed at $\beta_2 = 0.005$ is vanished with unstable P-modes by increasing β_2. ST-modes lose their stability by the stability change. Then invariant manifolds of ST-modes appear at $\beta_2 = 0.006$. Although the unstable manifolds do not show any homo- or heteroclinic connections as shown in the inset of Fig. 4.5(c), the unstable manifolds reach the vicinities of ST-modes. The connections between the vicinities of ST-modes are observed.

By increasing β_2 from 0.006 to 0.01, the simple structure is broken as shown in Fig. 4.5(d). The right branch of W^u(ST4) approaches to ST5; however, the unstable manifolds forms a cyclic structure surrounding stable P-modes. The nearest point of W^u(ST4) to ST5 tends to leave as β_2 increases. Thus, the unstable manifolds of ST-modes will show more complicated structure in the $(\theta_k, \ \Delta\theta_k)$ plane. In other words, the simple structure can be observed if β_2 is close to the critical value at which the stability change occurs.

The simple structure is similar to the phase space of a pendulum system derived by $\ddot{\phi} = -\sin\phi$. Stable and unstable ILMs correspond to the stable and unstable equilibrium points, respectively. The homoclinic orbit in the cylindrical phase plane $(\dot{\phi}, \ \phi)$ forms very similar structure to the unstable manifolds of unstable ILMs. By
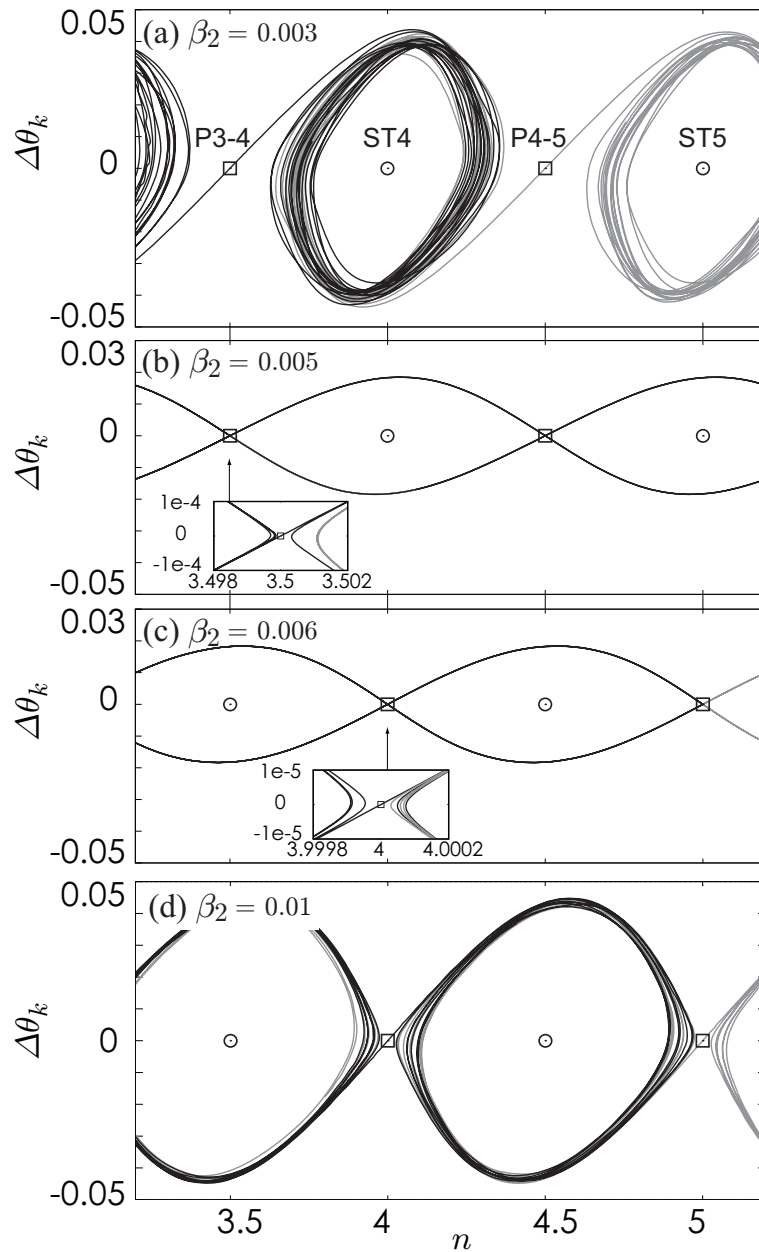
Figure 4.5: Coexisting ILMs and unstable manifolds at $\beta_2 = 0.003$(a), 0.005(b), 0.006(c), and 0.01(d). Structure of the vicinity of an unstable ILM is shown in the insets. Unstable manifolds are located very close to the unstable ILM. There is no homo- or heteroclinic connection.
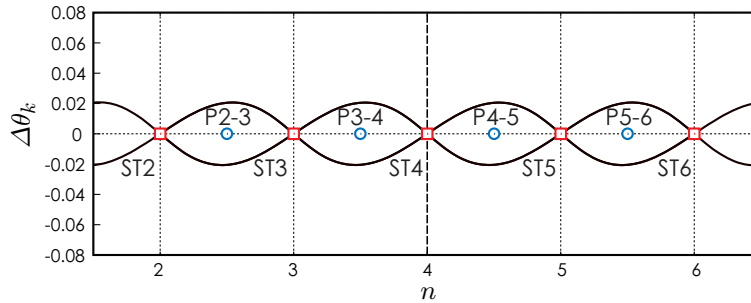
46

Figure 4.6: Unstable manifolds of ST-modes at $\beta_2 = 0.006$, $\mathcal{H} = 250$.

the similarity of the global phase structures, it is expected that the global dynamics of traveling ILM is also similar to in the pendulum system. This point will be discussed in Sec. 4.7.

4.6.2   Influence of Impurity

In the previous chapter, it was shown that an impurity strongly affects coexisting ILMs when β_2 is close to the critical value. Several ILMs around the impurity are vanished by adding the impurity. As shown in Sec. 4.6.1, the stability change is caused with the drastic change of the global phase structure. In this section, the influence of an impurity to the global phase structure is discussed at $\beta_2 = 0.006$. To eliminate the influence of the fixed boundaries, the ringed array is considered. The unstable manifolds of the ringed array without impurities are shown in Fig. 4.6. The nonlinear inter-site coefficient β_2 is set at 0.006. A quite simple structure which is similar to the pendulum is observed. In addition, the simple structure has translational symmetry because the ringed array has the symmetry.

The simple structure is changed by adding an impurity at $n = 4$. Figs. 4.7(a)–(c) show the global phase structures for $\alpha_d > 0$. The unstable manifold of ST4 are inside of the other unstable manifolds in Fig. 4.7(a). Then the connections between ST4 and neighboring ILMs are broken. P3-4 and P4-5 approach to ST4 as α_d increases as shown in Figs. 4.7(a) and (b). The loops surrounding P3-4 and P4-5 become smaller. As shown in Fig. 4.7(c), the unstable ST4 finally gains stability at $\alpha_d = 0.05$ and the unstable manifold of ST4 is vanished. The connection between ST3 and ST5 is observed at $\alpha_d = 0.05$. If a larger impurity added, the connection will be vanished with disappearances of ST3, ST5, P2-3, and P5-6.

For the case of $\alpha_d < 0$, unstable manifolds of ST4 are outside of the other unstable manifolds as shown in Fig. 4.8(a). The connections between ST4 and
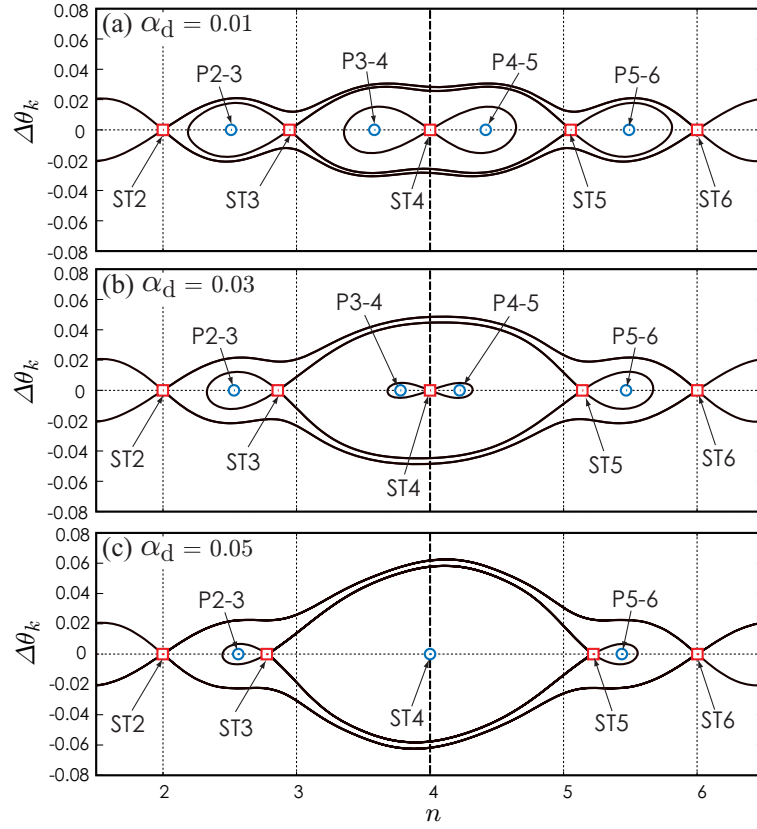
Figure 4.7: Unstable manifolds of ST-modes with impurity, (a) $\alpha_{\mathrm{d}} = 0.01$, (b) $\alpha_{\mathrm{d}} = 0.03$, (c) $\alpha_{\mathrm{d}} = 0.05$.
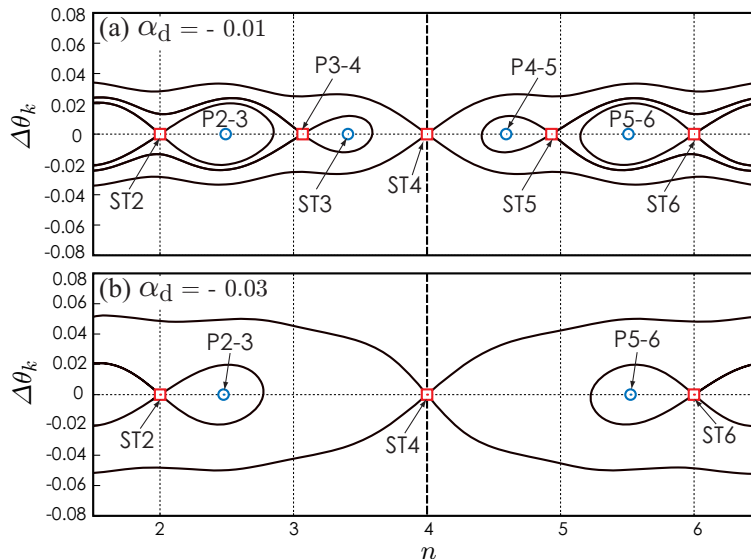
Figure 4.8: Unstable manifolds of ST-modes with impurity, (a) $\alpha_{\mathrm{d}} = -0.01$, (b) $\alpha_{\mathrm{d}} = -0.03$.

neighboring ILMs are also broken. The right branch of $W^u(\mathrm{ST4})$ returns to the vicinity of ST4. The unstable manifold of ST4 form a large loop which surrounds all coexisting ILMs and unstable manifolds except ST4. The loop becomes larger as the magnitude of the impurity is increased. The stability of ST4 is not flipped in this case. However, disappearances of coexisting ILMs are caused by varying α_{d} from -0.01 to -0.03. P3-4, ST4, P4-5, and ST5 disappear in Fig. 4.8(b). Therefore, unstable ST4 is isolated as well as the case of $\alpha_{\mathrm{d}} > 0$.

4.7 Behavior of Traveling ILM

4.7.1 Trajectory of Traveling ILM and Structure of Unstable Manifolds

In this section, the global dynamics of traveling ILMs are discussed based on the global phase structures. Here, it is assumed that a traveling ILM is generated by an initial point which is close to an ILM. If the ILM is unstable, the generated ILM will wander in the array [41]. In addition, the behavior of the traveling ILM depends on the global structure of invariant manifolds [41].

The global phase structure at $\beta_2 = 0.001$ is shown in Fig. 4.9(a). It is already

(a) Unstable manifold of P3-4 and P4-5.

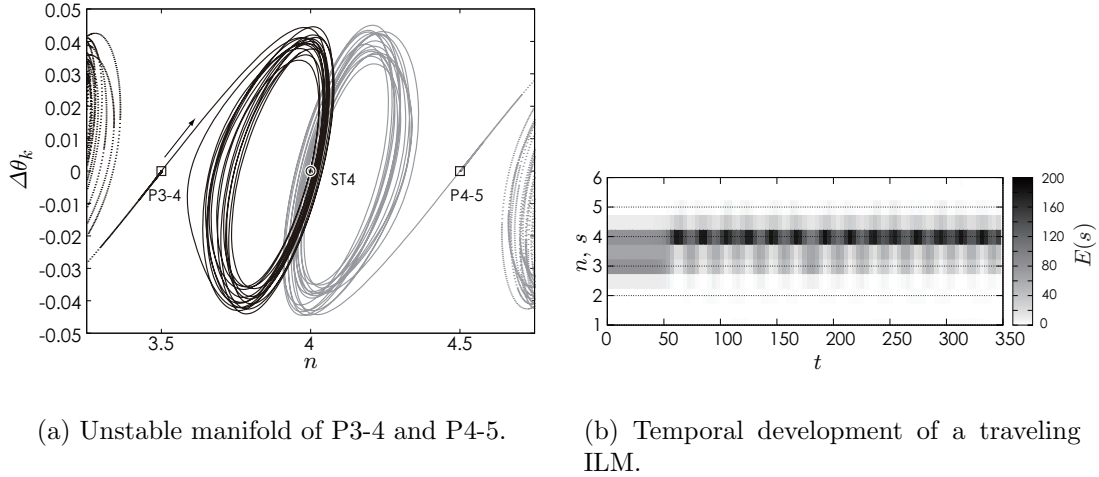(b) Temporal development of a traveling ILM.

Figure 4.9: (a): Unstable manifold of P3-4 and P4-5. Coexisting ILMs are represented by circles and squares. The arrow in the upper panel implies the direction of a perturbation against P3-4. The dots lying to the upper left are caused by definition of the hyper plane Σ_4. (b): Temporal development of a traveling ILM. Darkness correspond to the energy $E(s)$.

shown and discussed in Sec. 4.4. The unstable manifolds show cyclic structures. The cyclic structure formed by the right branch of W^u(P3-4) implies that a traveling ILM initially excited near P3-4 wanders between P3-4 and ST4. In Fig. 4.9(b), the behavior of a traveling ILM is shown with energy distribution given by Eq. (4.5). Darkness corresponds to high energy state. The traveling ILM is generated on the right branch of unstable manifold of P3-4. The arrow in Fig. 4.9(a) indicates the direction of the trajectory of the traveling ILM. At first, the energy mainly distribute on third and fourth sites and between them. The locus of the energy distribution is at 3.5. In other words, the traveling ILM stays near P3-4. The traveling ILM suddenly move to ST4 at $t \simeq 50$. The energy concentrate on the third oscillator at $t = 60$. Then the traveling ILM immediately returns to P3-4. Finally the traveling ILM reciprocally moves for a long period. The reciprocal behavior seems to be caused by the cyclic structure of W^u(P3-4). The locus of the traveling ILM is restricted in a region between $n = 3.5$ and 4. The region corresponds to the right branch of W^u(P3-4). Then the behavior of traveling ILM is predictable by the structure of unstable manifolds in the phase space.

The global phase structure at $\beta_2 = 0.01$ is shown in Fig. 4.10(a). The unstable manifolds also show cyclic structures. However, the cyclic structures of the unstable manifolds of ST-modes are centered at a stable P-mode. The unstable manifold

(a) Unstable manifold of ST3, ST4, and ST5.

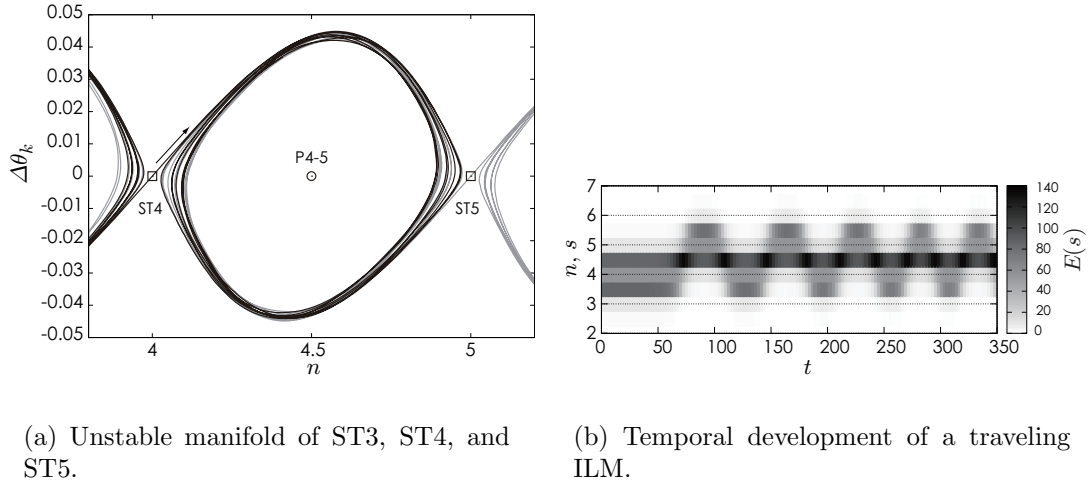(b) Temporal development of a traveling ILM.

Figure 4.10: (a): Unstable manifold of ST3, ST4, and ST5. (b): Temporal development of a traveling ILM.

of ST4 is located nearby ST5, and *vice versa*. Thus, a traveling ILM will move from the vicinity of ST4 toward ST5, if the traveling ILM is excited near the ST4. The behavior of a traveling ILM is shown in Fig. 4.10(b). The initial point of the traveling ILM is chosen on the right branch of W^u(ST4). Thus, the traveling ILM is initially located at $n = 4$ as shown in Fig. 4.10(a)(b). The traveling ILM begins to move at $t \simeq 50$. Then the traveling ILM reciprocally moves between ST4 and ST5. The reciprocal behavior corresponds to the structure of the unstable manifolds. In addition, the traveling ILM maintains its localized energy distribution while it wanders in the array. Therefore, the structure of unstable manifolds implies the behavior of a traveling ILM which is generated near an unstable ILM.

4.7.2   Sensitive Dependence on Initial Condition

The simple phase structures, which are similar to a pendulum system, appear if β_2 is close to the critical value at which the stability change occurs. Analogous to the case of a conservative pendulum system, it is expected that the invariant manifolds of unstable ILMs can be separatrices. So, the behaviors of traveling ILMs become completely different even if the initial points of the traveling ILMs are close each other. Here we take two initial points, IP1 and IP2, as shown in Fig. 4.11, where $\beta_2 = 0.006$ and $\mathcal{H} = 250$. IP1 is inside the cyclic structure formed by unstable manifolds of unstable ST-modes, whereas IP2 is outside the structure. The trajectory started at IP1 turns clockwise and the other trajectory moves to the
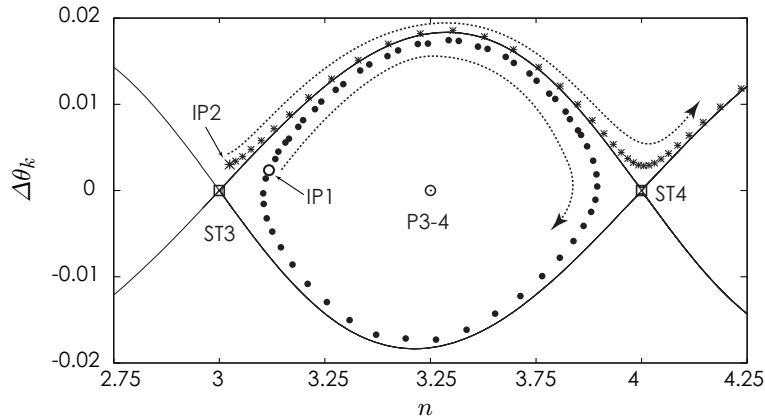
Figure 4.11: Unstable manifolds of unstable ILMs. An open circle and open squares represent stable P-mode and unstable ST-modes, respectively. Unstable manifolds of unstable ST-modes are drawn by solid curves. Filled circle and asterisks correspond to trajectories of traveling ILMs generated near ST3. Time-development of energy concentration for both trajectories is shown in Fig. 4.12.

right hand side. The corresponding time-development of energy concentrations is shown in Fig. 4.12. For the case of IP1, the locus of the high energy concentration reciprocally moves between $n = 3$ and 4. On the other hand, a traveling ILM started from IP2 wanders beyond ST4. Although IP1 and IP2 are close to each other, the behavior of the ILMs show completely different feature. It suggests that the structure of unstable manifolds determines the behavior of traveling ILM.

4.8   Remarks

In this chapter, the global phase structure was investigated by calculating unstable manifolds of unstable ILMs. It was observed that an unstable manifold forms a loop surrounding a stable ILM. The loop is called cyclic structure. Connections between vicinities of unstable ILMs were also identified. In addition, the drastic change of the global phase structure is caused when the stability change occurs. It was also shown that the global phase structure tends to be simple when the nonlinear inter-site coefficient is varied to the critical value causing the stability change. In the simple structures, the vicinity of each unstable ILM is connected each other by the unstable manifolds.

The simple structure can be changed by adding an impurity if β_2 is set near the critical value. A positive α_d locally changes the simple structure. However,
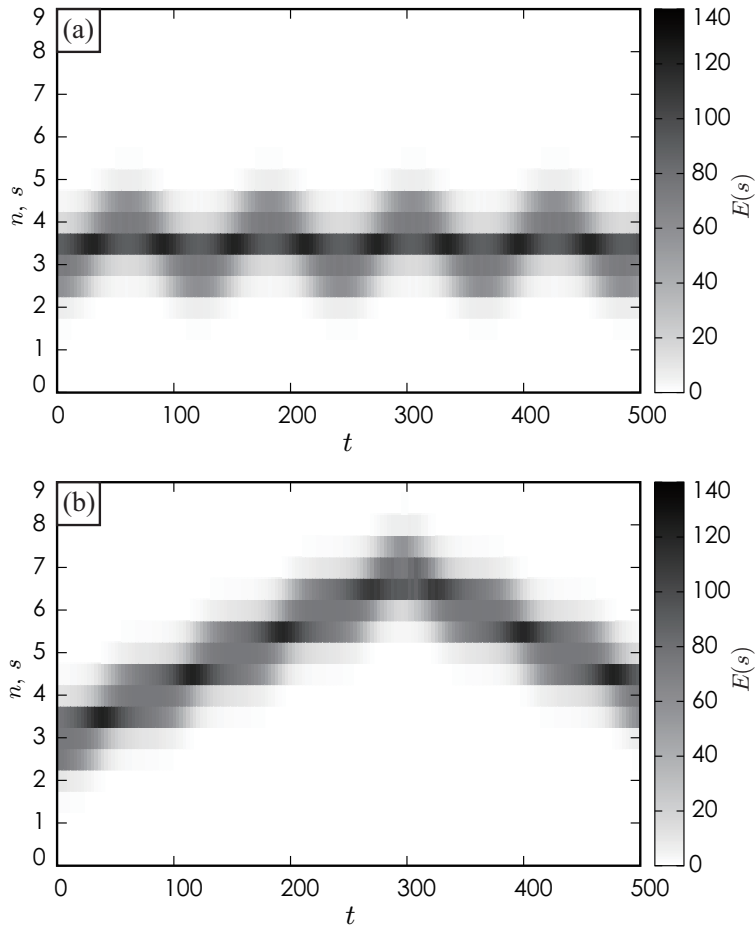
Figure 4.12: Time-development of energy concentration of traveling ILMs. (a) Reciprocally traveling ILM generated at IP1 in Fig. 4.11. (b) Traveling ILM initially started at IP2.

a negative α_{d} can globally change the phase structure. An unstable ILM at the negative impurity has an unstable manifold which surrounds all coexisting ILMs and their manifolds.

On the other hand, the behaviors of traveling ILMs were considered. As results, it was suggested that the global phase structure governs the behavior. In addition, it was shown that unstable manifolds can be thought as separatrices when the global phase structure shows a quite simple structure which is similar to a pendulum system. Behaviors of two traveling ILMs are completely separated by the unstable manifolds. Therefore, it seems that a traveling ILM can be controlled if the structure of unstable manifolds is changed as desired. In the next chapter, ma-

nipulation methods for traveling ILMs will be proposed based on the facts mentioned above.

Appendix to Drastic Change of Global Phase Structure

The global phase structure drastically changes between $\beta_2 = 0.005$ and 0.006 as shown in Fig. 4.5. Although the stability of coexisting ILMs are flipped in $0.005 < \beta_2 < 0.006$, the drastic change and the stability change are not caused simultaneously. Fig. 4.13 shows the process of the drastic change. The parameter setting is set as the same as Fig. 3.9. In the figure, stable ST- and P-modes are represented by open circles. Filled boxes indicate unstable ILMs. At $\beta_2 = 0.005453360$, the unstable manifold of ST4, $W^u(\text{ST4})$ is surrounded by $W^u(\text{P4-5})$ as shown in Fig. 4.13(a). However, the configuration is changed by increasing β_2. The right branch of $W^u(\text{ST4})$ surrounds $W^u(\text{P4-5})$ at $\beta_2 = 0.005453372$. On the other hand, the right branch of $W^u(\text{P3-4})$ encloses $W^u(\text{ST4})$ and $W^u(\text{P4-5})$ for both Figs. 4.13(a) and (b). The drastic change for $W^u(\text{P3-4})$ occurs in another parameter region, $0.005453372 < \beta_2 < 0.005453380$. Fig. 4.13(c) shows that $W^u(\text{P3-4})$ is surrounded by the left branch of $W^u(\text{ST4})$. Unstable manifolds of P3-4 and P4-5 are finally vanished when P3-4(u) and P4-5(u) disappear with neighboring stable ST-modes. Consequently, the global phase structure is changed as shown in Fig. 4.5(c) when β_2 increases to 0.006.
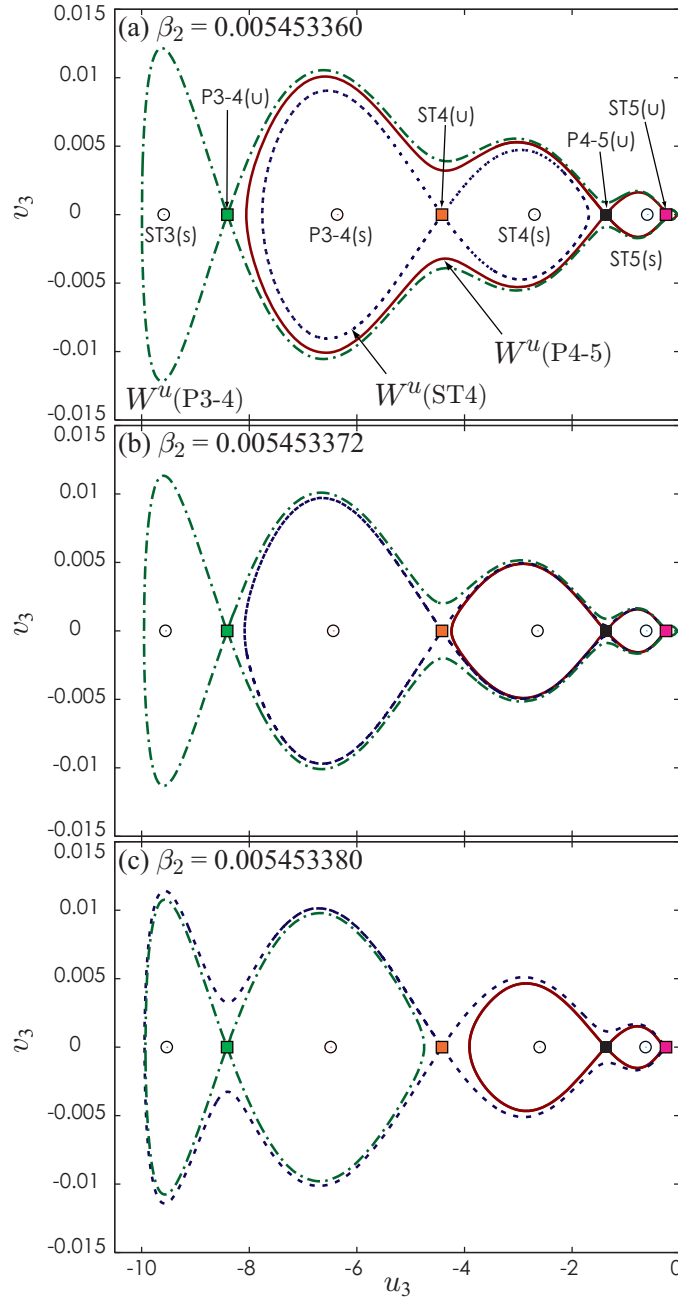
Figure 4.13: Drastic change of invariant manifolds of unstable ILMs. The solid, dotted, dashed-dotted curve represent W^u(P4-5), W^u(ST4), and W^u(P3-4), respectively. Parameters are set at $\alpha_1 = 1$, $\alpha_2 = 0.1$, $\beta_1 = 0.01$, and $\mathcal{H} = 250$. Boundaries of the array are fixed. The corresponding bifurcation diagram is shown in Fig. 3.9.

Chapter 5

Manipulation of ILM

This chapter presents new methods for manipulation of intrinsic localized modes in coupled cantilever arrays. In the previous chapter, it was shown that the global phase structure is changed when the stability change occurs. In addition, an impurity in the array possibly affects the global phase structure. It was also cleared that traveling intrinsic localized modes are governed by the global phase structure. In this chapter, two manipulation methods are proposed for ILM based on the phase structure. One is based on the drastic change of the phase structure according to the change of stability. The nonlinear inter-site coefficient is abruptly varied, then an ILM begins to move from a site to another. Another is achieved by adding an impurity. The impurity is confirmed to attract or repulse an ILM. Dynamical behaviors of manipulated ILMs are discussed based on the global change of phase structures by these methods.

5.1   Capture and Release

5.1.1   Stability Change for Manipulation of ILM

In the previous chapter, it was suggested that the behavior of traveling ILMs are governed by the structure of unstable manifolds of unstable ILMs. In addition, the drastic change of the global phase structure was observed with respect to the nonlinear inter-site coefficient β_2. These facts allow us to expect that the behavior of traveling ILM can be manipulated by adjusting β_2. Fig. 5.1 depicts a concept to manipulate ILMs by changing the global phase structure. Here, it is assumed that a traveling ILM is initially excited near a stable ILM. Then the traveling ILM stays around the stable ILM as shown in Fig. 5.1(a). When β_2 is rapidly varied, the stability of coexisting ILMs changes and the drastic change of the global phase
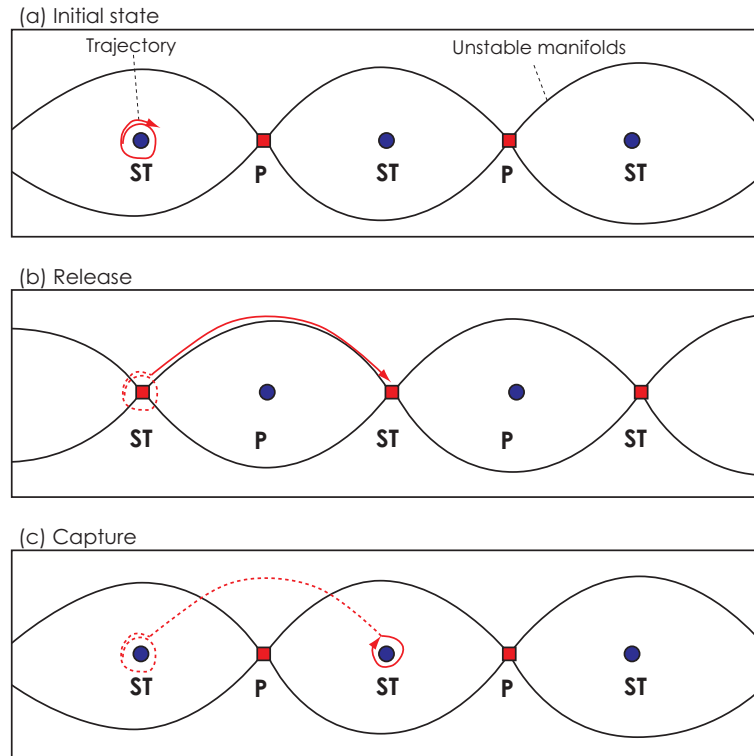
Figure 5.1: Concept of ILM manipulation using stability change. Squares and circles correspond to unstable and stable ILMs, respectively. Solid curves indicate unstable manifolds of unstable ILMs. The arrow represents the trajectory of the traveling ILM.

structure appears. As a result, the traveling ILM begins to move along an unstable manifold of the destabilized ILM (Fig. 5.1(b)). That is to say, the traveling ILM is *released*. The released ILM will wander in the array. The wandering ILM will be *captured* by the secondary stability change of ILMs, when the wandering ILM approaches to the vicinity of an unstable ILM. The captured ILM stays around the stabilized ILM at a site as shown in Fig. 5.1(c). As results, the traveling ILM is shifted from a site to the next.

5.1.2 Numerical Confirmation

Figure 5.2 shows the structure of unstable manifolds at $\beta_2 = 0.005$ and 0.006. Stable and unstable ILMs alternately exist. Stability of ILMs is flipped when β_2 is increased from 0.005 to 0.006. In Fig. 5.2(a), unstable manifolds connect between vicinities of unstable P-modes and surround stable ST-modes. After the stability change of
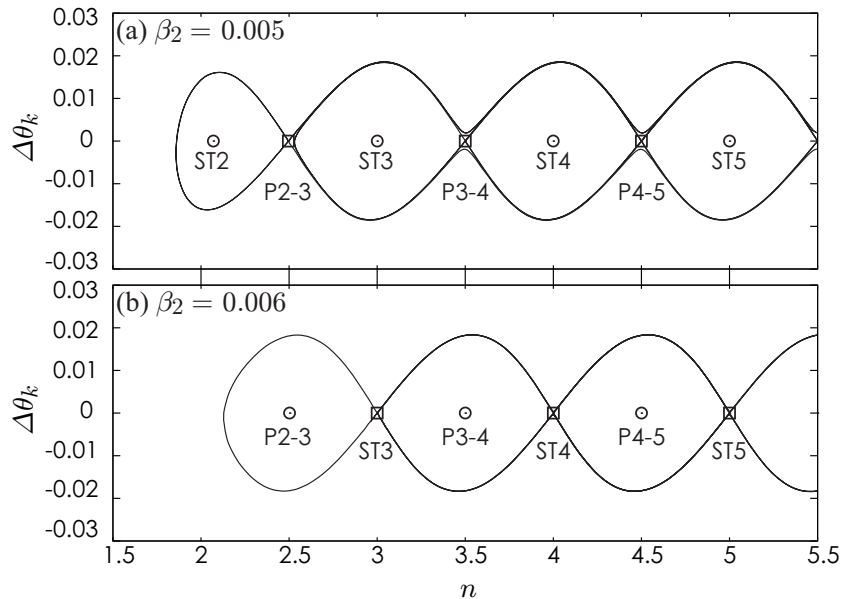
Figure 5.2: Coexisting ILMs and unstable manifolds at (a)$\beta_2 = 0.005$, (b)$\beta_2 = 0.006$. Circles and boxes indicate stable and unstable ILMs, respectively. Solid curves represent unstable manifolds.

ILMs, the structure of phase space drastically changes with relation to unstable manifolds. Stable P-modes are surrounded by unstable manifolds which connect vicinities of each unstable ST-modes.

A numerical simulation is shown for the capture and release manipulation as in Fig. 5.3. Here, an initial condition is set as stable ST3 at $\beta_2 = 0.005$. The magnitude of energy is shown by the tone in Fig. 5.3. The locus of the energy concentration initially exists at $n = 3$. The first stability change at $t = 100$ is due to the discontinuous change of β_2. Then the global phase structure changes from Fig. 5.2(a) to (b). ST3 loses its stability and begins to travel toward $n = 4$ for $100 < t < 820$. That is, ST3 is released. The nonlinear inter-site coefficient β_2 is changed to 0.005 again at $t = 820$. Then the traveling ILM is captured around $n = 4$. Consequently, the ILM is manipulated from the site at $n = 3$ to 4.

5.1.3 Success and Failure of Capture

The capture and release of traveling ILMs were numerically shown in the previous section. It was confirmed that the released ILM can be captured and stayed around a site. However, the captured ILM does not converge to the site. A small fluctuation
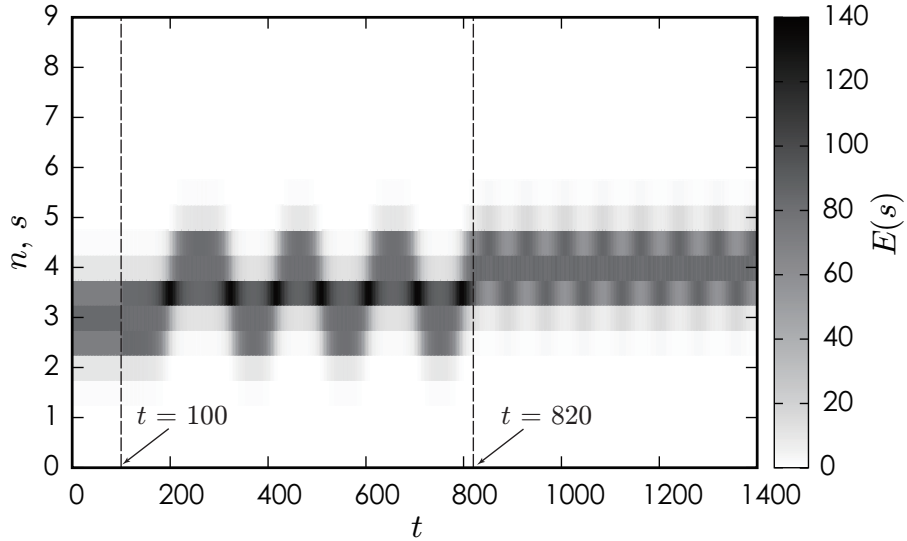
Figure 5.3: Capture and release of a traveling ILM. Darkness is proportional to the magnitude of energy. Dashed-lines indicate when the stability change is caused.

around the site remains. In this section, the reason of the fluctuation is discussed.

The capture and release manipulations of P3-4 are shown in Fig. 5.4 for different onset of the stability change of ILMs. The horizontal axis corresponds to the iteration number of the Poincaré map $\mathcal{P}$. In these cases, the stability changes are fired when the orbit of traveling ILM intersects Σ_4. It allows to discuss the position of the traveling ILM in $(\theta_k, \ \Delta\theta_k)$ plane when the stability change occurs.

At first, it is shown that the captured ILM shows very small fluctuation. In Fig. 5.4(a), the traveling ILM initially stands at P3-4. In the initial state, the nonlinear inter-site coefficient is set at $\beta_2 = 0.006$. Thus, P3-4 is stable. The nonlinear inter-site coefficient is discontinuously varied from 0.006 to 0.005 at $k = 69$, where k denotes the map number corresponding to time evolution. As a result, the first stability change occurs and the ILM is released. The released ILM leaves from the destabilized P3-4 at $k \simeq 110$. Then it moves toward the vicinity of P4-5, because the unstable manifold of P3-4 reaches near the P4-5 (see Fig. 4.5(b)). After the released ILM reaches the vicinity of P4-5, β_2 is set at 0.006 again at $k = 134$ for stabilizing P4-5 (secondary change). The released ILM is captured around the stabilized P4-5. Consequently, the ILM travels from P3-4 to P4-5.

However, the released ILM is not captured when the second stability change is fired at $k = 118$ as shown in Fig. 5.4(b). The ILM travels back and forth in the whole of array. On the other hand, Fig. 5.4(c) shows that the released ILM is
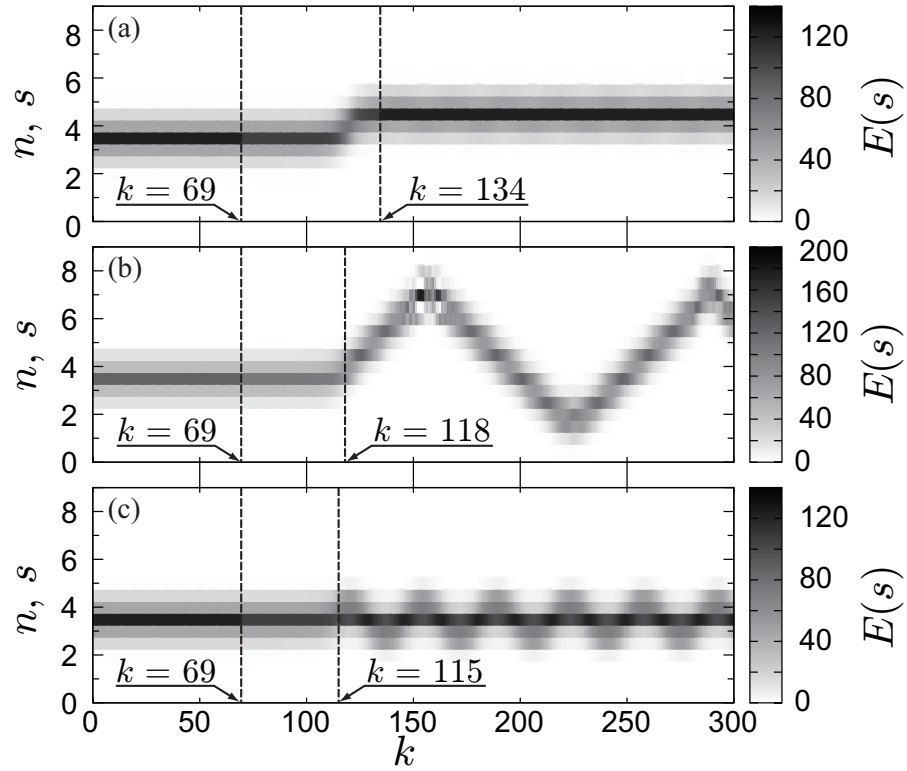
Figure 5.4: Capture and release of traveling ILM. A stable ILM is initially excited. The stability of coexisting ILMs is changed at $k = 69$, where k depicts the number of the map and corresponds to the time development. The nonlinear inter-site coefficient is instantaneously changed here. The stability is flipped again at $k = 134(a)$, $118(b)$, and $115(c)$.
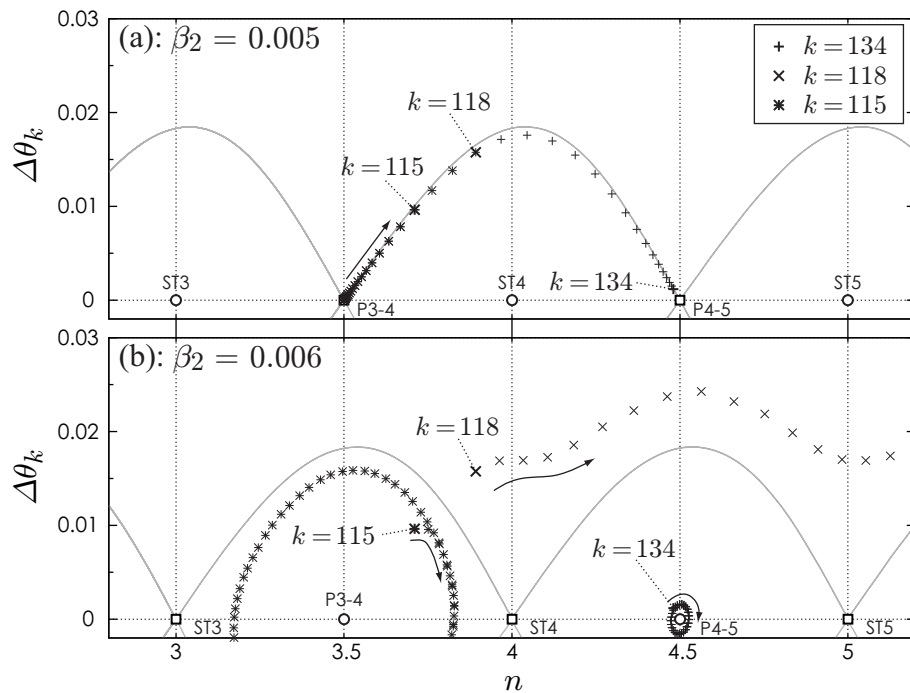
Figure 5.5: Trajectories of traveling ILMs and unstable manifolds of unstable ILMs. The trajectories are projected by $\mathcal{G}$. Open circles and boxes correspond to coexisting ILMs. Gray curves represent unstable manifolds of unstable ILMs. The trajectories are drawn by sequences of points. (a) Trajectories during the first and the second stability changes, and (b) trajectories after the second stability change.

captured around the ILM where the traveling ILM initially stands, when the second stability change is fired at $k = 115$. The traveling ILM reciprocally moves around P3-4.

The difference in the behaviors can be explained by the global phase structures. In Fig. 5.5, the trajectories of manipulated ILMs and unstable manifolds of unstable ILMs are shown. A released ILM travels along unstable manifolds from unstable P3-4 as shown in Fig. 5.5(a). After the second stability change, the phase structure is drastically changed. Fig. 5.5(b) shows the phase structure and trajectories of traveling ILMs after the second stability change. For the trajectory corresponding to Fig. 5.4(b), the traveling ILM is located outside all cyclic structures of unstable manifolds. On the other hand, the traveling ILM is inside the cyclic structure for the trajectory of Fig. 5.4(a) and 5.4(c). It implies that if a traveling ILM, released by the first stability change, is inside the cyclic structure at the second stability change, the traveling ILM is captured around a stabilized ILM. In addition, fluctuations of captured ILMs depend on the position when the secondary stability change occurs. If the secondary stability change occurs when the trajectory of traveling ILM is sufficiently close to an unstable ILM, the fluctuation of the captured ILM is small. On the other hand, a traveling ILM which wanders the whole of array is generated if the traveling ILM is located outside all cyclic structures. The position, when the secondary stability change occurs, determines the behavior of traveling ILM after the capture and release manipulation.

5.2   Attraction and Repulsion

5.2.1   Motivation

An experimental manipulation of ILM was first achieved by adding impurities [35]. An ILM was attracted and repulsed by the impurities. The experimental results suggest that the global phase structure can be changed locally by adding an impurity. In Chap. 3 and 4, the influence of an impurity was discussed. As a result, it was shown that the impurity can change the global phase structure if β_2 is close to the critical value for the stability change. In this section, manipulations using an impurity are discussed numerically. Here, small variation of linear on-site coefficient is assumed as an impurity of the array.

5.2.2   Global Phase Structure with Impurity

In this section, manipulations will be shown in the coupled cantilever array with fixed boundaries. Fig. 5.6(a) shows the initial phase structure before an impurity is added. The nonlinear inter-site coefficient β_2 is set at 0.005. ST1 and P1-2 do not exist because of the fixed boundaries. Here we consider the case that ST3 is manipulated by adding an impurity at $n = 4$. The global phase structure is locally changed when the linear on-site coefficient α_1 of the 4th cantilever is varied from 1 to $1 + \alpha_d$. At $\alpha_d = 0.05$, the global phase structure is changed as shown in Fig. 5.6(b). Coexisting ILMs neighboring ST4 are disappeared. Unstable manifolds surrounding ST4 form a larger loop than the initial phase structure in Fig. 5.6(b). In this case, the stability of ST4 is not flipped. However, ST4 loses its stability when α_d is set at -0.05. In Fig. 5.6(c), the destabilized ST4 has one dimensional unstable manifold as well as coexisting P-modes. The unstable manifolds of ST4 surround all coexisting ILMs except ST4. For instance, P2-3 and its unstable manifold are surrounded by the left branch of unstable manifold of the destabilized ST4. Figs. 5.6(b) and (c) show that an impurity, added at a certain site, can locally affect coexisting ILMs and can change the structure of unstable manifold.

5.2.3   Attractive and Repulsive Manipulation

Attractive and repulsive manipulations are shown with energy distributions in Fig. 5.7. The stable ST3 is initially excited. An attractive manipulation of ST3 is achieved by adding a positive impurity $\alpha_d = 0.05$ at $n = 4$. Fig. 5.7(a) shows the behavior of the attracted ST3. The impurity is added at $t = 0$. ST3 is first attracted by the impurity. Then the attracted ILM reciprocally moves around $n = 4$. The corresponding trajectory is shown by filled boxes in Fig. 5.6(b). The stable ST3 at $\alpha_d = 0$ is vanished by the impurity. Thus, the initially excited ST3 begins to move. The arrow in Fig. 5.6(b) indicates the direction of the trajectory. The trajectory first moves to the right hand side and revolves around ST4.

On the other hand, Fig. 5.7(b) shows a repulsive manipulation. The initially excited ST3 is first repulsed by an impurity $\alpha_d = -0.05$. The repulsed ST3 wanders between $n = 1.5$ and 3. That is, ST3 is repulsively manipulated. The trajectory of the repulsed ST3 is shown in Fig. 5.6(c). In this case, the stable ST3 still exists when the impurity is added. However, the stable ST3 approaches to the unstable P2-3. In addition, the right branch of $W^u(\text{P2-3})$ is located in $n < 3$ as shown in Fig. 5.6(c). Therefore, the initial point which corresponds to ST3 in Fig. 5.6(a) is located outside $W^u(\text{P2-3})$ at $t = 0$. Then, the trajectory first moves along the arrow shown in Fig. 5.6(c). The trajectory turns along the unstable manifold of P2-3.
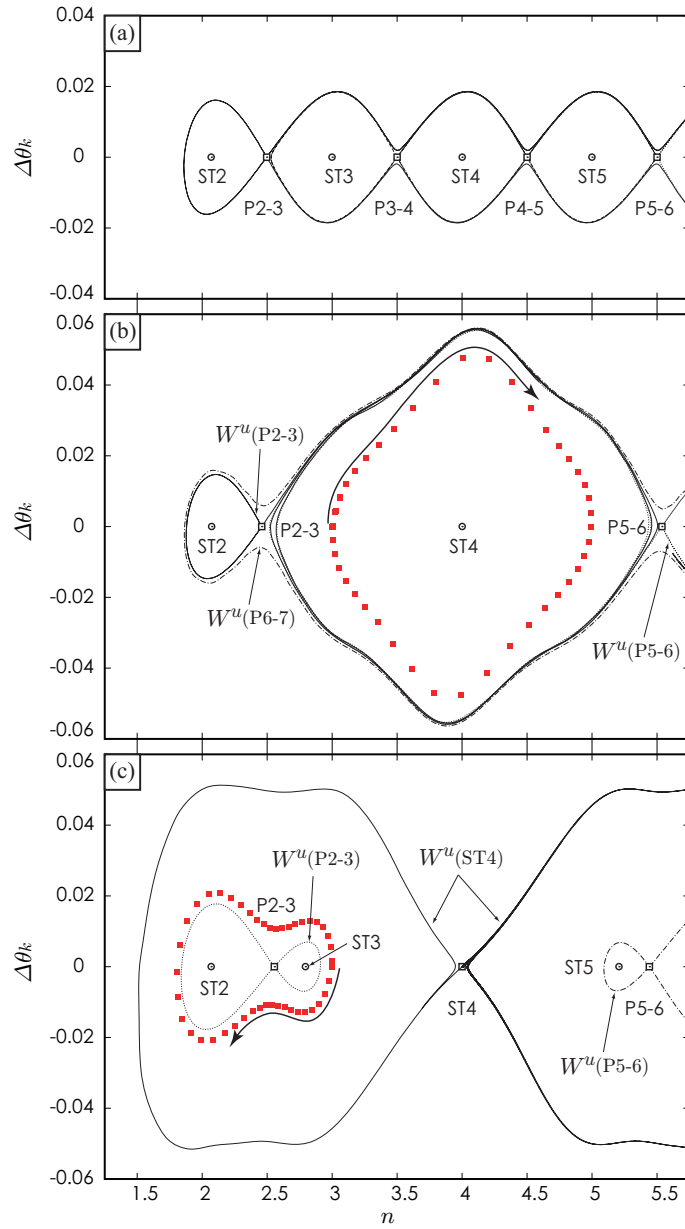
Figure 5.6: Coexisting ILMs and unstable manifolds for the case of an impurity, α_d is added at $n = 4$. (a) $\alpha_d = 0$, (b) $\alpha_d = 0.05$, (c) $\alpha_d = -0.05$. Filled circles represent trajectories of (a) attracted and (b) repulsed ST3.

65

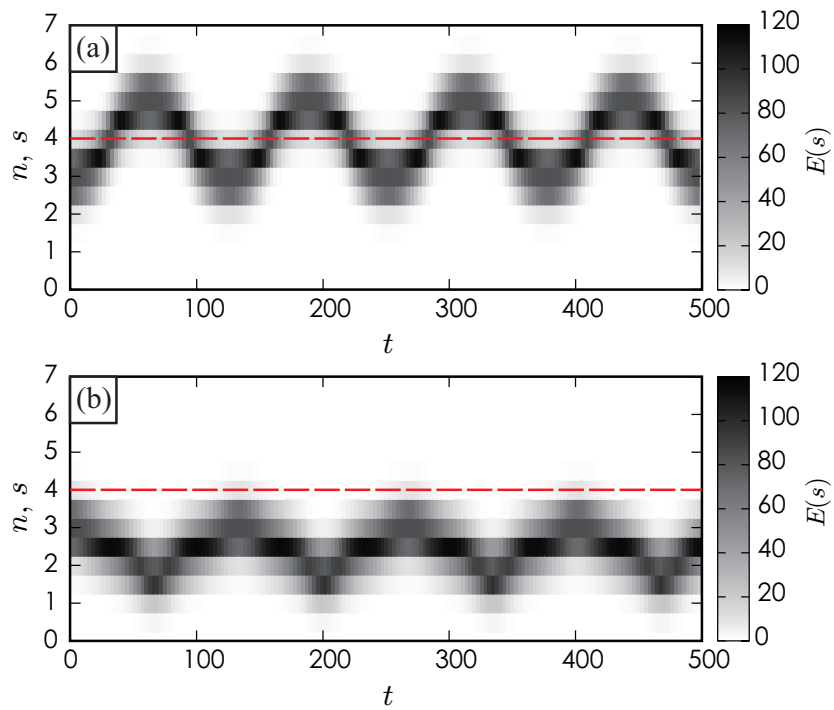Figure 5.7: Manipulation using an impurity. (a) Attractive and (b) repulsive manipulation. An impurity is added at $n = 4$.

5.3 Remarks

In this chapter, manipulations for a traveling ILM in Eq. (2.2) were numerically discussed based on the global phase structure. In the capture and release manipulation, an ILM was arbitrary released and was captured around a site. The abrupt change of the nonlinear inter-site coefficient was applied to achieve the drastic change of global phase structure due to stability change. In the attractive and repulsive manipulations, an ILM was attracted or repulsed by an impurity added at a site. The mechanism of the manipulations was also explained based on the global phase structure.

The capture and release manipulation using the stability change requires that the nonlinear inter-site coefficient β_2 of Eq. (2.2) is adjustable. The nonlinear inter-site coefficient seems difficult to adjust experimentally. However, the nonlinear on-site coefficient β_1 can also flip the stability because the ratio β_2/β_1 determines the stability of coexisting ILMs. It has already been reported that an on-site nonlinearity can be adjustable by applying a static electric field to a micro-cantilever array [36]. When the electric field is applied between each cantilever and a substrate facing the array, the electric force is induced in each cantilever. The on-site potential is modified as $U_{\mathrm{O}n}(u_n) = \alpha_1 u_n^2/2 + \beta_1 u_n^4/4 - \delta_1 V^2/(d_0' + u_n)$ [36, 59], where d_0' and V depict a nondimensionalized distance and the voltage between the cantilever array and the substrate, respectively. Relative magnitude of the static electric potential is determined by a coefficient δ_1, which depends on the size of cantilever. According to Maclaurin's expansion, the applied electric field changes the on-site nonlinear coefficient as $\beta_1' = \beta_1 - 4\delta_1 V^2/d_0'^5$. Therefore the on-site nonlinearity can be varied as a function of the voltage. If a micro-cantilever array is fabricated to have the stable ST-modes, the manipulation is possible because an applied voltage decreases the nonlinear on-site coefficient.

In the next chapter, a macro-mechanical cantilever array having tunable on-site potentials is proposed. An experimentally excited ILM will be manipulated by a locally induced impurity. The mechanism of the experimental manipulation is discussed and compared with the manipulations proposed in this chapter.

Chapter 6

Experimental manipulation in macro-mechanical system

This chapter presents experimental discussion on intrinsic localized modes. A macro-mechanical cantilever array is first proposed as a coupled cantilever array. Each cantilever in the array is designed so that the on-site potential can be adjusted. Therefore, the cantilever array allows that attractive and repulsive manipulations using an impurity are investigated experimentally. In this chapter, observations of intrinsic localized modes are shown prior to manipulation. Numerical simulations are applied to confirm the experimental results. The stability of ILM in the array is also investigated numerically. Finally, an attractive manipulation is shown experimentally.

6.1   Macro-mechanical Cantilever Array

6.1.1   Cantilever with Cylindrical Mass

In this section, an equation of motion of a macro-cantilever is derived. Figs. 6.1 and 6.2 show a schematic configuration of the cantilever. A cylindrical mass is attached at the free end of cantilever. Vibration of the cantilever is described by Euler-Bernoulli beam theory as follows:

$$\rho w h \frac{\partial^2 y}{\partial t^2} = - EI \frac{\partial^4 y}{\partial x^4},\tag{6.1}$$

where y depicts the displacement of cantilever at x. Moment of inertia is represented by $I = wh^3/12$. To solve Eq. (6.1), a solution is assumed to be $y(x,t) = Y(x)\sin(\omega t)$.

Then an ordinary differential equation

$$\frac{\mathrm{d}^4 Y}{\mathrm{d}x^4} = -\frac{\rho wh}{EI}\omega^2 Y,$$

(6.2)

is obtained. Eq. (6.2) can easily be solved. The general solution with four arbitrary constants is as follows:

$$Y(x) = C_1 \sin\left(\frac{\lambda}{\ell}x\right) + C_2 \cos\left(\frac{\lambda}{\ell}x\right) + C_3 \sinh\left(\frac{\lambda}{\ell}x\right) + C_4 \cosh\left(\frac{\lambda}{\ell}x\right),$$

(6.3)

where λ is a nondimensional parameter defined as $\lambda = \ell\sqrt{\omega\sqrt{\rho wh/EI}}$. Boundary conditions for the cantilever are given as follows:

$$\begin{cases} Y(0) = 0 \\ Y'(0) = 0 \end{cases} \quad \text{for fixed end,}$$

$$\begin{cases} EIY'''(\ell) + m\omega^2 Y(\ell) = 0 \\ -EIY''(\ell) + J\omega^2 Y'(\ell) = 0 \end{cases} \quad \text{for free end,}$$

(6.4)

where m and J denote the mass and the moment of the cylindrical mass, respectively. The boundary conditions give $C_1 = -C_3$, $C_2 = -C_4$ and a condition

$$(1 + \cos\lambda\cosh\lambda) - \frac{\lambda^3}{\ell^3}\frac{J}{\rho A}(\sin\lambda\cosh\lambda + \cos\lambda\sinh\lambda)$$

$$- \frac{\lambda}{\ell}\frac{M}{\rho A}(\sin\lambda\cosh\lambda - \cos\lambda\sinh\lambda) + \frac{MJ}{\rho^2 A^2}\frac{\lambda^4}{\ell^4}(1 - \cos\lambda\cosh\lambda) = 0,$$

(6.5)

which determines the frequency of vibrating cantilever. The lowest value of λ satisfying Eq. (6.5) is obtained as about $1.64(= \lambda_1)$[1]. The shape function $Y(x)$ shows that the end of cantilever oscillates with the largest amplitude. This oscillation is called the first mode oscillation of cantilever. In this thesis, the first mode is only focused so that the partial differential equation is reduced to an ordinary differential equation.

When the cantilever oscillates with the first mode frequency ω_0, the displacement of the end of cantilever shows a simple harmonic oscillation $y(\ell, t) = Y(\ell)\sin(\omega_0 t)$. Since a linear spring-mass system has harmonic solutions, the motion of the end of cantilever is described by a simple equation as follows:

$$\ddot{u} = -\omega_0^2 u,$$

(6.6)

where u denotes the displacement of the tip of cantilever. Eq. (6.6) represents a linear oscillation of the tip of cantilever for a small amplitude.

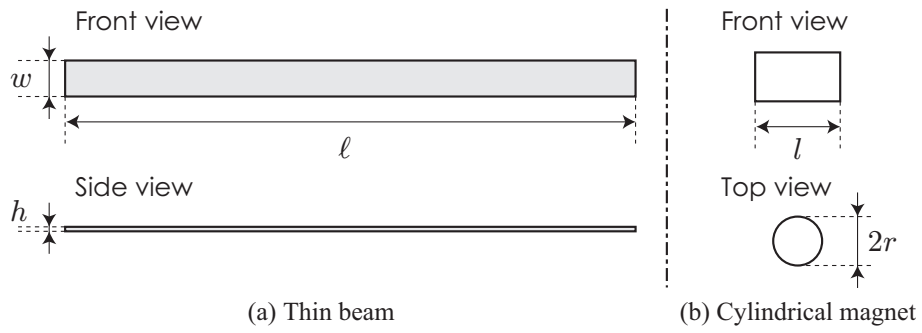[1] The corresponding frequency is about 37.5 Hz.

70

Front view

w

ℓ

Side view

h

Front view

l

Top view

$2r$

(a) Thin beam

(b) Cylindrical magnet

Figure 6.1: Schematic image of (a) thin beam and (b) cylindrical magnet.

$y(x)$

$x = 0$

$x = \ell$

O

x

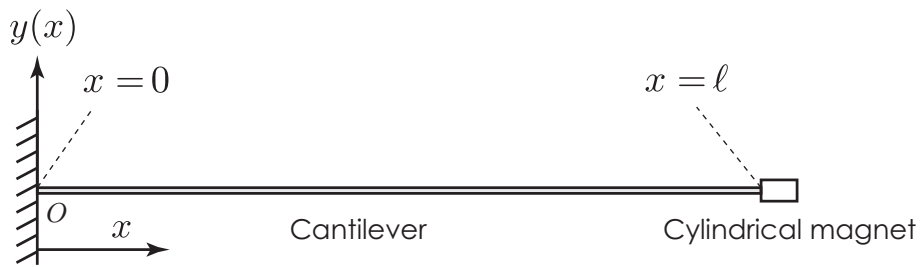Cantilever

Cylindrical magnet

Figure 6.2: Configuration of cantilever with permanent magnet.

6.1.2 Nonlinearity Caused by Magnetic Interaction

Intrinsic localized modes in a coupled cantilever array need nonlinearities in the array in order to exist. Then, a macro-cantilever is designed to have a nonlinearity in its restoring force. A static magnetic force is often employed to induce the nonlinearity [40–42,60]. In this thesis, a magnetic interaction between a permanent magnet and an electro magnet is applied. A schematic configuration is shown in Fig. 6.3. A permanent magnet (PM) is attached at the tip of cantilever. An electromagnet (EM) is placed beneath PM. The magnetic force between PM and EM can approximately be described by Coulomb's law for magnetic charges. Then the interaction force is nonlinearly changed against the displacement of cantilever. The configuration of magnetic charges is shown in Fig. 6.3(c). If the displacement of cantilever is sufficiently small relative to the length of cantilever, Coulomb's law for magnetic charges gives the restoring force

$$
\begin{aligned}
F(u_n) =& \frac{m_{\mathrm{p}} m_{\mathrm{e}}}{4\pi\mu_0} \frac{u_n}{\left(u_0^2 + d_0^2\right)^{\frac{3}{2}}}, \\
=& \chi(I_{\mathrm{EM}}) \frac{u_n}{\left(u_0^2 + d_0^2\right)^{\frac{3}{2}}},
\end{aligned}
\tag{6.7}
$$

where m_{p} and m_{e} correspond to magnetic charges of PM and EM, respectively. The distance between PM and EM at the equilibrium state is denoted by d_0. The magnetic permeability is represented by μ_0. Because the magnitude of m_{e} depends on the current flowing EM, the coefficient of the interaction can be represented as a function of the current, $\chi(I_{\mathrm{EM}})$. In this thesis, we assumed the linear relationship $\chi(I_{\mathrm{EM}}) = \chi_0 + \chi_1 I_{\mathrm{EM}}$. Because EM has a ferromagnetic core, an attractive force between PM and EM is caused even if the current is kept to be zero. Thus χ_0 is always negative. On the other hand, the current direction changes the sign of $\chi_1 I_{\mathrm{EM}}$. We chose the current enhancing the attractive force is positive. Therefore, χ_1 is also negative.

A voice coil motor is attached to excite the cantilever as shown in Fig. 6.3. When the voice coil motor is driven by a sinusoidal signal, the motion of the cantilever is depicted by

$$
\ddot{u} = -\omega_0^2 u - \gamma \dot{u} + F(u) + A\cos(\omega t),
\tag{6.8}
$$

where A and ω denote the magnitude and the angular frequency of the external force excited by the voice coil motor, respectively. The damping coefficient γ is due to the air resistance.

Voice coil motor $A\cos\omega t$

Cantilever

u_n

Permanent magnet

Electromagnet

d_0

u_n

m_{p}

m_{e}
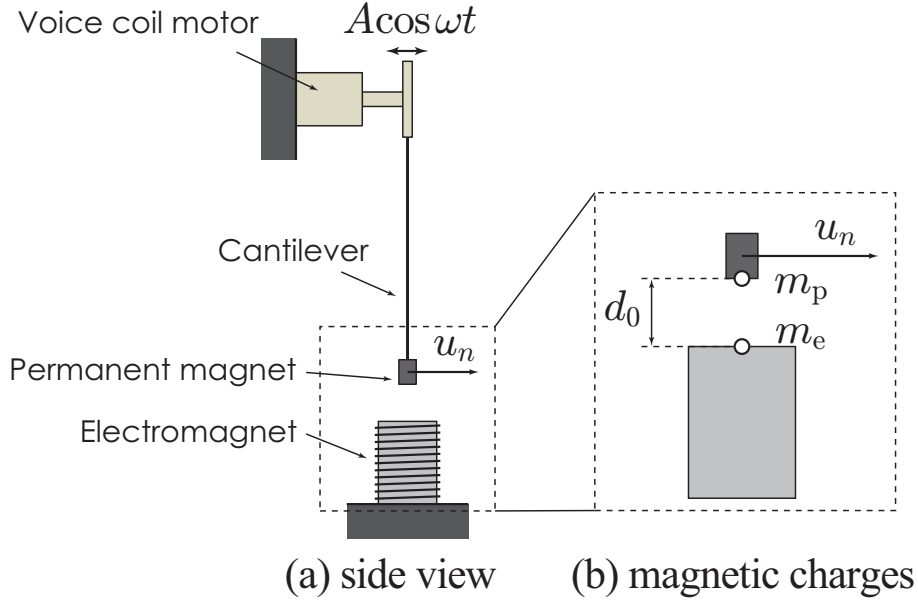
(a) side view   (b) magnetic charges

Figure 6.3: (a) Side view of a cantilever. A permanent magnet is attached at the free end of the cantilever. An electromagnet is placed beneath the permanent magnet. (b) Configuration of magnetic charges.

6.1.3   Mechanically Coupled Cantilevers

A schematic configuration of a macro-mechanical cantilever array is shown in Fig. 6.4. Eight cantilevers are placed with an equal interval in one dimension. Size of the array are in Table 6.1. Each cantilever derived by Eq. (6.8) is mechanically coupled by a elastic rod, which is called coupling rod. The coupling rod causes a force depending on the difference of displacement of adjacent cantilevers. The force linearly changes against the displacement difference if the deformation of the rod is sufficiently small. As shown in Fig. 6.4, the rod is attached near the support. The displacement of cantilever at the rod is quite small relative to the tip. Thus we assume the linearity of the coupling force. Therefore, the equation of motion of the coupled cantilever array is obtained as follows:

$$\begin{cases} \dot{u}_n = v_n, \\ \dot{v}_n = -\omega_0^2 u_n - \gamma u_n + F(u_n) + A\cos(\omega t) \\ \qquad - C(u_n - u_{n+1}) - C(u_n - u_{n-1}), \end{cases} \tag{6.9}$$

Table 6.1: Size of cantilever array

Each cantilever			
Length(ℓ)	70.0 mm	Width(w)	5.0 mm
Thickness(h)	0.3 mm	Pitch(p)	15.0 mm
Density(ρ)	8.0×10^3 kg/m^3	Young's modulus(E)	197 GPa

Cylindrical magnet			
Radius (r)	1.5 mm	Height(l)	3.0 mm
Mass (m)	96.6 mg		

Table 6.2: List of symbols in Eq. (6.9)

Symbol	Value	Symbol	Value
ω_0	$2\pi \times 35.1$ rad/s	γ	1.5 s^{-1}
C	284 s^{-2}	χ_0	-4.71×10^{-5} m^3/s^2
d_0	3.0 mm	χ_1	-9.14×10^{-3} m^3/s^{2}A
A	3.0 m/s^2	ω	$2\pi \times 36.1$ rad/s

where $n = 1, 2, \ldots, 8$ and C denotes the linear inter-site coefficient. The boundary conditions of Eq. (6.9),

$$\begin{cases} u_0 = 0, & v_0 = 0, \\ u_9 = 0, & v_9 = 0, \end{cases} \tag{6.10}$$

are given by the fixed ends of cantilever array shown in Fig. 6.4. Parameters estimated experimentally are in Table 6.2.

6.2 Experimental Setup

The experimental setup is shown in Fig. 6.6. The displacement of each cantilever u_n is measured by using a strain gauge. The resistance of the strain gauge is slightly changed with respect to the displacement of cantilever. To detect the small change of resistance, a bridge circuit is used with a differential amplifier. The amplified voltage signal is stored in a computer through a multi-channel A/D converter.

A current flowing in EM is individually adjusted by the computer. The computer outputs a voltage signal via a multi-channel D/A converter. A V/I converter including a current amplifier supplies the current to EM.
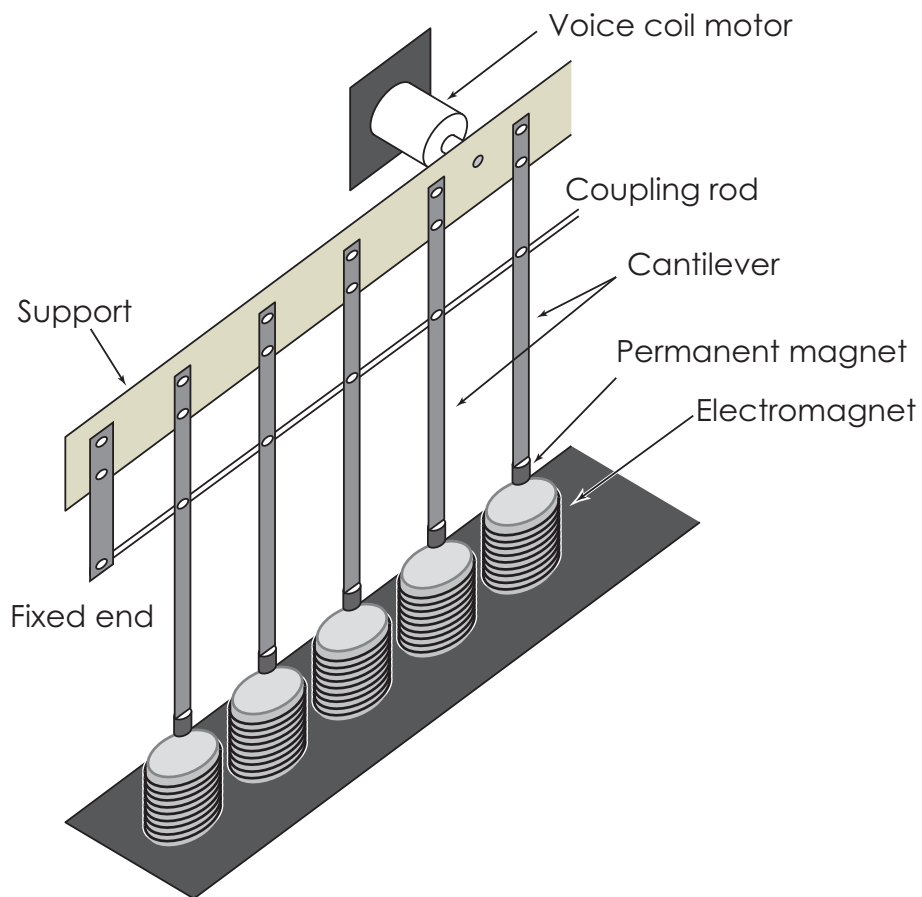
Figure 6.4: Overview of the cantilever array. Eight cantilevers are mechanically coupled by the coupling rod. A short cantilever is attached at the end of array to realize the fixed boundary condition. The voice coil motor excites the whole of cantilever array except electro magnets.
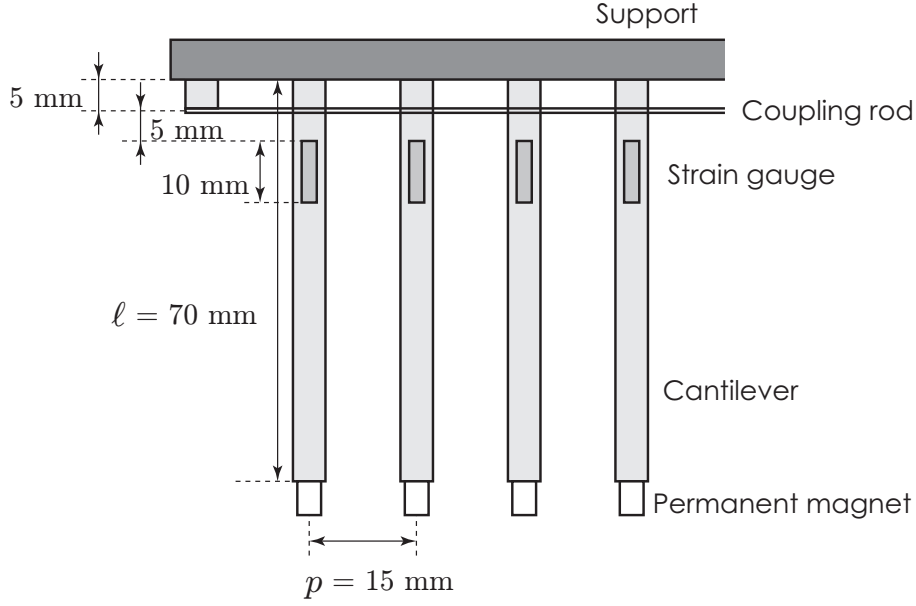
Figure 6.5: Size of the cantilever array.

To excite the cantilever array, the voice coil motor is attached to the support as shown in Fig. 6.6. The voice coil motor is driven by a sinusoidal voltage signal generated by a function generator.

6.3 Observation of Localized Oscillations

6.3.1 Frequency Response of Cantilever

Restoring force of each cantilever nonlinearly varies because of the magnetic interaction between PM and EM. Fig. 6.7 shows the relationship between amplitude and frequency when both γ and A are set at 0. The curvature of the skeleton curves shows the soft-spring characteristics of the cantilever. The curves in Fig. 6.7 asymptotically approach to the line of natural frequency of cantilever as the amplitude increases. Because the contribution of magnetic interaction becomes small when the amplitude is larger than the diameter of EM. On the other hand, the frequency at small amplitude strongly depends on the current flowing EM. The linearization of Eq. (6.9) decides a resonant frequency as follows:

$$\omega_0' = \sqrt{\omega_0^2 - (\chi_0 + \chi_1 I_{\mathrm{EM}})/d_0^3}, \tag{6.11}$$
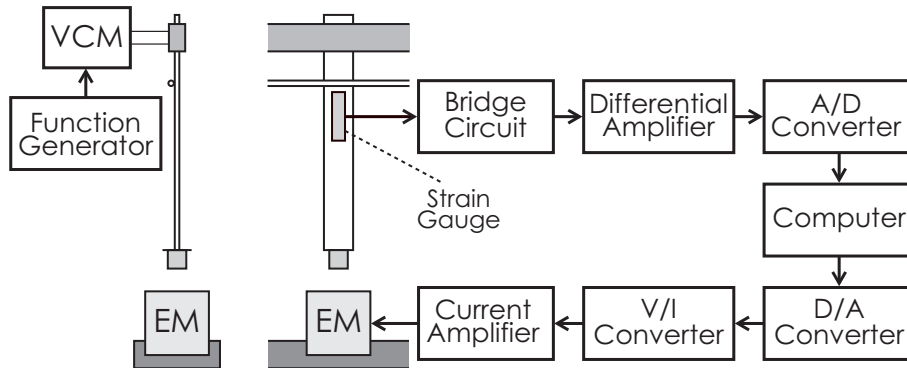
76

Figure 6.6: Experimental setup.

where χ_0 and χ_1 are assumed to be negative. The resonant frequency is shifted to the high frequency side according to the increase of current.

Experimental frequency responses clearly show that a hysteretic response with respect to the external force at the low frequency side from the resonant frequency as shown in Fig. 6.8. Amplitude of a cantilever rapidly increased at 38.3 Hz in the up-scan of frequency. However, in the down-scan, the amplitude jump occurred at 35.9 Hz. Therefore, the cantilever has two stable states when the frequency of external excitor is set between 35.9 Hz and 38.3 Hz. To excite a localized oscillation, the external excitor should vibrate the array with a frequency at which the hysteresis occurs. Then the frequency is set at 36.1 Hz.

6.3.2 Localized Oscillations

Several localized oscillations were observed in the coupled cantilever array by a external excitation. Figs. 6.9(a), (b), and (c) show wave forms of observed localized oscillations. One of the cantilevers has a quite large amplitude while the others are relatively small. The amplitude distribution is obviously localized.

We also observed localized oscillations at $n = 2$ and $n = 4$. However, a localized oscillation standing at $n = 3$ could not be excited. The reason seems a disorder of the array. The disorder is implied by a symmetry of amplitude distribution. As shown in Fig. 6.9(a), amplitude of 6th cantilever is larger than 4th cantilever. Thus the symmetry of observed localized oscillation is slightly broken. The asymmetricity is not observed in numerical simulations shown in Figs. 6.10(a), (b), and (c). The disorder seems to brake the symmetry of localized oscillations because any disorders are not considered in numerical simulations.
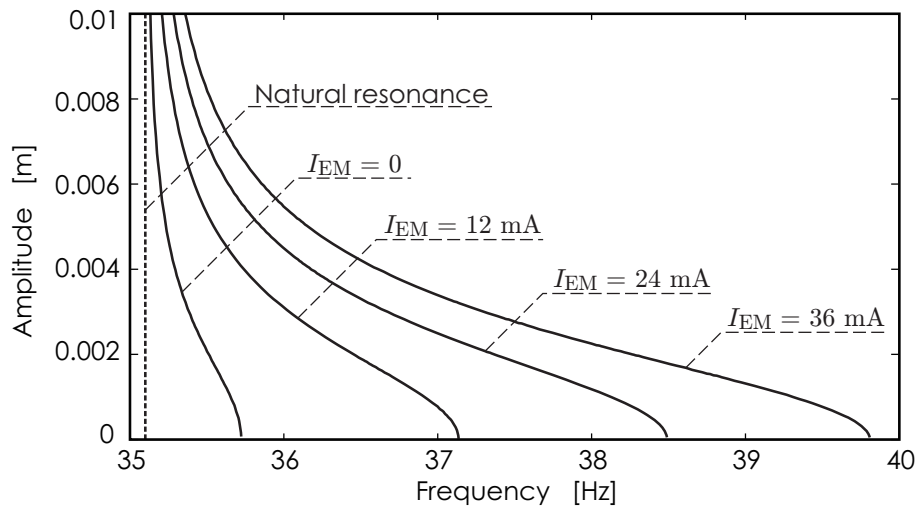
77

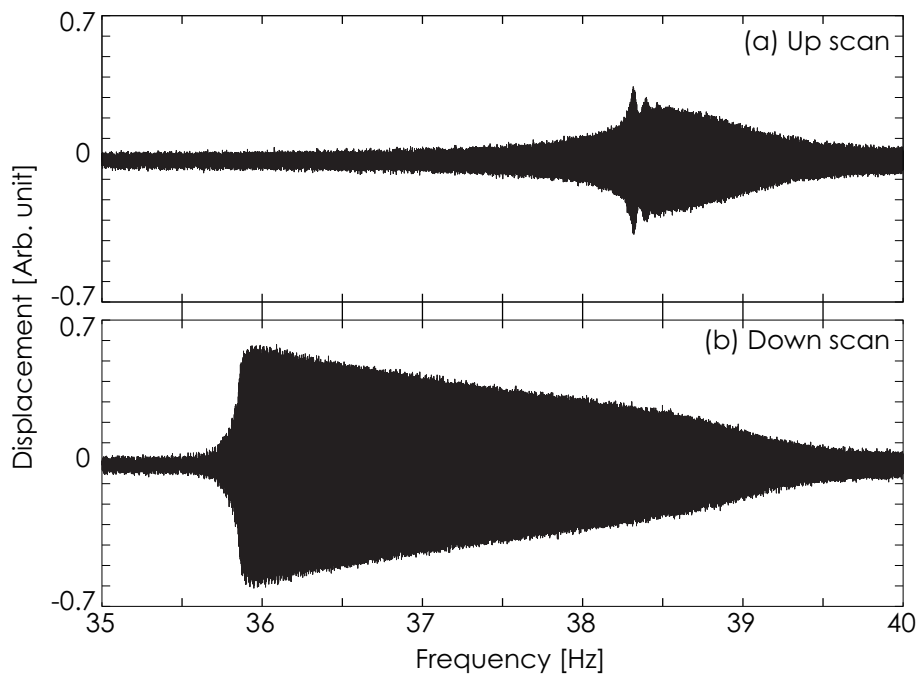Figure 6.7: Skeleton curves. Each curve is obtained numerically.

Figure 6.8: Frequency response for $I_{EM} = 24$ mA. (a) Up scan. (b) Down scan. The scan rate was set at 0.05 Hz/s. The damping and external force are estimated to be $\gamma = 1.5$ s^{-1} and $A = 3.0$ m/s^2, respectively.

(a) ILM at $n = 5$
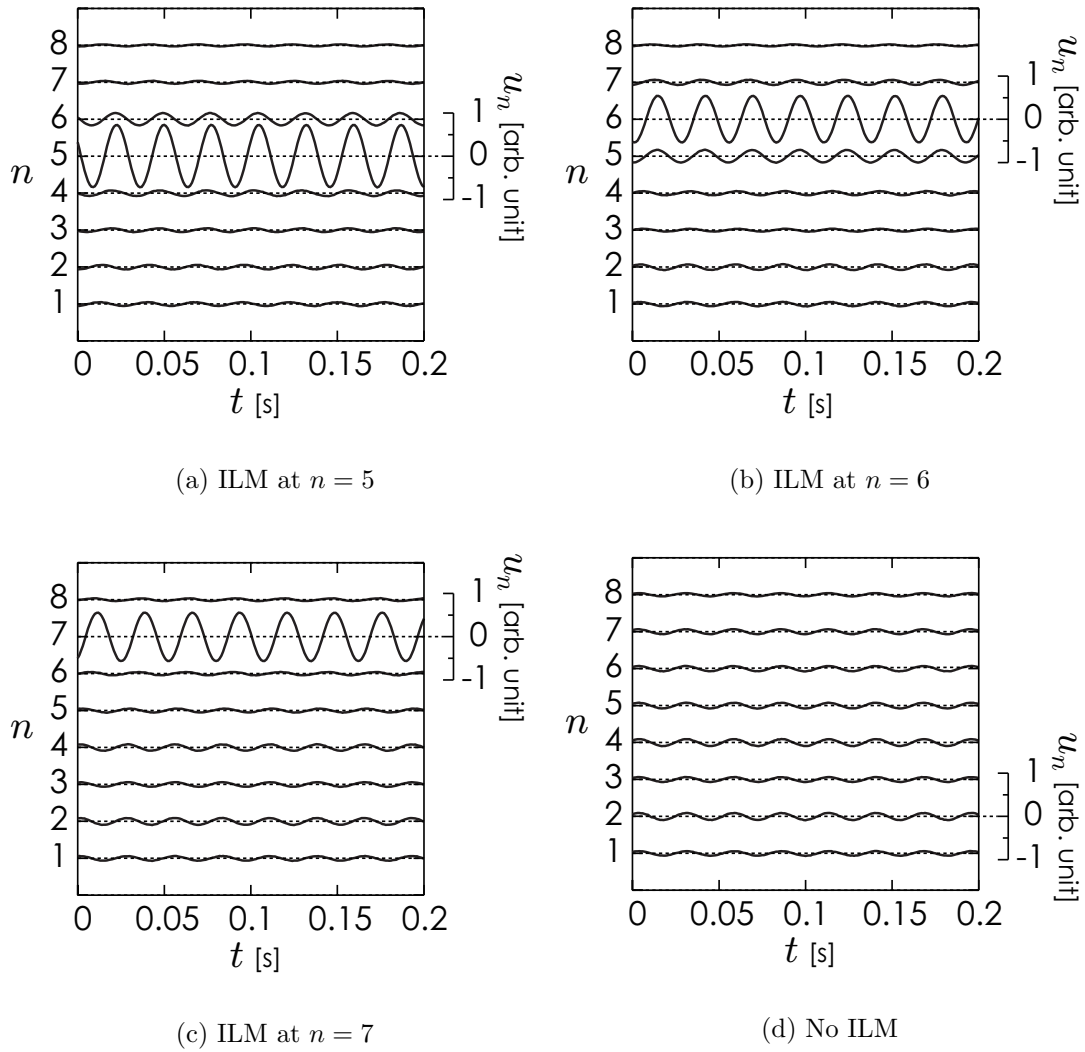
(b) ILM at $n = 6$

(c) ILM at $n = 7$

(d) No ILM

Figure 6.9: Experimentally excited ILMs. An ILM was excited at $n = 5$ (a), $n = 6$ (b), and $n = 7$ (c). It was also observed that there was no ILM (d). The cantilever array was externally vibrated with 36.1 Hz.
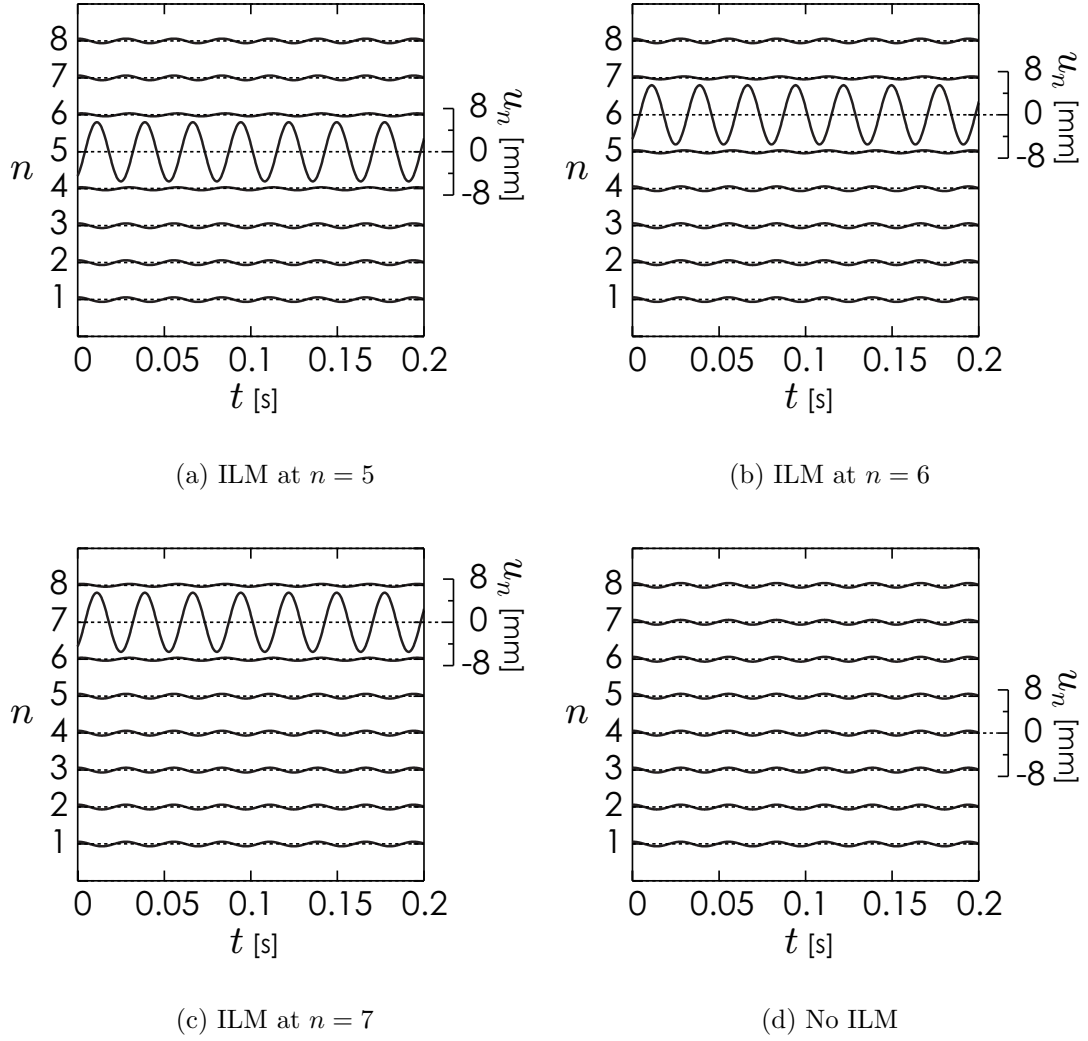
(a) ILM at $n = 5$

(b) ILM at $n = 6$

(c) ILM at $n = 7$

(d) No ILM

Figure 6.10: Numerically obtained ILMs for Eq. (6.9). Parameters are listed in Table 6.2.
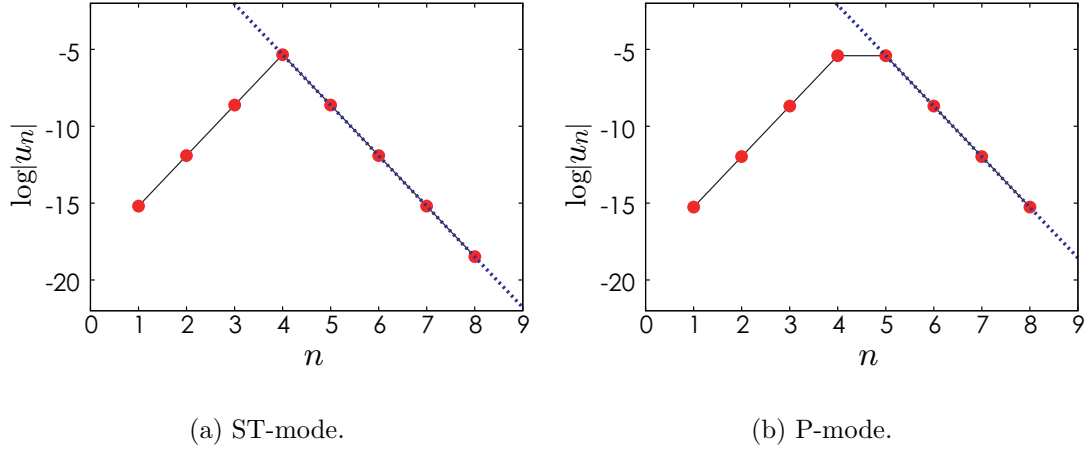
(a) ST-mode.   (b) P-mode.

Figure 6.11: Exponential decay of amplitude of localized oscillations. Theoretical lines drawn by dotted line are given by Eq. (2.12).

The fixed boundaries of the array can be considered as a local impurity. Localized oscillations standing at $n = 1$ and $n = 8$ were not observed experimentally. However, numerical simulations show the localized oscillations. It implies that the fixed boundaries of the array in the experimental system are not completely fixed. A short cantilever which is attached at the end of array is substitute by more stiff one to improve the fixed boundaries.

6.3.3 Intrinsic Localized Modes in Conservative System

Intrinsic localized modes have the tail which exponentially decays. To classify the observed localized oscillations into ILM, it is necessary to confirm whether the oscillations have the exponentially decaying tail. However, the confirmation is difficult in experiments because the cantilever array has the damping and the external force terms. All cantilevers are always excited by the external force. Thus small oscillations are observed even if there is no localized oscillation as shown in Fig. 6.9(d). Then we assume that the observed localized oscillations are classified into ILM if the corresponding solution at the conservative system has the exponentially decaying tail. The solution at the conservative system is obtained by iterating the shooting method. The dumping coefficient γ and the amplitude of external force A are swept with small step. As a result, a sequence of solutions is obtained. Solutions at the end of the sequences are shown in Figs. 6.11(a) and (b). The gradient of the tail is well fitted by the theoretical line given by Eq. (2.12). The solutions in the conser-
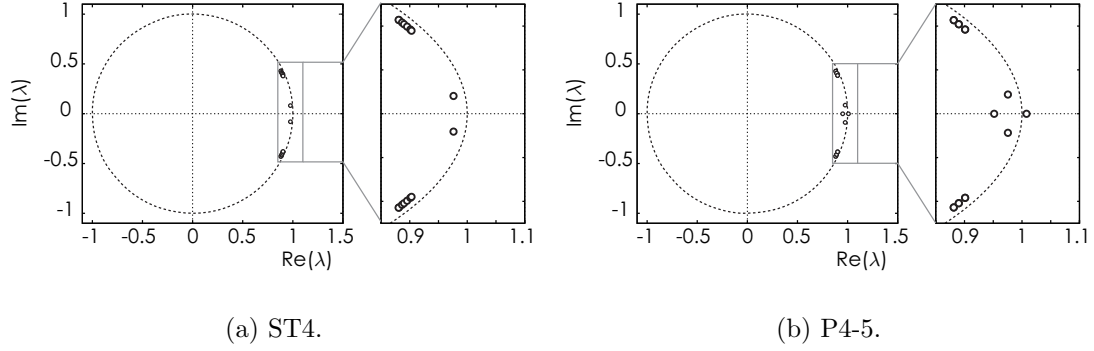
(a) ST4. (b) P4-5.

Figure 6.12: Floquet multipliers of (a) odd symmetric mode and (b) even symmetric mode. The left panel of each case shows an enlarged figure around $+1$ on unit circle. Parameters are set to $\omega = 2\pi \times 36.1$ rad/s , $A = 3$ m/s^2, and $I_{\mathrm{EM}} = 24$ mA.

vative system are ILMs. Consequently, the observed oscillations can be distinguish as ILM.

6.3.4 Stability Analysis

Even symmetric localized oscillations could not be excited experimentally. It implies that the even symmetric oscillations are unstable. In this section, the stability of ST- and P-modes are discussed. Floquet multipliers are obtained numerically for both ST4 and P4-5. Figs. 6.12(a) and (b) show the Floquet multipliers. All multipliers of ST4 are located inside unit circle. Even if a small fluctuation around the ST4 is caused by a disturbance, the fluctuation is exponentially decreased in time. Then, the ST4 is stable. On the other hand, the P4-5 has two Floquet multipliers on the real axis. The right panel in Fig. 6.12(b) shows that one of the multipliers are outside unit circle. Thus, the P4-5 is unstable for the parameters in Table. 6.2.

However, the absolute value of the Floquet multiplier which is outside unit circle is very close to $+1$. Thus, the multiplier will enter unit circle if the damping coefficient is slightly larger. It implies that there is possibility to excite P-modes experimentally.

6.4 Manipulations of ILM

6.4.1 Excitation of ILM

Excitation of ILM is usually realized by the modulational instability [21, 29]. However, the position and the number of ILM cannot be controlled because the modulational instability causes a random behavior of traveling ILMs [61]. On the other hand, an ILM can be excited at any site by adding an impurity [35]. Here we consider the excitation of ILM using an impurity in the macro-cantilever array. It is first assumed that the frequency of external exciter is sufficiently lower than the linear resonant frequency of each cantilever. If the resonant frequency of a cantilever is exclusively decreased by adding an impurity, the corresponding cantilever will resonate. As a result, a localized oscillation appears at which an impurity is added to change the resonant frequency of the cantilever. The impurity should be removed with keeping the localized oscillation. If the localized oscillation is still remained after the removing process, it becomes an ILM.

The experimental result of the excitation is shown in Fig. 6.13. The current flowing in EM at $n = 4$ was decreased from 24.0 mA to 11.5 mA. Then the amplitude of 4th cantilever began to increase. The current was increased to the original value when the amplitude became a large value. As a result, an ILM at $n = 4$ was excited. The excitation is called "seeding" [33].

6.4.2 Attractive Manipulation of ILM

The impurity which can excite an ILM also attracts an ILM excited beside the impurity. Fig. 6.14 shows an attractive manipulation by the impurity. In the manipulation, ST5 is initially excited. After the impurity is added, the amplitude of 4th cantilever begins to increase. On the other hand, the amplitude of 5th cantilever is decreased. The impurity is removed when the amplitudes of 4th and 5th cantilever are almost same. The oscillation of 5th cantilever becomes smaller with spreading small traveling waves. However, the amplitude of 4th cantilever grows in large. As a result, the locus of ILM shifts from $n = 5$ to $n = 4$.

The attractive manipulation is also shown numerically. In Fig. 6.15, the current flowing in EM at $n = 4$ is reduced from 24 mA to 4 mA at $t = 1$ s. Then the amplitude of 4th cantilever begins to increase. The impurity caused by the reduced current is removed at $t = 4.5$ s. The amplitude of 4th cantilever becomes almost same as the 5th cantilever. Then the oscillation of 4th cantilever glows in large and the oscillation of 5th cantilever becomes smaller. Consequently, ST5 is attracted by the impurity as well as the experimental result.
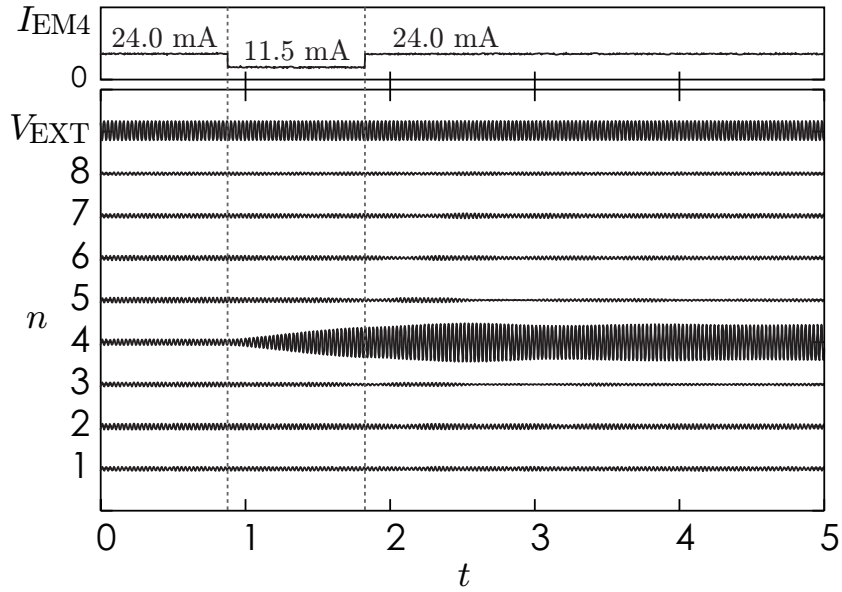
83

Figure 6.13: Generation of an ILM by adding an impurity. The impurity was added at $n = 4$ by varying the current I_{EM4} from 24.0 mA to 11.5 mA.
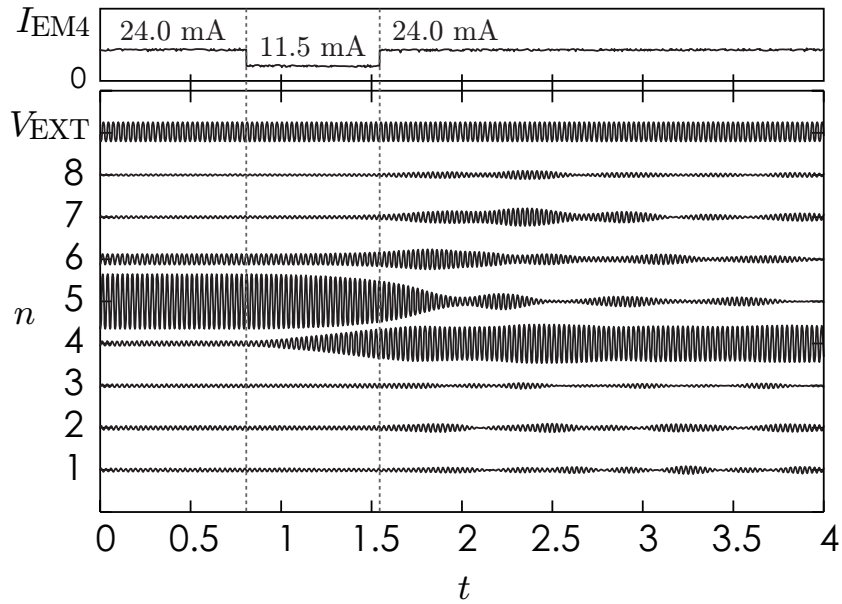

Figure 6.14: Manipulation of an ILM by adding the same impurity as Fig. 6.13. The impurity is added at $t = 0.81$ s and removed at $t = 1.55$ s.
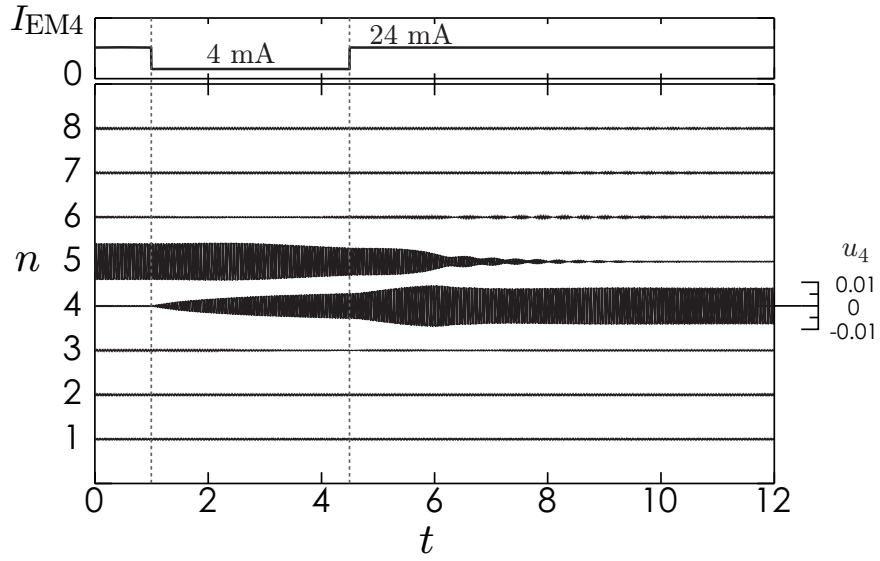
Figure 6.15: Numerical simulation of the attractive manipulation shown in Fig. 6.14. The current flowing in EM at $n = 4$ is decreased to 4 mA when the impurity is added. The impurity is added at $t = 1$ s and removed at $t = 4.5$ s. The amplitude and the frequency of external excitor are set at $A = 3$ m/s^2 and $\omega = 2\pi \times 35.7$ rad/s.
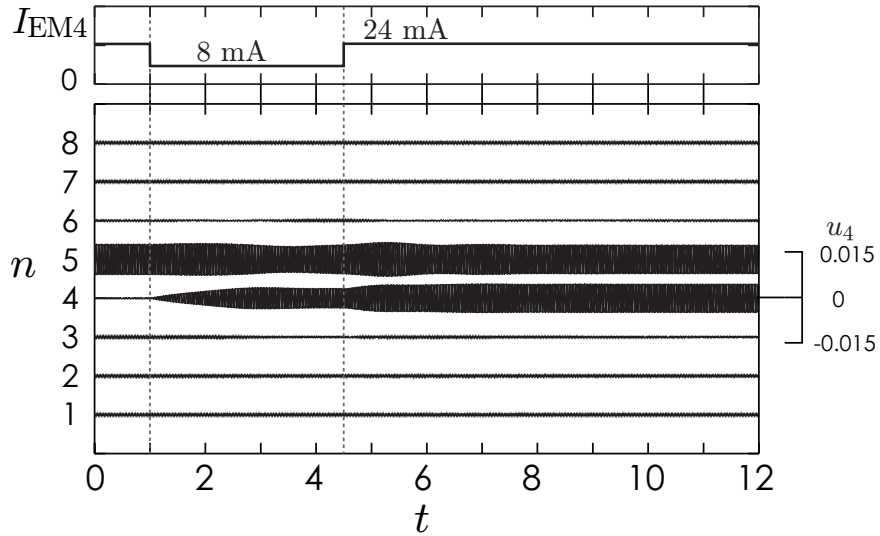

Figure 6.16: Failure of attractive manipulation. The frequency of external excitor is set at $\omega = 2\pi \times 36.2$ rad/s. The current flowing in EM at $n = 4$ is decreased to 8 mA from 24 mA when the impurity is added in this case. The impurity is added at $t = 1$ s and removed at $t = 4.5$ s. The other parameters are same as in Table 6.2.

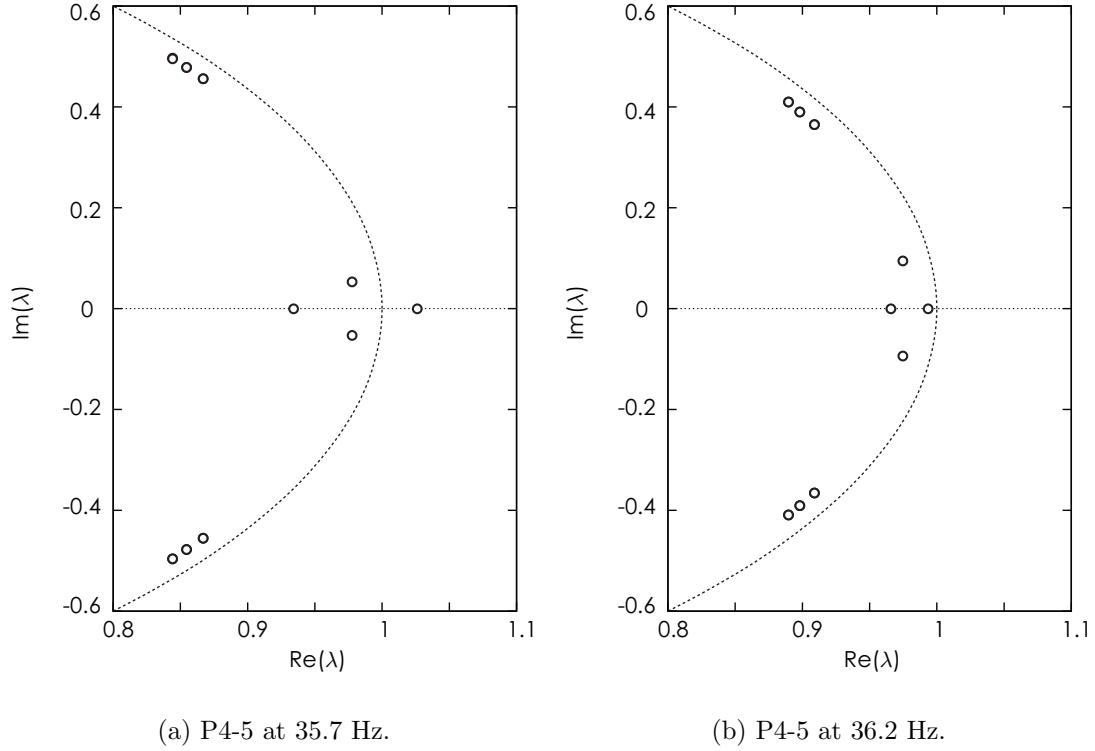(a) P4-5 at 35.7 Hz.   (b) P4-5 at 36.2 Hz.

Figure 6.17: Floquet multipliers of P4-5 at (a) 35.7 Hz and (b) 36.2 Hz.

However, the attractive manipulation is not always possible. An example of failure to manipulate is shown in Fig. 6.16. The frequency of external exciter and the lower value of the current are set at $\omega = 2\pi \times 36.2$ rad/s and 8 mA, respectively. The other parameters are same as Fig. 6.15. Until the impurity is removed, the behaviors of each cantilever are similar to Fig. 6.15. However, the amplitude of 5th cantilever does not decay after removing the impurity. Finally, P4-5 remains. That is, ST5 becomes P4-5 instead of ST4. It implies that P4-5 becomes stable at $\omega = 2\pi \times 36.2$ rad/s.

In the attractive manipulation, the stability of P-modes seems to affect the result of manipulation. Floquet multipliers of P4-5 are shown in Figs. 6.17(a), (b). Although P4-5 is unstable at 35.7 Hz, it becomes stable at 36.2 Hz. One of Floquet multipliers of unstable P4-5 is outside unit circle as shown in Fig. 6.17(a). Thus, the unstable P4-5 has one dimensional unstable manifold. Therefore, it is conjectured that the structure of the unstable manifold in phase space determines the behavior of manipulated ILM.

6.5   Remarks

In this chapter, the macro-mechanical cantilever array was proposed and modeled. The array consists of cantilevers, a coupling rod, an external excitor, and electro magnets. The electro magnets placed beneath cantilevers cause a soft-spring non-linearity. It was experimentally confirmed that the nonlinearity was adjustable by current flowing EMs. In addition, several ILMs were observed experimentally and numerically. It suggests the validity of the model describing the oscillation of individual cantilever. Therefore, the proposed cantilever array seems suitable for the study of ILM by comparison between the numerical and the experimental results.

The excitation and the attractive manipulation were demonstrated experimentally. For the manipulations, an impurity was induced by reducing the current flowing in EM. The impurity locally changed the resonant frequency of cantilevers. Then the amplitude of cantilever increased while the impurity was added. If the amplitude becomes sufficiently large, a ST-mode remains after the impurity is removed. On the other hand, the attractive manipulation was realized by the impurity. In experiments, a ST-mode became another ST-mode. That is, the locus of the ILM is attracted by the impurity. The attractive manipulation was confirmed by numerical simulations. However, a numerical simulation showed that a stable P-mode appeared after the impurity was removed. According to the stability analysis, it is suggested that the attractive manipulation of ST-mode, discussed in the previous chapter, is realized when the P-modes are unstable. Thus, it is conjectured that the structure of unstable manifold of unstable P-modes determines the behavior of manipulated ILM.

As mentioned above, the macro-mechanical cantilever array allows us the experimental investigation of manipulations for ILM. Several facts discussed in conservative systems are also observed in the experimental system. However, the array includes a damping caused by the air resistance and an external excitor. The damping and the external excitation obviously affect the global phase structure. Thus, more investigations are necessary to clarify the dynamics of ILM in the experimental system. In particular, the global phase structure at the low damping regime will be an important role for applications using ILM.

Chapter 7

Conclusion and Future Prospects

In this study, intrinsic localized modes in coupled cantilever arrays were investigated to clarify the mechanism of traveling ILMs and to propose new concepts for manipulation of ILMs. The conclusions obtained in this study and some suggestions for the future works are summarized below.

7.1 Conclusions

In coupled cantilever arrays modeled as nonlinear coupled ordinary differential equations, many ILMs coexist. They were classified into ST-mode, P-mode, and asymmetric mode. ST and P-modes are alternately located in the coupled cantilever array, and the asymmetric modes stand between them. The stability of the coexisting ILMs was investigated by Floquet analysis with respect to the nonlinear inter-site coefficient β_2. The resulting bifurcation diagram showed how the coexisting ILMs exchange their stability. In addition, it was also shown that there is the parameter region in which all coexisting ST- and P-modes are unstable. The asymmetric ILMs coexist as stable solutions in the region with unstable ST- and P-modes. The region is very sensitive against impurities in the array. In other words, the influence of disorder in the array is enhanced around the region where the stability change occurs.

The stability change of ILM was also confirmed at high energy limit. The highest order terms only remain in the equation of motion. The stability change was observed by varying the ratio between nonlinear on-site and inter-site coefficients. This implies that the stability of ILM is dominated by contribution of nonlinearities. Odd symmetric modes tend to be stable when on-site nonlinearity is stronger than inter-site nonlinearity. On the other hand, even symmetric modes tend to be stable

in the regime where inter-site nonlinearity is dominant. This qualitative result seems to be applicable to other systems.

By calculating invariant manifolds of coexisting unstable ILMs, the global phase structure was discussed. As results, cyclic structures surrounding stable ILMs and connections between vicinities of unstable ILMs were observed. In particular, the connections only appear when the stability change occurs. It was also shown that the global phase structure is drastically changed by varying the nonlinear inter-site coefficient. The drastic change occurs almost simultaneously with the stability change. In addition, the process of the drastic change was investigated. As a result, it was suggested that global bifurcations occur. The global bifurcations in high-dimensional phase space are difficult to confirm by numerical simulations. Hence, theoretical approach will be necessary to clarify the problems of how the global phase structure changes.

In Chapter 4, the behavior of traveling ILMs was also discussed. Unstable manifolds of unstable coexisting ILMs strongly affect the behavior of traveling ILM. Even though the initial conditions are very close to each other, the traveling ILMs show completely different trajectories. This result suggests that the global structure of invariant manifolds of unstable ILMs governs the dynamics of traveling ILMs.

In Chapter 5, manipulations of ILM were proposed based on the global phase structure. Capture and release manipulation was first shown by numerical simulations. The drastic change of the global phase structure was caused to capture and to release traveling ILMs. Through the manipulation, in principle, ILM can be shifted to any site. On the other hand, a traveling ILM wandering the whole of the array can also be generated. The nonlinear inter-site coefficient was varied for the manipulation. The nondimensionalization showed that the coefficient means the ratio between the on-site and the inter-site nonlinearities. Then, the nonlinear on-site coefficient can also be used as a control parameter in the capture and release manipulation.

Another manipulation was numerically achieved by adding an impurity into the array. This is known as attractive/repulsive manipulation. The manipulation is based on the fact that the global phase structure is locally changed by the added impurity. Therefore, investigations of the changed global phase structure allow us to predict whether an ILM is attracted or repulsed.

Finally, the attractive manipulation was experimentally realized in the macro-mechanical cantilever array. In the beginning of Chapter 6, the cantilever array having tunable on-site potentials was proposed and modeled. The tunable on-site potentials were realized by using electromagnets. The magnetic interaction causes a soft sprint characteristic into the restoring force of cantilever. Therefore, acoustic ILMs were observed. The observed ILMs have odd-symmetric amplitude distribu-

tion. That is, ST-modes are stable in the cantilever array.

The attractive manipulation was shown by adjusting a current flowing in an electromagnet. As a result, an ILM was attracted to the site where the impurity was added. After the impurity was removed, the ILM survived. This manipulation was also discussed by numerical simulations. As results, it was suggested that unstable even-modes are the key to the manipulation.

The manipulations discussed in this study are possibly applied to other systems in which intrinsic localized modes coexist. Because it was suggested that the nonlinearity ratio in on-site and inter-site potentials determines the stability of coexisting ILMs and changes the global phase structure. That is, the capture and release and the attractive/repulsive manipulations will be realized in a realistic system which has nonlinearities in both on-site and inter-site potentials. The experimental results in the macro-mechanical cantilever array seem to provide an evidence of this generality.

7.2   Future Prospects

The global phase structure regarding traveling ILMs is similar to a pendulum system when the nonlinear inter-site coefficient is close to the critical value causing the stability change. It implies that there is a dynamical analogy between the trajectories of traveling ILM and of the pendulum. It seems to be worthwhile to investigate the analogy. Tremendous knowledge gained on pendulum system can also apply to the dynamics of traveling ILM.

The possibility of control of ILM has been shown experimentally in electronic circuit ladders [33]. The ladders were designed to have both ILMs and soliton-like waves. The soliton-like waves excited at the both ends of ladder and propagated into the ladder. An ILM was excited at which two soliton-like waves collided. The mechanism of the excitation is the same as the seeding by using impurity. The ladder has varactor diodes exhibiting capacitance variations as a function of applied voltage. Thus, a soliton-like wave plays a role as a localized impurity. When the soliton-like waves collide, the amplitude becomes twice as large. Then, a strong impurity appears. Therefore, an ILM is excited. Other manipulations such as attraction were also realized in the ladders. This suggests that ILM can be controlled by indirectly added impurities. Since the individual adjustment of on-site potentials is hopeless in atomic scale system, the manipulations using soliton-like waves become significant.

Intrinsic localized mode is not a rare phenomenon in the nature. As mentioned in Chapter 1, ILM has been identified in various physical systems. Recently, it has been suggested that ILM exists in nanometer scale system such as DNA [62, 63], Si

crystal [64], graphene sheet [65], and carbon nano-tubes [66]. It implies that ILM plays an important role in nanoscience. In addition, it allows us to expect that ILM can be utilized in nanoelectromechanical system (NEMS).

Bibliography

[1] A. J. Sievers, S. Takeno, Intrinsic localized modes in anharmonic crystals, Phys. Rev. Lett. 61 (1988) 970.

[2] S. Takeno, A. J. Sievers, Anharmonic resonant modes in perfect crystals, Solid State Commun. 67 (1988) 1023.

[3] E. Fermi, J. Pasta, S. Ulam, Studies of non linear problems, in: The collected papers of Enrico Fermi, Vol. 2, University of Chicago Press, Chicago, 1955, pp. 978–988.

[4] J. B. Page, Asymptotic solutions for localized vibrational modes in strongly anharmonic periodic systems, Phys. Rev. B 41 (1990) 7835.

[5] S. Flach, Conditions on the existence of localized excitations in nonlinear discrete systems, Phys. Rev. E 50 (1994) 3134.

[6] R. S. MacKay, S. Aubry, Proof of existence of breathers for time-reversible or Hamiltonian networks of weakly coupled oscillators, Nonlinearity 7 (1994) 1623.

[7] K. W. Sandusky, J. B. Page, Interrelation between the stability of extended normal modes and the existence of intrinsic localized modes in nonlinear lattices with realistic potentials, Phys. Rev. B 50 (1994) 866.

[8] S. Flach, Existence of localized excitations in nonlinear Hamiltonian lattices, Phys. Rev. E 51 (1995) 1503.

[9] R. S. MacKay, J. A. Sepulchre, Multistability in networks of weakly coupled bistable units, Physica D 82 (1995) 243.

[10] R. Livi, M. Spicci, R. S. MacKay, Breathers on a diatiomic FPU chain, Nonlinearity 10 (1997) 1421.

[11] J. A. Sepulchre, R. S. MacKay, Localized oscillations in conservative or dissipative networks of weakly coupled autonomous oscillators, Nonlinearity 10 (1997) 679.

[12] K. W. Sandusky, J. B. Page, K. E. Schmidt, Stability and motion of intrinsic localized modes in nonlinear periodic lattices, Phys. Rev. B 46 (10) (1992) 6161.

[13] S. R. Bickham, S. A. Kiselev, A. J. Sievers, Stationary and moving intrinsic localized modes in one-dimensional monatomic lattices with cubic and quartic anharmonicity, Phys. Rev. B 47 (1993) 14206.

[14] O. A. Chubykalo, A. S. Kovalev, O. V. Usatenko, Stability of intrinsic localized modes in anharmonic 1-D lattices, Phys. Lett. A 178 (1993) 129.

[15] S. Aubry, Breathers in nonlinear lattices: Existence, linear stability and quantization, Physica D 103 (1997) 201.

[16] S. R. Bickham, A. J. Sievers, S. Takeno, Numerical measurements of the shape and dispersion relation for moving one-dimensional anharmonic localized modes, Phys. Rev. B 45 (1992) 10344.

[17] S. Flach, C. R. Willis, Movability of localized excitations in nonlinear discrete systems: A separatrix problem, Phys. Rev. Lett. 72 (1994) 1777.

[18] D. Chen, S. Aubry, G. P. Tsironis, Breather mobility in discrete ϕ^4 nonlinear lattices, Phys. Rev. Lett. 77 (1996) 4776.

[19] P. A. Houle, Phase plane of moving discrete breathers, Phys. Rev. E 56 (1997) 56.

[20] S. Aubry, T. Cretegny, Mobility and reactivity of discrete bteathers, Physica D 119 (1998) 34.

[21] S. Flach, C. R. Willis, Discrete breathers, Phys. Rep. 295 (1998) 181.

[22] D. K. Campbell, S. Flach, Y. S. Kivshar, Localizing energy through nonlinearity and discreteness, Phys. Today 57 (2004) 43.

[23] E. Trías, J. J. Mazo, T. P. Orlando, Discrete breathers in nonlinear lattices: Experimental detection in a Josephson array, Phys. Rev. Lett. 84 (2000) 741.

[24] P. Binder, D. Abraimov, A. V. Ustinov, S. Flach, Y. Zolotaryuk, Observation of breathers in Josephson ladders, Phys. Rev. Lett. 84 (2000) 745.

[25] A. V. Ustinov, Imaging of discrete breathers, Chaos 13 (2003) 716.

[26] H. S. Eisenberg, Y. Silberberg, R. Morandotti, A. R. Boyd, J. S. Aitchison, Discrete spatial optical solitons in waveguide arrays, Phys. Rev. Lett. 81 (1998) 3383.

[27] R. Morandotti, U. Peschel, J. S. Aitchison, H. S. Eisenberg, Y. Silberberg, Dynamics of discrete solitons in optical waveguide arrays, Phys. Rev. Lett. 83 (1999) 2726.

[28] J. W. Fleischer, M. Segev, N. K. Efremidis, D. N. Christodoulides, Observation of two-dimensional discrete solitons in optically induced nonlinear photonic lattices, Nature 422 (2003) 147.

[29] M. Sato, B. E. Hubbard, A. J. Sievers, B. Ilic, D. A. Czaplewski, H. G. Craighead, Observation of locked intrinsic localized vibrational modes in a micromechanical oscillator array, Phys. Rev. Lett. 90 (2003) 044102.

[30] B. I. Swanson, J. A. Brozik, S. P. Love, G. F. Strouse, A. P. Shreve, A. R. Bishop, W.-Z. Wang, M. I. Salkola, Observation of intrinsically localized modes in a discrete low-dimensional material, Phys. Rev. Lett. 82 (1999) 3288.

[31] K. Kisoda, N. Kimura, H. Harima, K. Takenouchi, M. Nakajima, Intrinsic localized vibrational modes in a highly nonlinear halogen-bridged metal, J. Lumin. 94 (2001) 743.

[32] M. Sato, A. J. Sievers, Direct observation of the discrete character of intrinsic localized modes in an antiferromagnet, Nature 432 (2004) 486.

[33] M. Sato, S. Yasui, M. Kimura, T. Hikihara, A. J. Sievers, Management of localized energy in discrete nonlinear transmission lines, Europhys. Lett. 80 (2007) 30002.

[34] M. Sato, B. E. Hubbard, L. Q. English, A.J.Sievers, B. Ilic, D. A. Czaplewski, H. G. Craighead, Study of intrinsic localized vibrational modes in micromechanical oscillator arrays, Chaos 13 (2003) 702.

[35] M. Sato, B. E. Hubbard, A. J. Sievers, B. Ilic, H. G. Craighead, Optical manipulation of intrinsic localized vibrational energy in cantilever arrays, Europhys. Lett. 66 (3) (2004) 318.

[36] M. Sato, B. E. Hubbard, A. J. Sievers, *Colloquium*: Nonlinear energy localization and its manipulation in micromechanical oscillator arrays, Rev. Mod. Phys. 78 (2006) 137.

[37] P. S. Waggoner, H. G. Craighead, Micro- and nanomechanical sensors for environmental, chemical, and biological detection, Lab Chip 7 (2007) 1238.

[38] T. Ono, X. Li, H. Miyashita, M. Esashi, Mass sensing of adsorbed molecules in sub-picogram sample with ultrathin silicon resonator, Rev. Sci. Instrum. 74 (2003) 1240.

[39] M. Spletzer, A. Raman, A. Q. Wu, X. Xu, R. Reifenberger, Ultrasensitive mass sensing using mode localization in coupled microcantilevers, Appl. Phys. Lett. 88 (2006) 254102.

[40] T. Hikihara, Y. Okamoto, Y. Ueda, An experimental spatio-temporal state transition of coupled magneto-elastic system, Chaos 7 (1997) 810.

[41] T. Hikihara, K. Torii, Y. Ueda, Wave and basin structure in spatially coupled magneto-elastic beam system – transitions between coexisting wave solutions, Int. J. Bifurcat. and Chaos 11 (2001) 999.

[42] T. Hikihara, K. Torii, Y. Ueda, Quasi-periodic wave and its bifurcation in coupled magneto-elastic beam system, Phys. Lett. A 281 (2001) 155.

[43] K. Yamasue, Studies on time-delayed feedback control of chaos and its application to dynamic force microscopy, Ph.D. thesis, Kyoto University (November 2006).

[44] S. Flach, A. V. Gorbach, Discrete breathers – advances in theory and applications, Phys. Rep. 467 (2008) 1–116.

[45] M. R. M. Crespo da Silva, C. C. Glynn, Nonlinear flexural-flexural-torsional dynamics of inextensional beams. I. Equations of motion, J. Struct. Mech. 6 (1978) 437.

[46] M. R. M. Crespo da Silva, Non-linear flexural-flexural-torsional-extensional dynamics of beams – I. Formulation, Int. J. Solids Structures 24 (1988) 1225.

[47] P. Malatkar, A. H. Nayfeh, On the transfer of energy between widely spaced modes in structures, Nonlinear Dyn. 31 (2003) 225.

[48] M. Sato, private communication (2008).

[49] M. Toda, Nonlinear Waves and Solitons, Nippon-Hyoron-sha, 1983, in Japanese.

[50] M. Toda, Oscillations, BAIFUKAN, 1968, in Japanese.

[51] S. Flach, A. Gorbach, Discrete breathers in Fermi-Pasta-Ulam lattices, Chaos 15 (2005) 15112.

[52] L. M. Marín, S. Aubry, Breathers in nonlinear lattices: numerical calculation from the anticontinuous limit, Nonlinearity 9 (1996) 1501.

[53] S. Flach, Energy Localisation and Transfer, World Scientific, 2004, Ch. 1, pp. 1–71.

[54] W. H. Press, S. A. Teukolsky, W. T. Vetterling, B. P. Flannery, Numerical Recipes in C, Second Edition, Cambridge University Press, New York, 1992.

[55] J. Guckenheimer, P. Holmes, Nonlinear Oscillations, Dynamical Systems, and Bifurcations of Vector Fields, Springer-Verlag, 1983, Ch. 1, pp. 22–32.

[56] P. Bergé, Y. Pomeau, C. Vidal, Order within Chaos, Wiley, New York, 1984.

[57] J. Guckenheimer, P. Holmes, Nonlinear Oscillations, Dynamical Systems, and Bifurcations of Vector Fields, Springer-Verlag, 1983, Ch. 1, pp. 1–22.

[58] S. Wiggins, Introduction to Applied Nonlinear Dynamical Systems and Chaos, 2nd Edition, Springer-Verlag, 2003.

[59] M. I. Younis, A. H. Nayfeh, A study of the nonlinear response of a resonant microbeam to an electric actuation, Nonlinear Dyn. 31 (2003) 91.

[60] F. C. Moon, P. J. Holmes, A magnetoelastic strange attractor, J. Sound Vibrat. 65 (2) (1979) 275.

[61] T. Cretegny, T. Dauxois, S. Ruffo, A. Torcini, Localization and equipartition of energy in the β-FPU chain: Chaotic brethers, Physica D 121 (1998) 109.

[62] T. Dauxois, M. Peyrard, C. R. Willis, Localized breather-like solution in a discrete Klein-Gordon model and application to DNA, Physica D 57 (1992) 267.

[63] M. Peyrard, Y. Sire, Energy Localisation and Transfer, World Scientific, 2004, Ch. 8, pp. 325–340.

[64] N. K. Voulgarakis, G. Hadjisavvas, P. C. Kelires, G. P. Tsironis, Computational investigation of intrinsic localization in crystalline Si, Phys. Rev. B 69 (2004) 113201.

[65] Y. Yamayose, Y. Kinoshita, Y. Doi, A. Nakatani, T. Kitamura, Excitation of intrinsic localized modes in a graphene sheet, Europhys. Lett. 80 (2007) 40008.

[66] Y. Kinoshita, Y. Yamayose, Y. Doi, A. Nakatani, T. Kitamura, Selective excitations of intrinsic localized modes of atomic scales in carbon nanotubes, Phys. Rev. B 77 (2008) 024307.

Acknowledgements

Finally, the author would like to thank my parents, Shinichi and Chiyo Kimura, for their continual supports and encouragement.

List of acronyms and symbols

Acronyms

A/D   Analog-to-Digital
DB   Discrete Breather
D/A   Digital-to-Analog
EM   Electro Magnet
FPU   Fermi-Pasta-Ulam
IEICE   the Institute of Electronics, Information and Communication Engineers
ILM   Intrinsic Localized Mode
IP   Initial Point
KG   Klein-Gordon
P   Page
PM   Permanent Magnet
ST   Sievers-Takeno
VCM   Voice Coil Motor

Symbols

ℓ Length of cantilever
w Width of cantilever
h Thickness of cantilever
ω_0 Resonant frequency of the first mode of cantilever
α_1 Nondimensional coefficient of linear on-site term
α_2 Nondimensional coefficient of linear coupling term
β_1 Nondimensional coefficient of nonlinear on-site term
β_2 Nondimensional coefficient of nonlinear coupling term
u_n Displacement of nth cantilever

List of Publications

Journal articles

- M. Kimura and T. Hikihara, "Stability Change of Intrinsic Localized Mode in Finite Nonlinear Coupled Oscillators," Phys. Lett. A 372, 4592, (2008).

- M. Kimura and T. Hikihara, "Capture and Release of Traveling Intrinsic Localized Mode in Coupled Cantilever Array," Chaos, (accepted).

- M. Kimura and T. Hikihara, "Coupled Cantilever Array having Tunable On-site Potential and Observation of Localized Oscillation," Phys. Lett. A, (accepted).

International conference proceedings

- M. Kimura and T. Hikihara, "A Numerical Study on Invariant Manifold Related to Transition of Intrinsic Localized Mode in Coupled Cantilever Array," 2007 International Symposium on Nonlinear Theory and its Applications, Vancouver, Canada, September 16-19 (2007).

Domestic conference proceedings and technical reports

- M. Kimura and T. Hikihara, "A Numerical Study on Bifurcations of Intrinsic Localized Modes in Coupled Cantilever Arrays without Dissipations," 2005 Kansai-section Joint Convention of Institutes of Electrical Engineering, G2-17, Kyoto University Katsura-Campus, Kyoto, Japan, November 12-13 (2005).

- M. Kimura and T. Hikihara, "Global Phase Structure of Coupled Cantilever Array and Transition of Intrinsic Localized Mode," Research Institute for Mathematical Sciences (RIMS) Workshop "Mathematical Aspects of Complex Fluids and Their Applications", RIMS, Kyoto, Japan, November 16-18 (2005). RIMS Kokyuroku No.1472, pp.193-202 (2006)(in JAPANESE).

- M. Kimura and T. Hikihara, "Coexistence and Transition of Intrinsic Localized Mode in Coupled Cantilever Arrays," Technical Committee on Nonlinear Problems (NLP), Technical report NLP2005-90, pp.27-32, College of Engineering, Ibaraki University, Ibaraki, Japan, December 16 (2005).

- M. Kimura and T. Hikihara, "A Numerical Study on Transition of Unstable Intrinsic Localized Mode in Coupled Cantilever Arrays with Fixed Boundary Condition," Technical Committee on Nonlinear Problems (NLP), Technical report NLP2006-8, pp.37-42, Faculty of Engineering, Kumamoto University, Kumamoto, Japan, May 11 (2006).

- M. Kimura and T. Hikihara, "A Study of Transition and Invariant Manifold of Unstable Intrinsic Localized Mode in Coupled Cantilever Arrays with Fixed Boundary Condition," Technical Committee on Nonlinear Problems (NLP), Technical report NLP2006-31, pp.53-58, Graduate School of Natural Science and Technology, Kanazawa University, Kanazawa, Japan, July 3 (2006).

- M. Kimura and T. Hikihara, "A Numerical Study on Traveling Intrinsic Localized Mode in Coupled Cantilever Array with an Impurity," 2008 IEICE General Conference, A2-2-26, Kitakyushu Science and Research Park, Kitakyusyu, Japan, March 18-21 (2008).

- M. Kimura and T. Hikihara, "Observation of Intrinsic Localized Modes in Coupled Cantilever Array with Electromagnets," 2008 Kansai-section Joint Convention of Institutes of Electrical Engineering, G1-18, Kyoto Institute of Technology, Kyoto, Japan, November 8-9 (2008).

- M. Kimura and T. Hikihara, "Manipulation of Intrinsic Localized Mode based on Invariant Manifold Structure," Technical Committee on Nonlinear Problems (NLP), Technical report NLP2008-72, pp.11-16, Ishikawa Prefectural Bunkyo Hall, Kanazawa, Japan, December 9-10 (2008).